



Intermediate Band Properties of Femtosecond-Laser Hyperdoped Silicon

Citation

Sher, Meng-Ju. 2013. Intermediate Band Properties of Femtosecond-Laser Hyperdoped Silicon. Doctoral dissertation, Harvard University.

Permanent link

<http://nrs.harvard.edu/urn-3:HUL.InstRepos:11095958>

Terms of Use

This article was downloaded from Harvard University's DASH repository, and is made available under the terms and conditions applicable to Other Posted Material, as set forth at <http://nrs.harvard.edu/urn-3:HUL.InstRepos:dash.current.terms-of-use#LAA>

Share Your Story

The Harvard community has made this article openly available.
Please share how this access benefits you. [Submit a story](#).

[Accessibility](#)

Intermediate Band Properties of Femtosecond-Laser Hyperdoped Silicon

A thesis presented

by

Meng-Ju Sher

to

The Department of Physics

in partial fulfillment of the requirements

for the degree of

Doctor of Philosophy

in the subject of

Physics

Harvard University

Cambridge, Massachusetts

May 2013

©2013 - Meng-Ju Sher

All rights reserved.

Thesis advisor

Eric Mazur

Author

Meng-Ju Sher

Intermediate Band Properties of Femtosecond-Laser Hyperdoped Silicon

Abstract

This thesis explores using femtosecond-laser pulses to hyperdope silicon with chalcogen dopants at concentrations above the maximum equilibrium solubility. Hyperdoped silicon is promising for improving efficiencies of solar cells: the material exhibits broad-band light absorption to wavelengths deep below the corresponding bandgap energy of silicon. The high concentration of dopants forms an intermediate band (IB), instead of discrete energy levels, and the IB enables sub-bandgap light absorption. This thesis is divided into two primary studies: the dopant incorporation and the IB properties.

First, we study dopant incorporation with a gas-phase dopant precursor (SF_6) using secondary ion mass spectrometry. By varying the pressure of SF_6 , we find that the surface adsorbed molecules are the dominant source of the dopant. Furthermore, we show the hyperdoped layer is single crystalline. The results demonstrate that the dopant incorporation depth, concentration, and crystallinity are controlled respectively by the number of laser pulses, pressure of the dopant precursor, and laser fluence.

Second, we study the IB properties of hyperdoped silicon using optical and electronic measurements. We use Fourier transform infrared spectroscopy to study light

absorption. The absorption extends to wavelengths as far as $6\ \mu\text{m}$ before thermal annealing and we find the upper bound of the IB location at $0.2\ \text{eV}$ below the conduction band edge. For electronic measurements, we anneal the samples to form a diode between the hyperdoped layer and the substrate, allowing us to probe the IB using temperature-dependent electronic transport measurements. The measurement data indicate that these samples form a localized IB at concentrations below the insulator-to-metal transition. Using a two-band model, we obtain the location of the localized IB at $>0.07\ \text{eV}$ below the conduction band edge.

After femtosecond-laser hyperdoping, annealing is necessary to reduce the laser-induced defects; however annealing decreases the sub-bandgap absorption. As we are interested in the IB that contributes to sub-bandgap absorption, we explore methods to reactivate the sub-bandgap absorption. We show that the sub-bandgap absorption is reactivated by annealing at high temperatures between 1350 and $1550\ \text{K}$ followed by fast cooling ($>50\ \text{K/s}$). Our results demonstrate an ability to control sub-bandgap absorption using thermal processing.

Contents

Title Page	i
Abstract	iii
Table of Contents	v
Citations to previously published work	viii
Acknowledgments	ix
Dedication	xi
1 Introduction	1
1.1 Motivation	2
1.2 Hyperdoping	4
1.2.1 Laser melting and doping	5
1.2.2 Hyperdoping with femtosecond lasers	8
1.2.3 Applications to photovoltaics	11
1.3 Surface texturization	13
1.3.1 Pulsed-laser surface texturization	14
1.3.2 Geometric light trapping	16
1.4 Summary	17
1.5 Organization of the dissertation	18
2 Experimental methods and updates	20
2.1 Sample fabrication	20
2.1.1 Ambient pressure	22
2.1.2 Fluence	23
2.1.3 Shots per area: the average number of laser pulses delivered to the sample	24
2.2 Stationary and scanning pulses	26
2.3 Influence of SF ₆ pressure on surface morphology	28
3 The dopant incorporation mechanism	34
3.1 Introduction	35
3.2 Experimental	37

3.3	Results	39
3.4	Discussion	44
3.4.1	Crystalline phase	44
3.4.2	Source of dopant atoms	45
3.4.3	Pulse number dependence and concentration profiles	47
3.5	Conclusion	50
4	Intermediate band conduction in fs-laser hyperdoped silicon	52
4.1	Introduction	53
4.2	Experimental	55
4.3	Results	57
4.4	Discussion	61
4.4.1	Carrier concentration at thermal equilibrium	61
4.4.2	Two-band conduction at high dopant concentration	63
4.4.3	S-hyperdoped silicon	67
4.4.4	Intermediate band below the insulator-to-metal transition	69
4.4.5	Electronic properties decoupled with optical properties	70
4.5	Conclusion	71
5	Mid-infrared absorptance	73
5.1	Introduction	74
5.2	Experimental	76
5.3	Results and discussion	77
5.3.1	Upper bound on dopant energy levels	77
5.3.2	Broad resonance features after annealing	83
5.4	Conclusion	88
6	Reactivation of sub-bandgap absorption	89
6.1	Introduction	90
6.2	Experimental	91
6.3	Results	92
6.4	Discussion	96
6.5	Conclusion	97
7	Summary and future directions	98
7.1	Summaries	98
7.2	Future directions	100
A	The Hall effect	103
A.1	Introduction	103
A.2	Two types of carriers	106

B Spectrophotometer corrections	109
B.1 Corrections to reflection measurements	110
B.1.1 Case I: diffuse reflection	112
B.1.2 Case II: specular reflection	113
B.2 Results	114
B.3 Summary and future work	116
C The photovoltaic potential of fs-laser textured amorphous silicon	118
C.1 Introduction	119
C.2 Experimental	120
C.3 Results	122
C.4 Discussion	126
C.5 Conclusion	129
Bibliography	130

Citations to previously published work

Parts of this dissertation cover research reported in the following articles:

1. M.-J. Sher, Y.-T. Lin, M. T. Winkler, E. Mazur, C. Pruner and A. Asenbaum, “Mid-infrared absorptance of silicon hyperdoped with chalcogen via fs-laser irradiation,” *Journal of Applied Physics*, **113**, 063520, 2013.
2. M.-J. Sher, K. Hammond, L. Christakis, E. Mazur, “The photovoltaic potential of femtosecond-laser textured amorphous silicon,” *SPIE 2013 Photonics West Conference Proceedings*, (San Francisco, CA), 2013,
3. M.-J. Sher, M. T. Winkler, E. Mazur, “Pulsed-laser hyperdoping and surface texturing for photovoltaics,” *MRS Bulletin*, **36**, 439, 2011.
4. B. K. Newman, M.-J. Sher, E. Mazur, T. Buonassisi, “Reactivation of sub-bandgap absorption in hyper-doped silicon,” *Applied Physics Letters*, **98**, 251905, 2011.

Acknowledgments

I want to thank everyone who has helped me along the way. The past six years would have been impossible without the support from a very large group of people including my thesis committee, labmates, collaborators, friends, and family, all to whom I am indebted.

First, I would like to thank my advisor Eric Mazur and the Mazur group. I am grateful for the well-rounded training Eric provides as well as the trust and freedom to pursue our research goals. With the group, we not only have been through many of the hardest practice qualifying exams, but also many exhausting and fun outings, barbecues, and dumpling parties together. Mark Winkler, Paul Peng, and Eric Diebold are great mentors who taught me the required patience and persistence for doing research. Yu-Ting Lin, Ben Franta, Kasey Phillips, Guoliang Deng, Jin Suntivich, and Thierry Sarnet helped out in every aspect and allowed me to focus on a small subset of all the possible combinations of experimental parameters. Chris Evans and I took many M2 buses and discussed numerous research problems together. I am likewise grateful to colleagues and friends: Tina Shih, Sam Chung, Rafa Gattass, Valeria Nuzzo, Jason Dowd, Phil Munoz, Orad Reshef, Sally Kang, Kevin Vora, Michael Moebius, Sarah Griesse-Nascimento, Nabiha Saklayen, Haifei Zhang, and Sebastien Courvoisier. Lastly, the younger group members such as Ken Hammond, Lysander Christakis, and Weilu Shen encouraged me with their enthusiasm and curiosity. The interdisciplinary, supportive, and fun environment the Mazur group provided over the years is truly unique.

I am very fortunate to work with a group of talented collaborators on the black silicon project. I would like to thank the black silicon team both for their intellec-

Acknowledgments

tual support and friendship over the years. Matt Smith supported us with impressive microstructural analysis. Joe Sullivan, Christie Simmons, Jacob Krich, and Elif Ertekin helped tremendously on the band structure and the implied material properties. Bonna Newman contributed many sleepless hours at synchrotron facilities. I would like to thank Niall Mangan, Tobias Schneider, and Sophie Marbach for taking on the task of understanding the ultrafast melting and resolidification dynamics. I am grateful for valuable discussions with Austin Akey, Dan Recht, Jim Carey, and Jeff Warrender. Lastly, I would like to thank all of the faculty involved with this fruitful collaboration: Prof. Tonio Buonassisi, Prof. Silviya Gradecak, Prof. Michael Brenner, Prof. Augustinus Asenbaum, Prof. Michel Meunier, Prof. Cyndy Friend, Prof. Alan Aspuru-Guzik, as well as my committee members Prof. Mike Aziz and Prof. Efthimios Kaxiras.

Lastly, graduate school became a lot more fun with support from friends and family who prevented me from spending too much time in the lab. I owe a special thank you to my big loving family: my parents, brother, grandparents, great aunts, great uncles, aunts, uncles, and cousins. I would like to thank my wonderful roommates Jack and Eddie, friends whom we played weekly volleyball together, as well as teaching staff and students from Physics 15b of Fall 2012 and 15c of Spring 2013; they gave me a wonderful place to be when I was not working on my thesis. Thank you!

Acknowledgements of Financial Support

This thesis is based on work funded by the National Science Foundation under contract CBET-0754227 and DMR-0934480.

To my loving family

Chapter 1

Introduction

We motivate this thesis by describing two ways in which pulsed lasers can be used to increase efficiency in photovoltaic devices. First, pulsed-laser hyperdoping can introduce dopants into a semiconductor at non-equilibrium concentrations, which creates an intermediate band within the bandgap of the material and modifies the absorption coefficient. Second, pulsed-laser irradiation can enhance geometric light trapping by increasing surface roughness. Hyperdoping in silicon enables absorption of photons to wavelengths of at least $2.5 \mu\text{m}$, while texturing enhances the absorptance to near unity at all absorbing wavelengths. This thesis focuses on understating the hyperdoping process and the intermediate band properties, but the femtosecond-laser texturing occurs simultaneously in our fabrication process. This chapter reviews both effects and provides connection to this thesis.

1.1 Motivation

Most approaches to photon management in photovoltaics (PV) focus on increasing the total absorbed irradiance I_{abs} from the incident solar irradiance I_{sun} through some modification of the photovoltaic material. The total absorbed irradiance of a material, obtained from Beer’s law, is:

$$I_{\text{abs}} = \int I_{\text{sun}}(\lambda)[1 - R(\lambda)][1 - \exp[-\alpha(\lambda) d]] d\lambda, \quad (1.1)$$

where R and α are the wavelength-dependent reflectance and absorption coefficients, respectively; d is the path length of a photon through the material; and the integration is over all optical wavelengths λ . Thus, neglecting wavelength conversion approaches, photon management requires manipulating one or more of three material parameters: α , R , or d . Pulsed-laser processing of semiconductors with nanosecond, picosecond, or femtosecond laser pulses, offers two very different approaches to enhance photon absorption: pulsed-laser hyperdoping and surface texturing. For example, the “black silicon” process [1], achieves near-unity, broadband absorption of visible and near infrared light in silicon with femtosecond laser processing. The effects of these techniques on light absorption are summarized in Figure 1.1.

First, pulsed-laser irradiation can be used to introduce non-equilibrium concentrations of dopants into silicon, a process we refer to as hyperdoping. This process changes silicon’s electronic structure and increases the absorption coefficient α [4–7]. Second, pulsed-laser irradiation of a silicon wafer can produce micrometer- or nanometer-scale surface textures that are suitable for geometric light trapping [8–10]. Hyperdoping significantly increases the absorption coefficient through the inclusion of

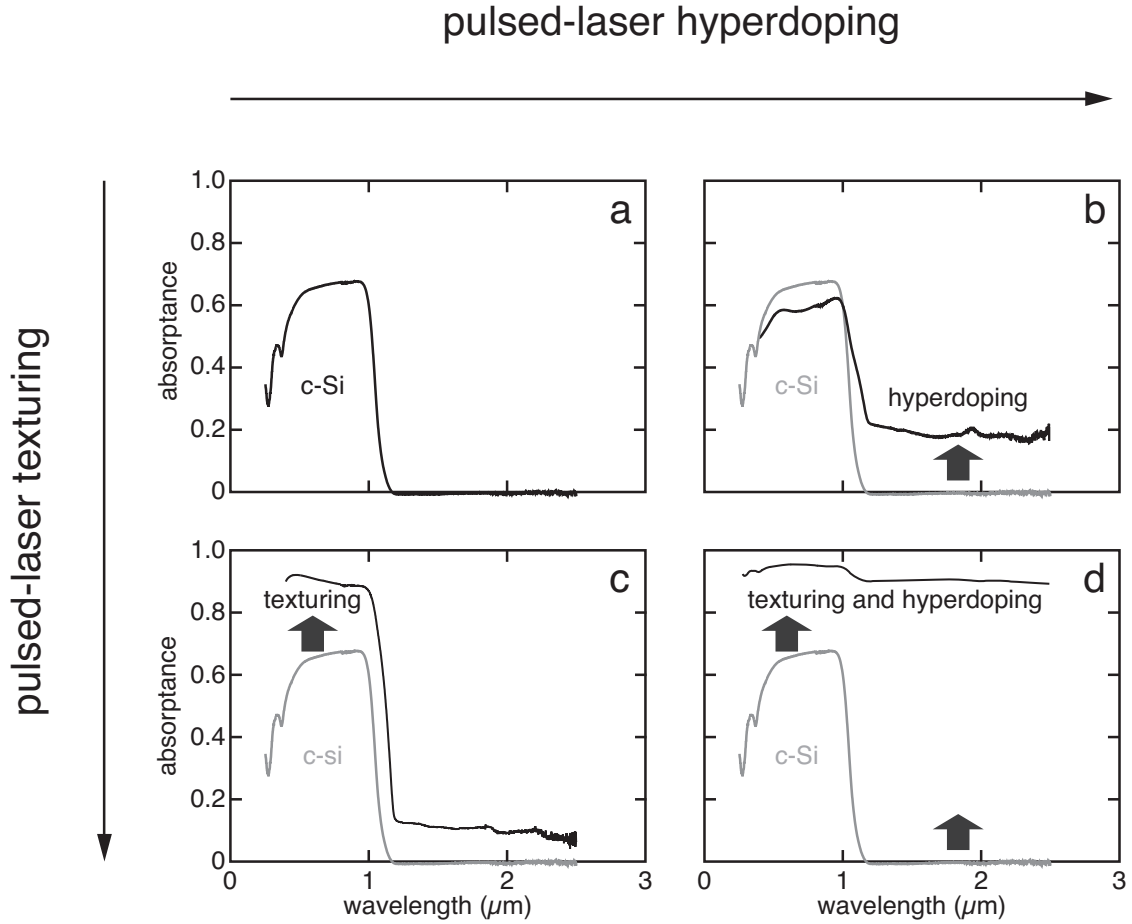


Figure 1.1: Absorption enhancement from pulsed-laser hyperdoping and surface texturing. The absorbance A is obtained from the expression $A = 1 - R - T$, where R and T are reflectance and transmittance, respectively, measured with an integrating sphere to collect both specular and diffuse light. (a) untreated crystalline silicon (c-Si) has zero absorption of light with wavelength longer than $1.1 \mu\text{m}$ due to its energy bandgap. (b) Pulsed-laser hyperdoping with sulfur enables absorption of sub-bandgap light. (c) Pulsed-laser texturing enhances above-bandgap light absorption with geometric light trapping. (d) Broadband near-unity absorption is achieved with both pulsed-laser hyperdoping and surface texturing. Adapted from References [2] and [3].

a high concentration of new electronic states. The process depends on the fast resolidification that follows pulsed-laser melting, which traps dopant atoms at concentrations far above equilibrium solubility limits [11, 12]. Realizing such dopant concentrations with deep-level impurities is a possible route to fabricating an intermediate band photovoltaic cell, a high-efficiency PV concept [13]. Surface texturing, on the other hand, increases the fraction of absorbed photons by increasing d and effectively decreasing $R(\lambda)$ (Equation 1.1). Texturization relies on laser-induced ablation of silicon, which selectively removes material to create light trapping morphologies. These two pulsed-laser approaches to photon management are distinct and can be realized independently, although most research in this field has focused on a combination of these two effects [8, 14–16].

In this chapter, we review pulsed-laser hyperdoping and surface texturing, summarize the current state of the art for both techniques, and discuss outstanding questions and challenges for each application. We first describe the basic physics of laser-induced melting, how it leads to hyperdoping and changes in the absorption coefficient, and ongoing research directions in this field toward realizing efficient photovoltaic devices. Next, we describe laser ablation and how it leads to surface geometries that are advantageous for geometric light trapping. Finally, we outline the connection to and organization of this thesis.

1.2 Hyperdoping

Pulsed lasers have been used in doping processes since the 1960s, including laser-assisted doping [17, 18], gas immersion laser doping [19, 20], pulsed laser mixing [21],

and laser-induced diffusion [22]. Lasers with pulse durations between hundreds of femtoseconds and tens of nanoseconds can achieve dopant concentrations that exceed the solid solubility limit by several orders of magnitude. Although we focus on silicon in this chapter, alternative laser-processes have been explored for other materials, including binary [23] and quaternary [24–26] materials. The hyperdoping process can introduce dopant states that enhance absorption at photon energies above and below the bandgap, making it a potential route to realizing intermediate band photovoltaic devices.

1.2.1 Laser melting and doping

When a laser pulse delivers energy to a solid volume at a rate sufficiently in excess of any cooling processes, such as conduction to the underlying bulk, it can raise the solid’s temperature above the melting point and cause a layer near the surface to melt. Pulsed lasers are well-suited to this application for two reasons. First, for laser pulses that are nanoseconds or shorter in duration, the energy is deposited over a timescale that is comparable to or shorter than that of heat diffusion [27]—thus heat accumulates faster than it can be conducted away to the substrate. Second, because of their high spatial coherence, laser pulses can be focused to small areas, and the pulse energy is absorbed in a small volume. Laser pulses with durations in the range of 10^{-13} – 10^{-8} s have been used to achieve temperatures sufficient for melting a layer of silicon near the surface, typically 50–500 nm thick [28–30]. Because this thin layer of laser-melted material is resting atop a room temperature lattice, the heat flux away from the molten region is high, and the resolidification front moves quickly through

the material, potentially exceeding 10 m/s [11, 31]. The standard Czochralski crystal growth process, in comparison, typically involves resolidification fronts with speeds of about 10^{-5} m/s [32].

As the resolidification-front velocity approaches 1 m/s, thermodynamic equilibrium cannot be established at the liquid-solid interface [11]. As a result, dopant atoms present in the melt are trapped in the solid silicon above their equilibrium solubility limit, a process known as solute trapping [11, 12, 33]. According to well-tested predictive models, faster resolidification velocities yield higher dopant concentrations [11, 12, 30, 34]. At sufficiently high resolidification velocities (>15 m/s), however, solute segregation [35, 36] and loss of crystalline order [37] during resolidification occur. Figure 1.2 shows a sulfur concentration profile after fs-laser irradiation

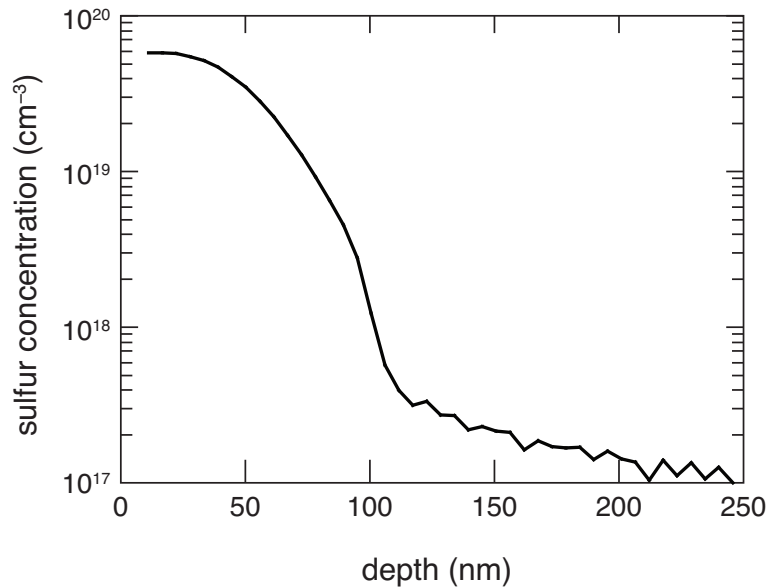


Figure 1.2: Sulfur concentration obtained by secondary ion mass spectrometry after pulsed-laser hyperdoping with 800-nm fs-laser pulses in a SF_6 atmosphere at a pressure of 500 Torr. S concentration near the surface is 6×10^{19} cm^{-3} , three orders of magnitude larger than the solubility limit of S in silicon. Adapted from Reference [38].

of silicon in a sulfur-rich atmosphere. The sulfur concentration approaches 10^{20} cm^{-3} near the surface, about three orders of magnitude above the solid solubility limit [39].

Dopants can be introduced into the host material via diffusion from a dopant-rich atmosphere while the substrate is molten. Introducing the dopants via ion implantation prior to laser melting is more common, however [11]. In the case of diffusion into molten silicon, the dopant precursor can be a gaseous ambient or a thin solid film on top of the silicon. Pulsed-laser hyperdoping of heavy chalcogen (S, Se, and Te) in silicon has been achieved via all of the methods mentioned previously using femtosecond [4, 8, 15] picosecond [15], or nanosecond [5, 6, 8, 15, 21] laser pulses.

The heat-transfer and resolidification processes described previously are common to laser-induced melting using pulses with durations of tens of nanoseconds and shorter. However, the duration of laser pulses used for hyperdoping ranges over five orders of magnitude, and significant differences occur across these timescales. For femtosecond pulses, laser energy is deposited into the material well before heat diffusion occurs. First, electrons absorb the energy of the laser pulse, and then this high-temperature electron gas transfers energy to the cold lattice through electron-phonon coupling on a picosecond timescale [27]. In addition, nonlinear absorption reduces the photon penetration depth, and the pulse energy is deposited in a very thin layer, lowering the energy threshold for melting [40]. In this case, the resolidification-front velocity can greatly exceed the liquid-to-crystal relaxation rate, yielding resolidification into an amorphous phase [37, 41]. For nanosecond laser pulses, the absorption process is linear, and the absorption length is larger. Thus, deeper melt depths and dopant distributions can be achieved. The temperature gradient across the molten

layer and the solid substrate is smaller than for a laser pulse of femtosecond duration, resulting in a longer melt duration and slower resolidification-front velocity. Therefore, ns-laser hyperdoped silicon is often crystalline, while fs-laser hyperdoped silicon often has an amorphous or polycrystalline structure [8, 38]. To summarize, the duration of a laser-pulse determines the kinetics of melting and resolidification, and hence significantly impacts dopant incorporation and changes in crystal structure.

1.2.2 Hyperdoping with femtosecond lasers

We now discuss the “black silicon” process: hyperdoping silicon with heavy chalcogen atoms via irradiation with 100-fs, 800-nm Ti:sapphire laser pulses. The dopants are introduced via a chalcogen-rich ambient, such as gaseous sulfur hexafluoride (SF_6) or a thin solid film of Se or Te (deposited on the silicon surface via thermal evaporation prior to laser irradiation). After fs-laser hyperdoping, the chalcogens are incorporated at concentrations of about 1 at.% [2, 7]—greater than the equilibrium solubility [39, 42, 43] by a factor of 10^3 . This process can be tuned to simultaneously produce a light-trapping surface texture (Section 1.3) in addition to hyperdoping. We emphasize that with an appropriate choice of laser parameters, hyperdoping can be achieved without surface texturization [3].

The optical absorptance of silicon hyperdoped with sulfur is shown in Figures 1.1b and 1.1d. In Figure 1.1b, the laser treatment was designed to avoid any surface texturization and shows that hyperdoping is responsible for the sub-bandgap absorption. In Figure 1.1d, absorptance is plotted for samples that have been both hyperdoped as well as textured. Combining hyperdoping and surface texturing, ab-

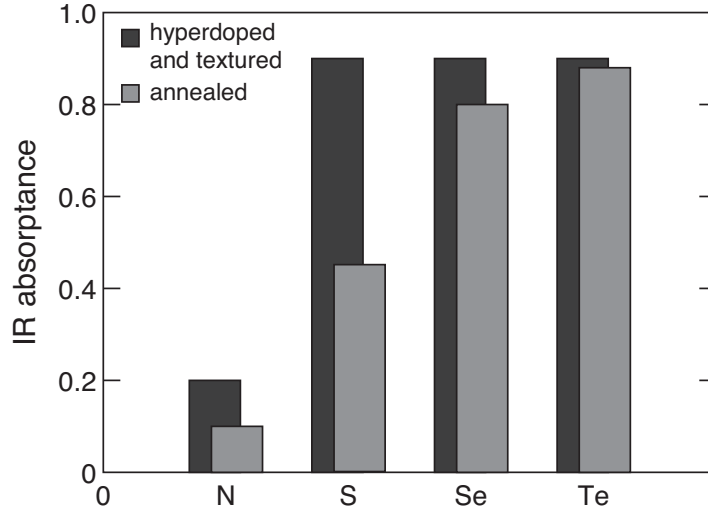


Figure 1.3: Average infrared ($\lambda = 1.25$ to $2.5 \mu\text{m}$) absorptance of chalcogen hyperdoped silicon before and after annealing (775 K, 30 min.), represented by dark and light gray bars respectively. Samples are irradiated in the presence of a sulfur dopant precursor (SF_6 or H_2S) (S), selenium (Se), or tellurium (Te). Adapted from References [7] and [44].

sorptance is near unity for both above and below bandgap light. The absorptance for silicon hyperdoped with Se and Te is nearly identical to that of silicon hyperdoped with S (shown in Figure 1.1d) [7]; Figure 1.3 shows the average infrared (IR) absorptance of optical wavelengths 1.25 to $2.5 \mu\text{m}$ for samples irradiated with and without chalcogen dopant precursors. Chalcogen-hyperdoped silicon exhibits broadband absorption extending to photon energies less than the bandgap of silicon. Three observations indicate that the high chalcogen concentration is responsible for this broadband, sub-bandgap absorption. First, we observe the broad sub-bandgap absorption if and only if a heavy chalcogen is present. We have experimented extensively with other dopants [45, 46] and phases of dopant precursors (solid [7, 44] versus gaseous [45]) and demonstrated that the presence of the chalcogen dopant is necessary

and sufficient for strong sub-bandgap absorption. We show a selection of these data in Figure 1.3. Second, the sub-bandgap absorption decreases after thermal annealing in a manner directly related to the specific chalcogen-dopant used [2, 44]. Figure 1.3 shows the average IR absorptance following a 30 min. anneal at 775 K for various dopants. The absorptance decreases at rates that are governed by the chalcogen-dopant diffusivity in silicon. For example, Te atoms have the lowest diffusivity among chalcogen atoms; consequently, the sub-bandgap absorptance of a Te-doped sample changes least after annealing. A chalcogen-dopant diffusion model explains the correlation between infrared absorption and the thermal treatment [44]. Lastly, silicon hyperdoped with chalcogens using a different technique (ion implantation followed by nanosecond pulsed laser melting) exhibits similar sub-bandgap absorption [5, 6]. Thus, regardless of the hyperdoping method, silicon hyperdoped with approximately 1 at.% of heavy chalcogens exhibits broadband absorption of photons with energy less than the bandgap of silicon.

The origins of this absorption can be understood by considering the energy states of the chalcogens in silicon [47]. Dilute concentrations of sulfur introduce a variety of occupied electronic states (arising from point defects, dimers, and more complex structures) that reside 100–300 meV below the conduction band edge of silicon; as a result, the sulfur dopants are electron donors [48]. As the sulfur-concentration increases, new atomic configurations become likely, and these energy levels shift and broaden [49]. Low energy photons can be absorbed by exciting electronic transitions between the band edges and the energy states introduced by sulfur. Thus, the presence of these states and the electronic transitions they facilitate are most likely responsible

for the observed extended infrared absorption.

Finally, absorption of these sub-bandgap photons yields mobile charge carriers. Using sulfur as both an electron donor and as an optically sensitive defect, we have fabricated a variety of optoelectronic devices based on the junction formed between the substrate and the hyperdoped region [48, 50, 51]. For example, we demonstrated photodiode devices that respond to sub-bandgap photons [48], with a measurable photoresponse at photon energies as low as 0.8 eV. Thus, it is unlikely that free-carrier absorption [52] and structural-defect absorption [53] are responsible for this sub-bandgap absorption. Both of these effects enable absorption of sub-bandgap photons, but do not increase the population of mobile charge carriers, and therefore the absorbed energy cannot be extracted. In addition, the broad, featureless absorption shown in Figure 1.1b and 1.1d does not exhibit the predicted wavelength dependence of these effects.

1.2.3 Applications to photovoltaics

Next we consider the question of whether the strong sub-bandgap absorption of hyperdoped silicon can be used to increase photovoltaic efficiency. The idea of using dopants to increase absorption of low-energy photons (and thus increase PV cell efficiency) has a long history. The first proposal, suggested over 50 years ago, focused on using deep-level impurities to enhance absorption [54]. This concept, now further developed, is known as the impurity photovoltaic (IPV) effect [55]. The principle of an IPV cell is to convert below-bandgap photon energy to electron-hole pairs through a two-stage, defect-assisted absorption process illustrated in Figure 1.4a. However,

deep electronic states are highly localized [56]; their presence introduces localized pockets of charge that disrupts the local electrostatic potential in the silicon lattice and leads to increased non-radiative recombination rates [56]. Thus, efforts to increase absorption through the inclusion of such states yield shorter carrier lifetimes and lower open-circuit voltage; consequently, cell efficiency can only be increased by 1–2% (absolute) using this method [55]. On the other hand, it was recently pointed out that

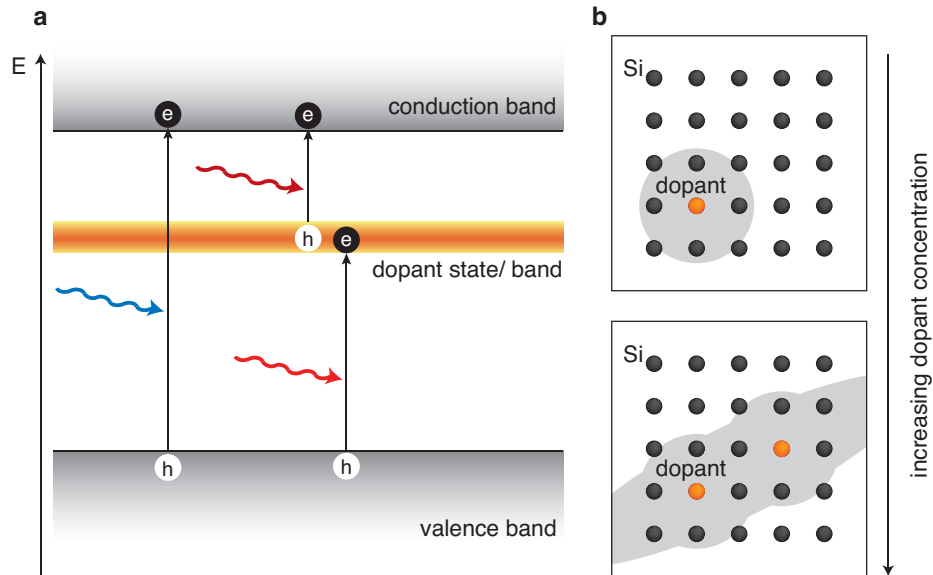


Figure 1.4: (a) Schematic of light absorption process. Photons with energy smaller than the bandgap energy excite electrons either from the valence band to the dopant state/ band, or from the dopant state/ band to the conduction band. (b) Illustration of a crystal of atoms (black) with dopants (orange) and the electron wave functions of the dopant electrons (gray). The electron wavefunction become delocalized if the concentration of the dopants is increased above the insulator-to-metal transition.

if such impurity states were included in high enough concentrations that their electronic states delocalize (through a Mott insulator-to-metal transition, for example), high recombination rates might be avoided (Figure 1.4b) [57]. Such an intermediate band photovoltaic (IBPV) material could convert sub-bandgap photons to current

without decreasing the open-circuit voltage in the cell, thus achieving a theoretical energy-conversion efficiency of $>63\%$, significantly higher than the 41% efficiency limit of a standard single-junction solar cell (under concentrated sunlight) [58, 59]. Fabricating an IBPV, however, is difficult, and no current design has demonstrated the theoretically predicted efficiency improvements [13, 60].

Pulsed-laser hyperdoping yields a material that exhibits several of the characteristics expected from an IBPV material. First, chalcogen-hyperdoped silicon exhibits strong photon absorption and measurable photoresponse for sub-bandgap light. Second, we have recently observed evidence that a insulator-to-metal transition occurs in silicon hyperdoped with chalcogens [61]. As mentioned previously, such a delocalization transition is a necessary condition to avoid strong non-radiative recombination due to localized deep states. Currently, there are contradicting reports on the feasibility of this lifetime recovery effect [62, 63]. With both experimental and theoretical work devoted to investigating the mechanism and impact of intermediate band formation in hyperdoped silicon [61, 64–66], we are evaluating this material as a potential intermediate band system that could effectively capture the energy of sub-bandgap photons.

1.3 Surface texturization

Pulsed lasers are uniquely suited for hyperdoping because they heat small volumes of silicon over short timescales; for the same reason, they are also well-suited for creating surface texture. By providing highly localized heating, pulsed lasers can remove material through ablation to create surface texture. Their coherent properties

lead to surface roughness with a characteristic length scale tunable by appropriate wavelength selection. We begin this section with a brief description of how pulsed-laser surface texturization occurs, and then explain its application to geometric light trapping in photovoltaics.

1.3.1 Pulsed-laser surface texturization

The physics of pulsed-laser texturization originates with the same processes described in the section on laser melting and doping. Because of interference between the incident laser pulse and self-scattering from surface defects, the energy deposited by a single laser pulse varies across the irradiated surface. This interference effect, which occurs over distances comparable to the incident laser wavelength, yields periodic variations in melt depth. Capillary waves, excited spontaneously in the melt, freeze in place during resolidification to form features known as laser-induced periodic surface structures (LIPSS). The periodicity of LIPSS is related to the wavelength and polarization of the incident light [67–69]. With subsequent laser pulses, the ripple pattern coarsens and “beads up [1].” Subsequent laser pulses are thus incident on a modulated surface and focus preferentially into the “valleys” of these features [70]. If the energy deposited in these valleys is sufficient to raise the temperature above the boiling point, the molten silicon becomes superheated and begins to boil. Additional increases in energy can lead to a significant increase in the rate of material removal, a process known as ablation [29]. Some material leaves the surface as superheated particles, a process that can be visualized and understood with molecular dynamics simulations [71]. Pulsed-laser irradiation on LIPSS thus initiates positive feedback:

surface texture leads to preferential focusing, which leads to selective ablation, which leads to additional surface texture. Although pulsed-laser texturing has been observed after irradiation with fs-, ps-, and ns-laser pulses, the fluence (energy per area) and pulse number requirement is lowest for fs-lasers [15]. In addition, the ambient environment has a large effect on the structure [46, 72]. The detailed evolution of the silicon spikes shown in Figure 1.5a is documented in Reference [1] along with a thorough review of relevant literature. The exact details of surface formation depend on a large number of parameters, but the description here explains the surface texturization qualitatively.

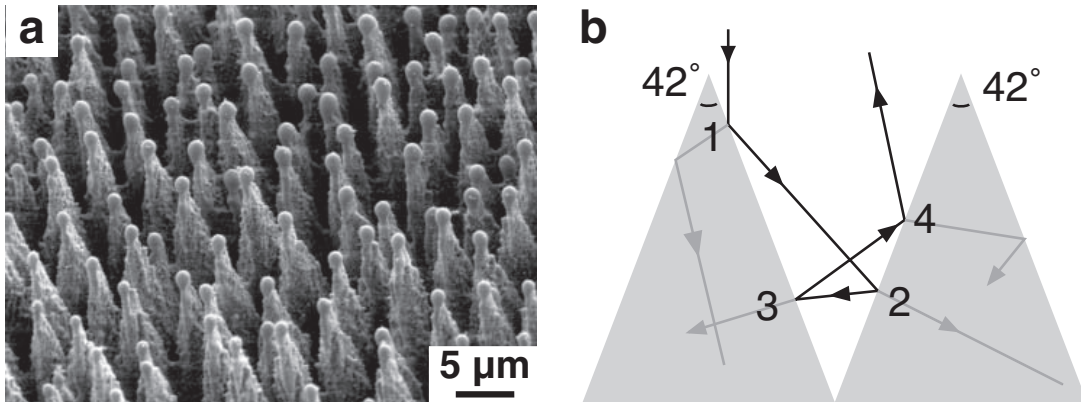


Figure 1.5: (a) Scanning electron micrographs of a silicon surface after irradiation with 600 fs-laser pulses at 8 kJ/m^2 at a SF_6 pressure of 500 Torr. The scanning electron microscopy image is taken at a 45° angle to the surface. (b) Illustration of the optical path of light incident on laser-textured silicon surfaces, with cones subtending 42° . Adapted from References [1] and [73].

Figure 1.5a shows the surface that results from the irradiation of silicon with normally incident 600 fs-laser pulses at 8 kJ/m^2 in an SF_6 atmosphere at a pressure of 500 Torr. We have extensively explored the degree to which these surfaces can be engineered, and both micrometer- [74, 75] and nanometer-scale [72, 76] surface roughness can be fabricated. For example, the height and spacing of the spikes depends

on laser wavelength, fluence, number of laser pulses, pulse duration, and ambient environment. Furthermore, formation of these spikes is independent of the crystalline orientation of the substrate [75], enabling the fabrication of light trapping surfaces on thin polycrystalline or amorphous films [77]. The manner in which irradiation parameters affect light absorption enhancement is documented in References [2, 4, 45, 46]. The absorptance of fs-laser textured silicon is plotted in Figures 1.1c and 1.1d. The reflectance of the laser-textured surface is low [46]; hence absorptance is near unity from $0.24 \mu\text{m}$ to at least $1.1 \mu\text{m}$.

1.3.2 Geometric light trapping

Geometric light trapping from micrometer-sized silicon spikes decreases reflection and enhances optical path length. The height, spacing, and subtended angle determine the extent of geometric light trapping. For spike heights on the order of $1 \mu\text{m}$ or larger, the structures are large enough that graded density [78] does not play a role for visible and near-IR light, and multiple reflection on the surface is the dominant effect of light trapping. Treating the case of spikes subtending a cone angle of 42° , the average angle observed in Figure 1.5a, normally incident light undergoes four reflections on average before escaping the surface (Figure 1.5b) [73]. The small cone angle outperforms chemically etched silicon pyramids, a common light-trapping structure that forms a 71° angle and yields only two reflections for normally incident light. As a result, less than 5% of the incident light is reflected. Furthermore, because the total internal reflection angle for silicon is approximately 14° , light transmitted into the silicon spikes reflects inside the spikes and greatly enhances the path length (Figure 1.5b).

Therefore, enhanced absorption is evident even for weakly absorbed photon energies near the bandgap. For example, at an optical wavelength of $1.1 \mu\text{m}$ (for which the absorption length in silicon is 3 mm) the absorption of light is still above 60%, significantly higher than it would be for a planar $400\text{-}\mu\text{m}$ silicon wafer (10%) [79].

Femtosecond-laser textured silicon is excellent at light trapping; however, the laser irradiation process produces structural modifications near the silicon surface that must be considered when applying this technique to fabricate high-efficiency photovoltaics. For example, the fs-laser surface texturization produces a polycrystalline layer approximately 100 nm thick near the surface [2]. Similar to heavily doped emitter regions, this layer likely exhibits a low minority carrier lifetime and could lower the efficiency of a photovoltaic device. To address this concern, thermal annealing could be used; alternatively, the polycrystalline layer can be etched away. In this fashion, fs-laser surface-textured silicon has been applied to solar cell fabrication: Nayak *et al.* use chemical etching and annealing to remove defects that form during pulsed laser irradiation and achieve 14% conversion efficiency [80]. Nayak *et al.* demonstrated integration of pulsed-laser textured surfaces with standard silicon solar cell fabrication. Finally, good light trapping can also be obtained with nanosecond lasers. Due to the slower resolidification front velocity in ns-laser melted silicon, such samples do not exhibit a polycrystalline region near the surface [8].

1.4 Summary

The outlook for pulsed lasers as tools for photon management in photovoltaics is bright. Pulsed laser processing provides two routes for photon management in pho-

tovoltaics. Surface texture achieved using intense pulsed-laser light to create quasi-periodic surface features reduces reflection and increases path length through the material. In addition, pulsed-laser hyperdoping processes alter the absorption coefficient of silicon through the inclusion of a non-equilibrium concentration of deep states in silicon. Hyperdoping is a potential route to realizing an intermediate band photovoltaic device. Hyperdoping and surface texturization are distinct and independently achievable. Although both techniques show promise for effective photon management, research challenges for implementing either method remain. Growing research interest in pulsed laser techniques, however, is yielding rapid progress in addressing these challenges.

1.5 Organization of the dissertation

This thesis reports (1) our progress in controlling the material quality and dopant concentration of the fs-laser hyperdoping process, and (2) our effort in identifying the energetics of the chalcogen dopants via electronic transport and mid-infrared light absorption measurements.

Chapter 2 describes the main experimental methods used in the thesis. We describe in detail the development of the fs-laser hyperdoping process compared to previous work.

Chapter 3 investigates fs-laser doping mechanism with gas-phase dopant precursor. We study fs-laser hyperdoping with few laser pulses below the ablation threshold to understand the mechanism on how the sulfur dopant diffuses into silicon. The goal is to develop methods to control dopant concentration by varying the pressure of the

dopant precursor.

In Chapter 4, we study the electronic properties of silicon hyperdoped with sulfur at different concentrations. Through analyzing temperature-dependent transport data, we analyze the properties of the intermediate band.

Chapter 5 presents the mid-infrared absorptance of chalcogen hyperdoped silicon. In this wavelength region, the light and matter interaction is more complicated than described in Section 1.3.2. After careful analysis, we place an upper bound on the position of the intermediate band.

Chapter 6 presents a method to reactivate sub-bandgap light absorption. This chapter addresses the issue that after fs-laser hyperdoping, an annealing step is necessary for fabricating devices, but annealing also reduces sub-bandgap light absorption. This chapter shows our progress toward fabricating a device that maintains its sub-bandgap light absorption.

Chapter 7 summarizes the main results obtained in this thesis and proposes future avenues of research to address several still unanswered questions regarding fs-laser hyperdoping and material properties of intermediate band systems.

Appendix A provides information on the Hall effect analysis presented in Chapter 4.

Appendix B provides methods to correct absorption data obtained with an integrating sphere.

Appendix C discusses the photovoltaic potential of using fs-laser texturing on amorphous silicon solar cells.

Chapter 2

Experimental methods and updates

The experimental setup used in this thesis is slightly different from previous work [3, 77, 81]. In this chapter we describe the “standard operating procedures” adopted in this thesis. We also list updates to previous work such as the influence of ambient pressure on surface morphology and connections between samples fabricated via stationary and scanning laser pulses.

2.1 Sample fabrication

We use amplified femtosecond laser pulses of temporal duration $\tau < 100$ fs and center wavelength $\lambda = 800$ nm. The maximum pulse energy is 2.5 mJ and the maximum repetition rate is 1 kHz. The laser is linearly polarized and has an approximately Gaussian spatial profile. The schematics of the experimental setup are shown in Figure 2.1 and 2.2. A stationary laser beam and a set of stepper motors are used when precise control of the hyperdoping area is desired (Figure 2.1). A fiber lamp

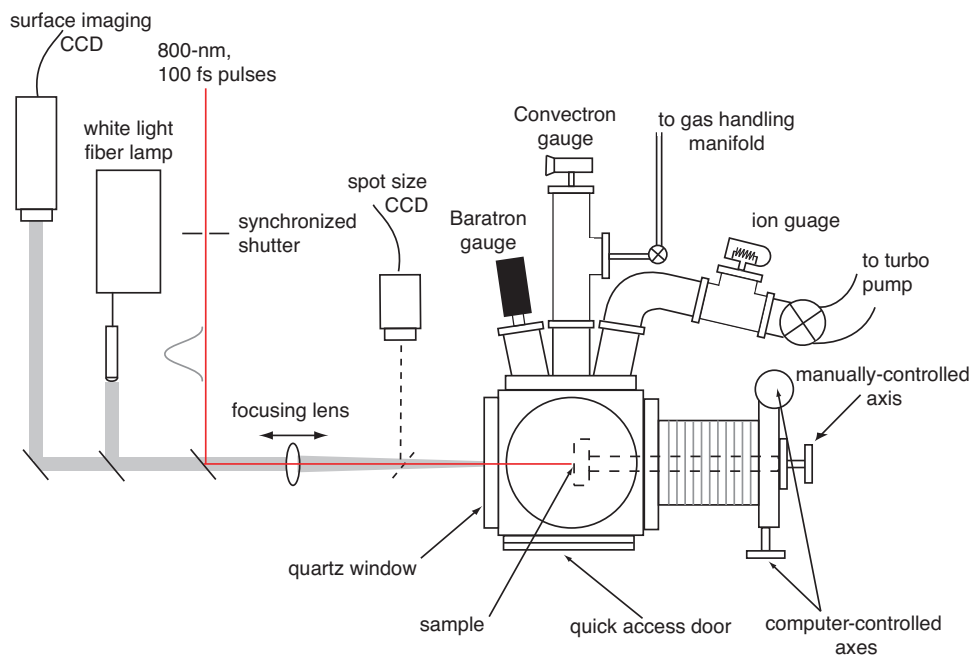


Figure 2.1: A schematic diagram of the fs-laser hyperdoping apparatus using a stationary laser beam and two-axis stepper motors to translate the sample.

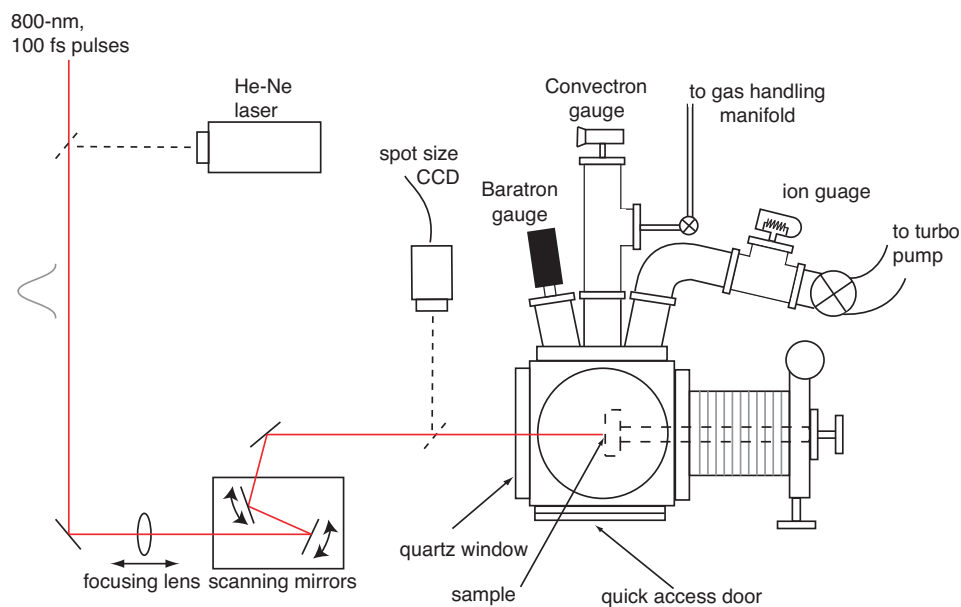


Figure 2.2: A schematic diagram of the fs-laser hyperdoping apparatus with the sample held stationary and a set of Galvo scanning mirrors scanning the laser beam across the sample surface.

and a CCD camera allow in situ imaging and alignment. We also use a synchronized mechanical shutter to control the number of laser pulses delivered to the sample.¹ When a large hyperdoping area is desired, we use a pair of galvanometric scanning mirrors to scan the laser pulses across the silicon surface (Figure 2.2). We use a HeNe laser beam path for sample alignment. Using the scanning mirror system, sample fabrication is 40 times faster than using the stepper motors.

The three parameters that are important in determining the dopant concentration and surface morphology are (1) the pressure of the dopant precursor or background gas, (2) the fluence (energy per area) of the laser at the sample's surface and (3) the number of laser pulses delivered to the sample.

2.1.1 Ambient pressure

Silicon samples are placed inside a stainless steel vacuum chamber (Figures 2.1 and 2.2) where a variety of different dopant precursor (SF_6) or background gases (N_2 or H_2) are introduced. We use the Baratron gauge to measure the chamber pressure (ranging from 0.1 to 760 Torr) because the Baratron gauge readout is independent of the type of gas being measured. The pressure measurement error associated with the Baratron gauge is ± 0.1 Torr for $P < 40$ Torr and $\pm 0.25\%$ otherwise. The convectron gauge and the ion gauges are used to monitor the vacuum base pressure. These two types of gauges are only calibrated for nitrogen.

¹The minimum exposure time of the shutter is 6 ms. We use repetition rate ≤ 100 Hz to deliver a single pulse

2.1.2 Fluence

Experiments in this thesis use fluence between 2.5 kJ/m² and 8.0 kJ/m². We use the focusing lens shown in Figures 2.1 and 2.2 to adjust the size of the laser spot at the silicon surface. On the other hand, we adjust the pulse energy by using a half-wave plate to rotate the pulse polarization before the pulse enters the compressor (not shown). The pulse compressor is polarization dependent, so we achieve continuous adjustment between 50 μJ and 2.5 mJ by using the half-wave plate. It is important to note that the wave plate does influence the output beam profile and we observe hot spots and distortion of the Gaussian beam. The distortion has no significant effect on our experimental results.

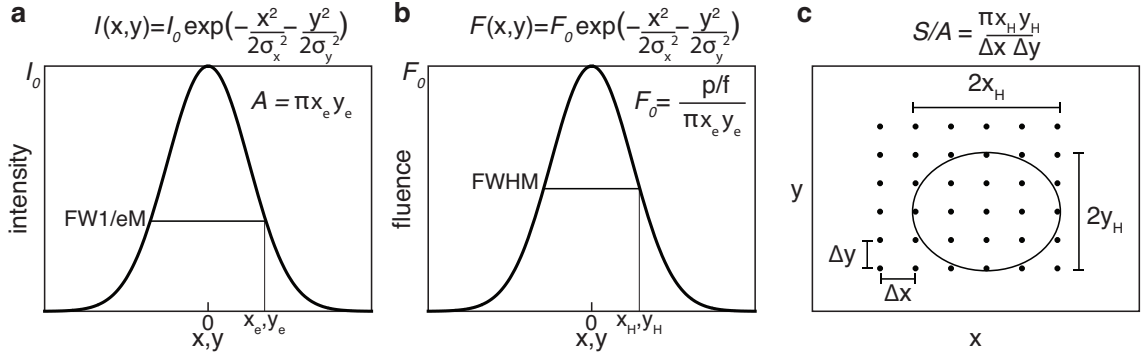


Figure 2.3: Key parameters for calculating the fluence and shots per area. (a) Illustration of a Gaussian intensity beam profile. (b) The fluence is $F = \frac{P/f}{A}$, where $A = \pi \cdot x_e \cdot y_e$. The local fluence profile is also Gaussian. (c) Illustration of the scanning pattern. The oval represents the area (defined by FWHM) of one laser pulse. Each dot represents the center of the Gaussian beam when a pulse arrives at the sample surface. The pulses are separated by Δx and Δy in the x and y-direction respectively. *shots per area* is $S/A = \frac{\pi \cdot x_H \cdot y_H}{\Delta x \Delta y}$.

The general equation for fluence is $F = \frac{E}{A} = \frac{P/f}{A}$, where E is the energy per pulse, A is the spot size, P is the power, and f is the repetition rate of the laser pulses. The laser intensity profile is Gaussian, $I(x, y) = I_0 \exp(-\frac{x^2}{2\sigma_x^2} - \frac{y^2}{2\sigma_y^2})$, where I_0 is the

peak intensity at the center of the Gaussian beam, and σ_x and σ_y are the standard deviation in the x- and y-direction respectively (Figure 2.3). Sometimes different research groups report fluence calculated using a different definition of area such as full-width-at-half-max (FWHM), full-width-at-1/e-max (FW1/eM), or full-width-at-1/e²-max (FW1/e²M), and hence this leads to discrepancies of fluence reported in the literature. For our fluence calculation, we use the area that corresponds to the FW1/eM of the Gaussian intensity profile. The radius x_e and y_e corresponds to $I(x_e, 0) = I(0, y_e) = I_0 e^{-1}$, $x_e = \sqrt{2}\sigma_x$, $y_e = \sqrt{2}\sigma_y$, and the area is $A = \pi \cdot x_e \cdot y_e$.

The total power within a pulse is $P = \int \int_{-\infty}^{\infty} I(x, y) dx dy = I_0 \pi (\sqrt{2}\sigma_x) (\sqrt{2}\sigma_y)$. The latter two terms correspond to x_e and y_e . Using the area defined by FW1/eM, $A = \pi x_e \cdot y_e$, the fluence F is also the peak fluence F_0 of the local fluence profile: $F = \frac{P/f}{A} = \frac{I_0 \pi (\sqrt{2}\sigma_x) (\sqrt{2}\sigma_y) / f}{(\pi x_e y_e)} = I_0 / f = F_0$. The local fluence profile is also a Gaussian (Figure 2.3b),

$$F(x, y) = F_0 \exp\left(-\frac{x^2}{2\sigma_x^2} - \frac{y^2}{2\sigma_y^2}\right).$$

2.1.3 Shots per area: the average number of laser pulses delivered to the sample

Since the laser beam has a Gaussian profile, when laser scans across the surface, the surface of the sample receives a range of laser fluences [82, 83]. Instead of reporting the detail scanning parameter such as scanning speed and pulse separation distances, we report the average number of laser pulses delivered to the sample, called *shots per area*, S/A (Figure 2.3c):

$$S/A = \frac{\pi x_H y_H}{\Delta x \Delta y},$$

where x_H and y_H are FWHM of the local fluence (Figure 2.3b). If S/A is 25, that means any given point on the sample receives 25 laser pulses with a local fluence above $F_0/2$.

Once the spot size is set by the fluence parameter, we achieve the desired S/A by adjusting the scanning speed v (either the speed of stepper motor or speed of the scanning mirrors). We scan the laser pulses using a raster scanning pattern; the laser pulse travels in the +x-direction, step a distance Δy in the y-direction, and then travels in the -x-direction. The separation distance between pulses is $\Delta x = v/f$, where f is the repetition rate. In this thesis the repetition rate of the laser pulses is 25, 100 or 1000 Hz. To ensure the sample is as homogenous as possible, we set $\Delta y/\Delta x = y_H/x_H$ [3].

To summarize, in the experiments described in this thesis, we set the ambient pressure in the vacuum chamber between vacuum (10^6) and 760 Torr. We adjust the energy per pulse and the spot size to achieve the desired fluence. We adjust the velocity of the stepper motor or the scanning mirrors and sometimes the repetition rate of the laser to achieve the desired shots per area. The fluence and shots per area parameters use in this thesis is lower than our earlier work [77, 81], because the sample produced are with smaller surface roughness and hence are easier to make good electric contacts to. In Chapter 3 and Chapter 4, we use fluence at 2.5 kJ/m^2 , and $S/A = 50$ to minimize the surface roughness. In Chapter 5 and 6 we perform hyperdoping at $F = 4 \text{ kJ/m}^2$, $S/A = 80$ for Se- or Te-hyperdoping; $F = 8 \text{ kJ/m}^2$, $S/A = 50$ for S-hyperdoping.

2.2 Stationary and scanning pulses

With increasing fluence, the silicon is heated, melted, or ablated after laser irradiation. Moreover, phase transformations also occur so the resulting material can be crystalline or amorphous [41]. Across the Gaussian fluence profile, all the above interactions can occur. In addition to optimizing the scanning pattern discussed in Section 2.1, there is also a minimum shots per area before the average laser interaction with silicon is homogeneous. In Figure 2.4, we show that the laser interaction with silicon using a small number of laser pulses and study the effect of overlapping laser pulses on phase transformations.

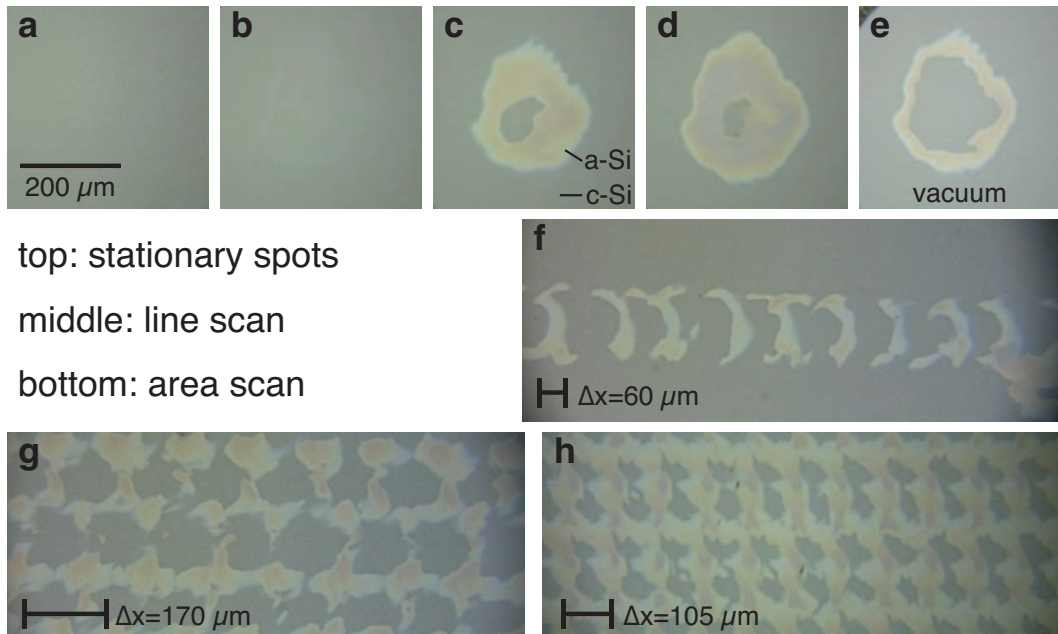


Figure 2.4: Optical microscope images of silicon surface after fs-laser irradiation at 2.5 kJ/m^2 at a SF_6 pressure of 100 Torr. Top row shows stationary laser irradiations after (a) 1, (b) 2, (c) 4, and (d) 6 laser pulses. (e) is a sample irradiated by 6 laser pulse in vacuum. Middle and bottom rows show (f) a line scan, (g) an area scan, and (h) a sample irradiated at 2.0 kJ/m^2 . At a fluence of 2.5 kJ/m^2 and the scanning condition same as (h), the sample surface becomes rough.

The fluence above the melting threshold is necessary for laser doping while laser texturing is dominated by energy above the ablation threshold. We measured the melting threshold of silicon as 2.1 kJ/m^2 [38]. We tested many different parameters above the melting threshold and found that at 2.5 kJ/m^2 , the center of the laser spot is crystalline and the surface is free of laser-induced periodic surface structures (LIPSS) up to 6 laser pulses.

We study the effect of irradiating with additional laser pulses with and without translating the sample. We examine irradiating silicon with 1 to 6 laser pulses on the same position. Figures 2.4a – 2.4d show optical microscope images of samples after irradiation with 1, 2, 4 and 6 laser pulses at a fluence of 2.5 kJ/m^2 at a SF_6 pressure of 100 Torr. The laser spot size (FWHM) is $560 \mu\text{m}$. The color contrast in Figure 2.4c and 2.4d indicates presence of amorphous silicon. This amorphous ring is not visible after irradiating with the first laser pulse, and a very faint contrast is visible after the second laser pulse. The size of the amorphous area increases with the number of laser pulses. At this fluence LIPSS develops after irradiating with more than 6 laser pulses. Figure 2.4e shows the size of the amorphous ring depends on the processing pressure; at vacuum, the area of amorphous silicon is smaller compared to Figure 2.4d. This suggests that the resulting material crystallinity is affected by both the resolidification dynamics and presence of defects and or dopants. Figures 2.4a – 2.4e show that additional laser pulses have a large impact on the crystallinity of the material.

In addition, we scan the laser pulses over a line and an area. Figure 2.4f shows a line scan of the same laser pulses with separation $\Delta x = 60 \mu\text{m}$. Figure 2.4g shows the

result of an area scan with $\Delta x = \Delta y = 170 \mu\text{m}$. We identify the amorphous silicon shown in Figures 2.4f – 2.4h corresponds to the edge of the laser pulses. Gimpel *et al.* also report that overlapping laser pulses leads to extra amorphization [84].

Scanning laser pulses is necessary to fabricate a sample of a large area. The non-uniform interaction across the Gaussian beam profile leads to a material that is not uniform when processing at low S/A . Therefore, overlapping large number of laser pulses is necessary to ensure the sample is homogeneous. On the other hand, overlapping large number of laser pulses also leads to laser texturing. Performing material characterization on a rough surface is challenging, so we want to minimize the surface roughness as much as possible. We observe that the surface of samples fabricated at $S/A = 50$ appears uniformly rough and the height of the laser textures are smaller than $2 \mu\text{m}$. In this thesis, we choose $S/A \geq 50$ when fabricating large area samples.

2.3 Influence of SF_6 pressure on surface morphology

The surface morphology of fs-laser irradiated silicon varies with different background gas [45, 46]. The conical spikes are sharper when silicon is processed in sulfur hexafluoride (SF_6) because fluorine radicals react with silicon and etch away silicon at the surface. In this thesis, we vary the pressure of SF_6 to control the sulfur concentration in the hyperdoped material. Understanding how the surface morphology changes under different pressures of SF_6 is important. Pressure dependence of hyperdoped silicon has been reported by Crouch *et al.* [2]. They fabricated S-hyperdoped silicon at 8 kJ/m^2 with 500 laser pulses and observed absorption increases with the

pressure of SF₆. The laser fluence and S/A used in this thesis are lower (≤ 8 kJ/m² and $\leq 100 S/A$). We observed that at some combination of SF₆ pressure, fluence and S/A , the hyperdoping is not effective.

We fabricate S-hyperdoped silicon using fs-laser with spot size of 500 μ m (FWHM). Using a combination of different fluences and S/A , we fabricate a set of samples at pressures of SF₆ between 1 and 760 Torr. In addition, we also fabricate a set of samples with the same conditions in a nitrogen environment.

Figures 2.5 and 2.6 are representative top-view and 45-degree SEM images of the samples. When fabricated with higher fluence and higher S/A , the conical spikes are bigger [70]. When fabricating in SF₆, the surface tends to be rougher with higher pressure. In general this agrees with Ref. [2]. There is, however, an exception when processing at pressure higher than 500 Torr. The lower left figure of Figures 2.5 and 2.6 shows that at 2.5 kJ/m², 50 S/A , and 500 Torr, the surface of the sample is composed of ripples and irregular small spikes. Similarly the spikes fabricated at 500 Torr with $F = 2.5$ kJ/m², $S/A = 100$ and $F = 4$ kJ/m², $S/A = 50$ are also smaller than the spikes fabricated under 100 Torr of SF₆.

As a comparison, Figures 2.7 and 2.8 show SEM images of samples fabricated in N₂ ambient gas. When fabricated with higher fluence and higher S/A , the observation is the same as above, the surface structures are bigger. However, the surface morphologies of sample fabricated in N₂ shows no pressure dependence. Since the nitrogen gas has no significant interaction with the silicon surface, the surface morphology is independent of the N₂ pressure. On the other hand, the pressure of the SF₆ has a large influence of the surface morphology. We did extensive tests and

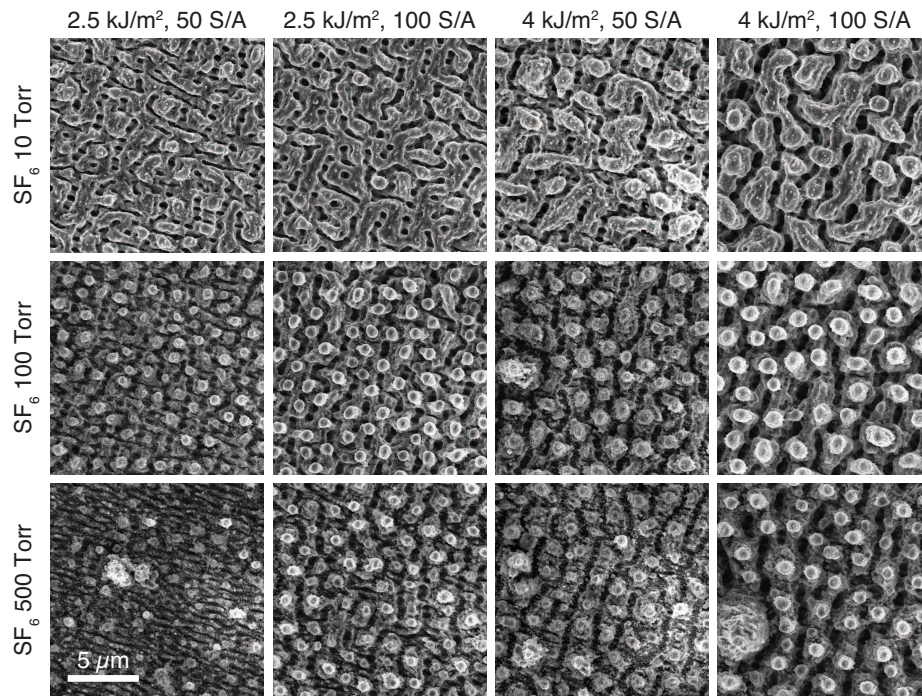


Figure 2.5: Top-view SEM images of silicon surface after laser irradiation at different fluence, S/A, and SF₆ pressure. Each column corresponds to a different set of irradiation condition, and each row corresponds to a different SF₆ pressure.

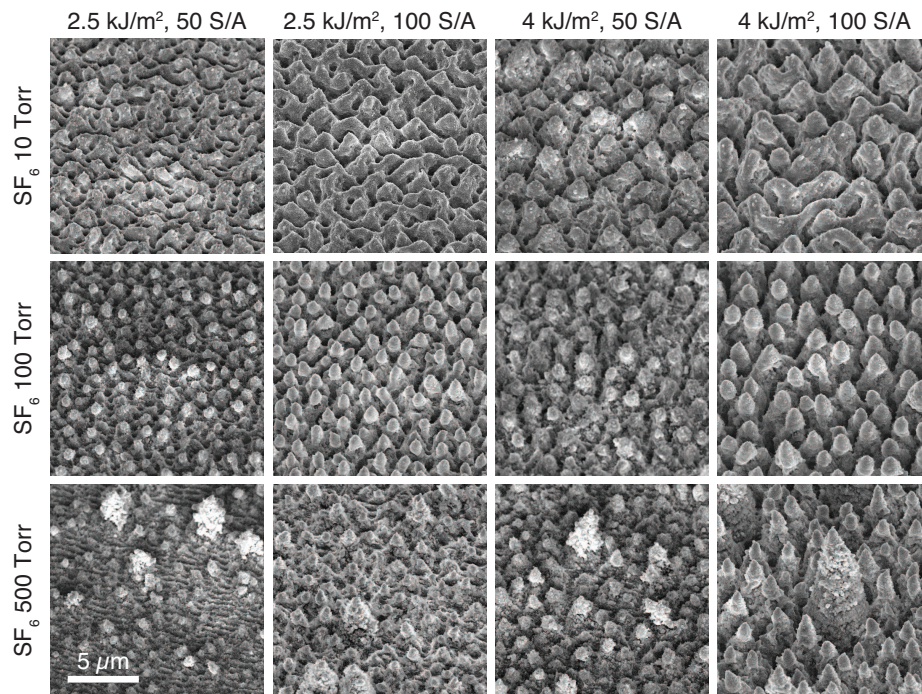


Figure 2.6: 45-degree SEM images of silicon surfaces shown in Figure 2.5.

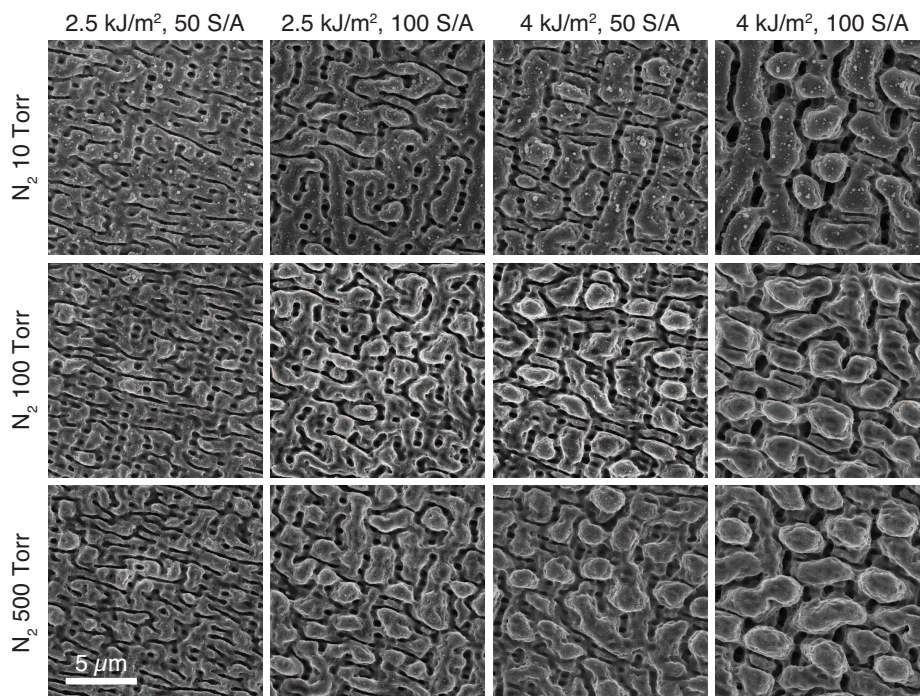


Figure 2.7: Top-view SEM images of silicon surface after laser irradiation at different pressures of nitrogen. The fabrication condition is the same as Figure 2.5 except in a nitrogen ambient environment.

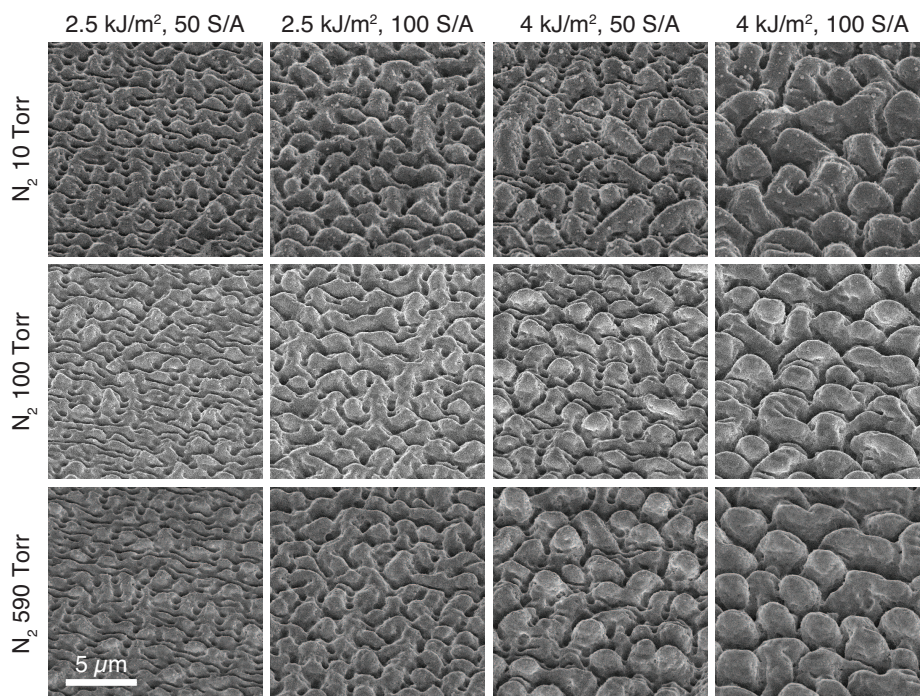


Figure 2.8: 45-degree SEM images of silicon surfaces shown in Figure 2.7

found only with the combination of high SF₆ pressure and low fluence or low S/A , the spikes become smaller. We hypothesize that under these fabrication conditions, the etching reaction due to the fluorine radicals is more significant than the result of laser texturing.

Figure 2.9 shows the light absorption of samples shown in Figures 2.5 and 2.6. The representative absorptance curves are shown in Figure 2.10. For light with energy both above and below the silicon bandgap energy, the absorptance is proportional to the size of the spikes. If the fluence is low (2.5 kJ/m²), the sub-bandgap absorptance increases with SF₆ pressure up to 100 Torr, and then drops significantly at 500 Torr. The sub-bandgap absorptance drop between 100 and 500 Torr is larger than the above-bandgap absorptance drop, so we think hyperdoping is not effective when the etching reaction dominates in the sample fabrication process.

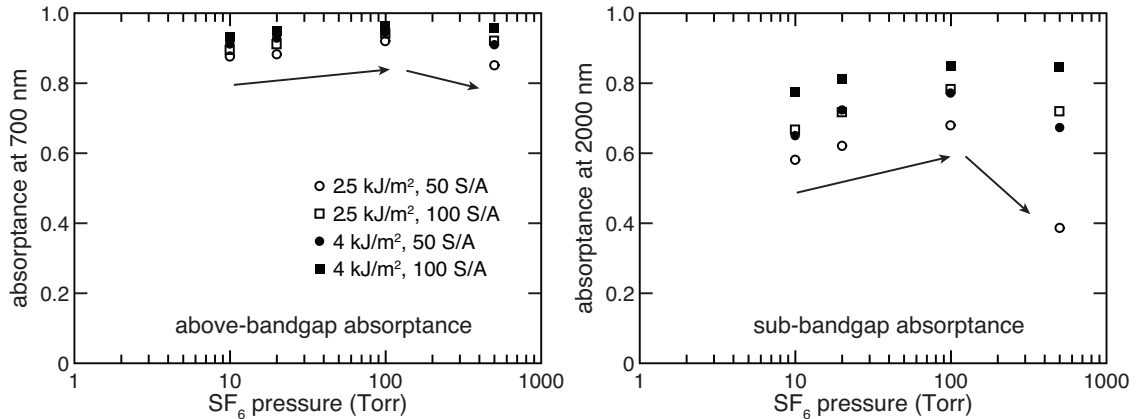


Figure 2.9: representative above (left) and below (right) bandgap light absorptance of samples fabricated under different conditions. We use light absorptance at 700 nm and at 2000 nm to represent above and below bandgap absorptance. For comparison, at 700 nm the absorptance of a silicon wafer (Si) is 0.67 and of a control sample (N₂) is 0.79. At 2000 nm the absorptance of Si is 0.07 and a N₂-sample is 0.23.

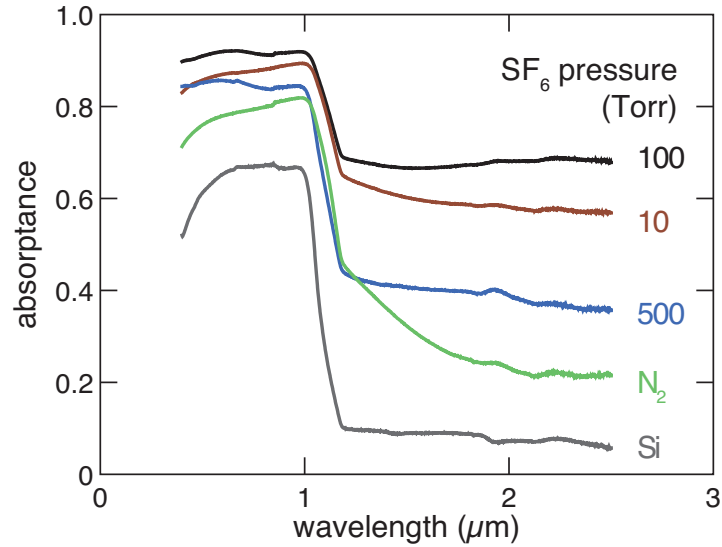


Figure 2.10: Absorbance curve of samples fabricated at 2.5 kJ/m^2 , 50 S/A and different pressures of SF_6 gas. Absorbance data of a flat single side polished silicon wafer (Si) and a control sample (laser irradiated at 10 Torr N_2) are plotted for comparison.

In this thesis, we use SF_6 pressure to control the sulfur concentration. We use pressure below 100 Torr to ensure the surface morphology of the samples does not vary significantly. When fabricating samples at 500 Torr, we use higher laser fluences (4 kJ/m^2 and 8 kJ/m^2).

Chapter 3

The dopant incorporation mechanism

This chapter studies the fundamental processes during femtosecond-laser hyperdoping of silicon with a gas-phase dopant precursor. We use secondary ion mass spectrometry to probe how the dopant concentration profile depends on the number of laser pulses and the pressure of the dopant precursor gas (SF_6). Through the pressure dependence on dopant incorporation, we find that the surface adsorbed molecules are the dominant source of the dopant atoms. Furthermore, we show the material quality is improved and the hyperdoped layer is single crystalline. The results show that the dopant incorporation depth, concentration, and crystallinity are respectively controlled by the number of laser pulses, pressure of the dopant precursor, and laser fluence. These parameters are important for building a comprehensive model to describe fs-laser hyperdoping with a gas-phase dopant precursor.

3.1 Introduction

Using pulsed lasers to introduce non-equilibrium concentrations of dopants into silicon (Si), also called hyperdoping, is a promising platform for fabricating Si with unique properties. For example, Si becomes a superconductor when hyperdoped with boron to greater than 5 at.% [85]. When heavy chalcogens (S, Se or Te) are used as dopants, the hyperdoped Si exhibits broad-band infrared absorption as well as photocurrent response at photon energies deep below the bandgap energy of Si [14,48,86]. Moreover, when using ultrafast lasers to perform hyperdoping, self-organized light-trapping structures often form as a result of laser induced periodic surface structures (LIPSS) [1,70]. Hyperdoping using femtosecond laser systems, however, often results in poor material crystallinity and currently lacks a reliable method for controlling the concentration profile [38]. Methods to improve material quality and to control the concentration profile will allow fs-laser hyperdoping techniques to be used for fabricating unique semiconductor devices.

The key processes during hyperdoping are laser-induced melting and resolidification (Figure 3.1). After fs-laser irradiation, the dopant atoms diffuse in from the surface while Si is molten. If the dopant concentration in the liquid is higher than the maximum solubility in the solid, as the Si resolidifies, the dynamics of the solid-liquid interface determines the fraction of dopant incorporated into the solid phase. The solute trapping kinetics depends on the resolidification velocity and the diffusive velocity of the dopant [11,12]. If the solid-liquid interface velocity is slow compared to the speed of diffusion (diffusive velocity), excessive solute (dopant) is rejected into the melt from the solid during the resolidification process. On the other hand, if

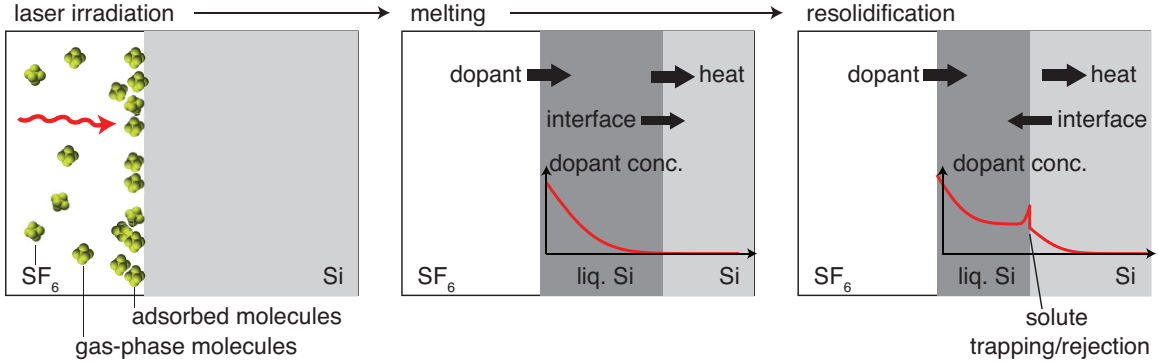


Figure 3.1: Schematics of the dopant diffusion process during pulsed-laser melting and resolidification. For clarity, SF_6 molecules in the vacuum chamber or adsorbed on the Si surface is only illustrated in the left panel. The arrows show the influx of dopant, heat diffusion and solid-liquid interface movement direction. The red curves in the middle and right panels are illustrations of the dopant diffusion profile and effect of solute trapping/rejection, which is a function of the interface velocity.

the interface velocity is fast, solute trapping occurs, achieving dopant concentration higher than what is thermodynamically favorable [12, 30]. Therefore, the source of the dopant atoms, diffusivity of the dopant in liquid Si, and the interface velocity play important roles in dopant incorporation.

Models that predict the dopant concentration profiles using ns-laser doping have been demonstrated with a technique called gas immersion laser doping (GILD) [87]. For boron or phosphorus doped Si using GILD, a strongly adsorbed layer of molecules, such as BF_3 , BCl_3 , B_2H_6 , and PCl_3 , is used as the dopant precursor [88, 89]. On the other hand, for a dopant with low solubility such as S, a model that predicts the dopant profiles also has been demonstrated using ion implantation followed by ns-laser melting [6, 90]. In this case, the dopants are introduced via ion implantation, instead of diffusion from the surface. For laser doping of S in Si, sulfur hexafluoride (SF_6), a stable, inert and commonly used industrial gas is an ideal dopant precursor.

The equilibrium S concentration in Si is low (maximum $3 \times 10^{16} \text{ cm}^{-3}$) [39], so solute trapping is necessary to introduce S with concentration approaching 1 at.% ($5 \times 10^{20} \text{ cm}^{-3}$), the concentration at which interesting optoelectronic properties are reported [48]. This study is aimed at studying S hyperdoping of Si us using fs-laser pulses with a gas-phase dopant precursor.

In this chapter, we perform hyperdoping of S in Si using fs-laser pulses at a fluence of 2.5 kJ/m^2 . We find that at this laser fluence, the hyperdoped layer is crystalline. We study how the pressure of the dopant precursor and the number of laser pulses influence the dopant concentration profile. Through this study, we identified that the dominant source of the dopant material is adsorbed SF_6 molecules. This chapter provides insight of the dopant incorporation mechanism and fabrication guidelines for fs-laser hyperdoping of Si.

3.2 Experimental

We use an amplified Ti:sapphire fs-laser system (center wavelength of 800 nm, pulse duration 80 fs, and repetition rate of 100 Hz) and focus the laser spot to $460 \mu\text{m}$ diameter (FWHM of a Gaussian beam profile) for hyperdoping. For measuring the dopant concentration profiles accurately, the surface of the samples should be flat and free of laser-ablated particles. We first perform laser irradiation tests on Si to identify processing parameters that produce samples suitable for concentration measurements. We examine the surface of Si samples irradiated with 1 to 10 laser pulses at fluences between 2.0 and 4.0 kJ/m^2 . We use a profilometer, an atomic force microscope (AFM) and a scanning electron microscope (SEM) to examine the samples. We find

irradiating the sample at a laser fluence of 2.5 kJ/m^2 with 6 laser pulses, the surfaces of the samples are flat and free of ablated particles nor laser induced periodic surface structures (LIPSS) [91].

Optical microscope images indicate that samples irradiated at a fluence of 2.5 kJ/m^2 could be crystalline. To examine the microstructure of the hyperdoped Si, we perform Raman spectroscopy to detect the presence of amorphous Si phases by monitoring the Raman shift at 150 cm^{-1} and 480 cm^{-1} . We use a Raman spectrometer with a 10-mW, 632.8-nm HeNe laser, recorded through a $20\times$ objective with a spot size of approximately $10 \mu\text{m}$. To support our Raman measurements, we also investigate the microstructure of one sample with transmission electron microscopy (TEM). A cross-sectional TEM sample is prepared using the lift-out method on a FEI Helios 600 dual-beam focused ion beam (FIB). Bright-field TEM images are collected with a JEOL 2010F transmission electron microscope operated at 200 kV.

For hyperdoping, the samples are irradiated with N number of laser pulses at SF_6 pressure of P and a laser fluence of 2.5 kJ/m^2 . N varies from 1 to 6 laser pulses, and P varies from vacuum (10^{-6} Torr) to 500 Torr. Prior to the laser treatment, Si wafers (p-type, float zone grown, $3 \text{ k}\Omega\cdot\text{cm}$) are solvent cleaned and etched with alignment markers ($800\text{-}\mu\text{m}$ circular mesas with $1.5\text{-}\mu\text{m}$ step height) using standard photolithography and reactive ion etching recipes. We then place the sample in a vacuum chamber, using an x-y stage to align the sample to the laser beam and pumped the chamber down to 10^{-6} Torr. Then we fill the gas chamber with SF_6 to the desired pressure.

To characterize the dopant concentration as a function of depth, we perform

secondary ion mass spectrometry (SIMS) measurements. The SIMS measurements are carried out using a 6-keV Cs ion beam with a current of 4 nA. We use the aforementioned alignment marker to center the measurement at the center of the laser irradiated spot and perform SIMS measurements on a square region of $20 \times 30 \mu\text{m}^2$. We record counts of ^{29}Si , ^{32}S , ^{34}S , ^{19}F and ^{18}O , and the S and F counts are calibrated against known ion-implanted Si samples.

3.3 Results

We first study the microstructure of the samples after laser irradiation at a fluence of 2.5 kJ/m^2 . Figure 3.2a shows Raman spectra normalized to the strong crystalline Si signal at 520 cm^{-1} . The Raman spectra show that the center of the laser irradiated area is crystalline and surrounding the crystalline center is a ring of amorphous Si [92]. Figure 3.2b is an optical microscope image of the sample showing a ring of a-Si with visible color contrast (the laser beam diameter is larger than the width of Figure 3.2b). To investigate the center of the laser irradiated area in detail, Figure 3.2c shows a TEM image of the sample from the center of the laser irradiated spot. In Figure 3.2d, fast Fourier transform of a hyperdoped area from Figure 3.2c shows that the center of the sample is single crystalline. Furthermore, the surface of the sample remains flat; AFM measurements show the RMS of the surface roughness is 0.5 nm. At this fluence, laser induced periodic surface structures develop after irradiating with more than six laser pulses.

Next, to understand the relationship between S incorporation, SF_6 pressure, and the number of laser pulses used, we summarize the result of the SIMS measurement

in Figure 3.3a. We determine the total incorporated dose of S (number of S atoms per unit area) from the SIMS measurement. Figure 3.3a shows that there is a critical pressure, P_{crit} , between 1 and 10 Torr. At pressures lower than P_{crit} , the S dose is independent of pressure and the number of laser pulses. At SF_6 pressures higher than P_{crit} , the S dose increases with both pressure and number of laser pulses.

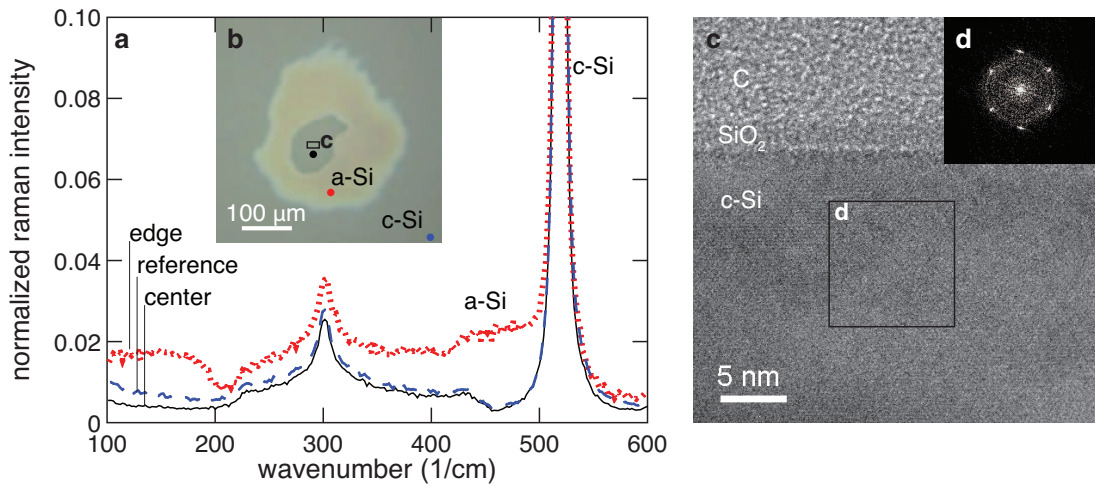


Figure 3.2: Microstructure of a hyperdoped sample. (a) Raman spectra taken from three different locations of the sample: the center (black solid line), edge of the laser irradiated spot (red dotted line), and a reference Si without laser irradiation (blue dashed line). The locations are marked in (b) the optical microscope image where the color contrast in shows the amorphous Si ring surrounding the center of the laser-irradiated spot. (c) Bright-field TEM image of a sample hyperdoped at 100 Torr with 4 laser pulses. The labels indicate protective carbon, C, native surface oxide SiO_2 , and the hyperdoped area, c-Si. The TEM sample is taken from the center of the laser-irradiated spot shown in (b). (d) Fast Fourier transform of the area indicated in (c) and shows the center of the laser-irradiated region is crystalline.

To study the dopant concentration profiles across the entire pressure range in detail, Figure 3.3b shows the pressure dependence for samples irradiated at 4 laser pulses. Below the P_{crit} , the dopant concentration profile is the same. Above P_{crit} , the concentration at the surface increases with pressure. For all samples irradiated

by the same number of laser pulses, in both the high fluence and low fluence regime, the dopants are incorporated to the same depth.

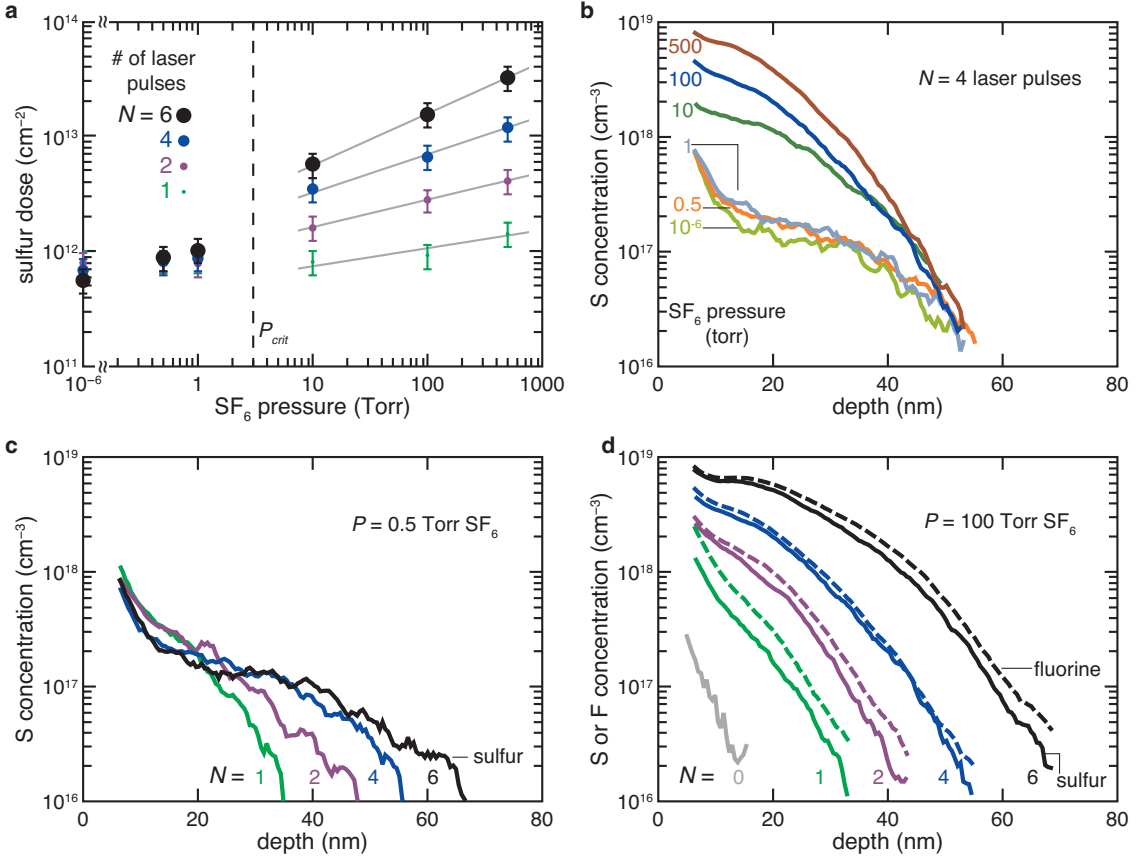


Figure 3.3: S dose and corresponding concentration profiles. (a) S dose, D , as a function of SF_6 pressure, P , and number of laser pulses, N . The lines represent the slopes, β , of data points between 1 and 500 Torr. $D \propto P^\beta$. $\beta = 0.16, 0.24, 0.33$, and 0.45 for $N = 1, 2, 4$, and 6 , respectively. All values of β are smaller than 1. (b) S concentration profiles of samples irradiated by four laser pulses at different pressures. (c) S concentration profiles of samples hyperdoped at 0.5 Torr. (d) S (solid line) and F (dashed line) concentration profiles of samples hyperdoped at 100 Torr. S conc. of a Si control sample (labeled $N = 0$) is also shown.

To study how subsequent laser pulses affect the S incorporation, we show the evolution of S concentration profiles after irradiating with different number of laser pulses in Figures 3.3c and 3.3d. In the low pressure regime (Figure 3.3c), the total

S dose (area under the concentration curve) is the same, but subsequent laser pulses allow the dopant to be incorporated deeper into the sample. In the high pressure regime, Figure 3.3d shows that both the surface concentration and the depth of the dopant distribution increases with the number of laser pulses. In all the profiles, the concentration of the incorporated S is higher than the maximum solubility of S in Si ($3 \times 10^{16} \text{ cm}^{-3}$).

Figure 3.3d also shows representative F concentration profiles. Due to the instrumentation, the F concentration uncertainty ($\pm 40\%$) is larger than the uncertainty of S concentration ($\pm 20\%$). We found that F incorporation is similar to S incorporation; F atoms are incorporated to the same depth and the profiles have the same shape. We find the F dose is about two times the S dose.

As a control sample, we perform SIMS measurement on Si samples without laser irradiation. The S concentration profile of the Si control sample is shown in Figure 3.3d ($N = 0$), and we find that there are no differences in the SIMS count whether or not the Si control sample is exposed to SF_6 gas. Therefore, the source of the S counts is most likely from native oxide. Ionized oxygen molecules have the same atomic mass as S and hence the signal contributes to the total count in the mass spectrometer [38]. The total S dose of the control sample is 10^{11} cm^{-2} , at least an order of magnitude smaller than the S dose in our sample, so the error from ionized oxygen molecules is a small percentage ($< 10\%$) of the S measured in the hyperdoped samples. Moreover, the control sample reveals the depth measurement uncertainty. With the energetic Cs ion milling, there is a mixing effect where portion of the atoms from the surface is push further into the sample [93]. As a result the

depth measurement uncertainty is about -10 nm.

Lastly, we study the effect of additional laser pulses on S concentration at different SF_6 pressures. Figure 3.4 shows the normalized S dose $D(N, P)/D(N = 1, P)$ as a function of laser pulses for all pressures. The SIMS experiment cannot provide

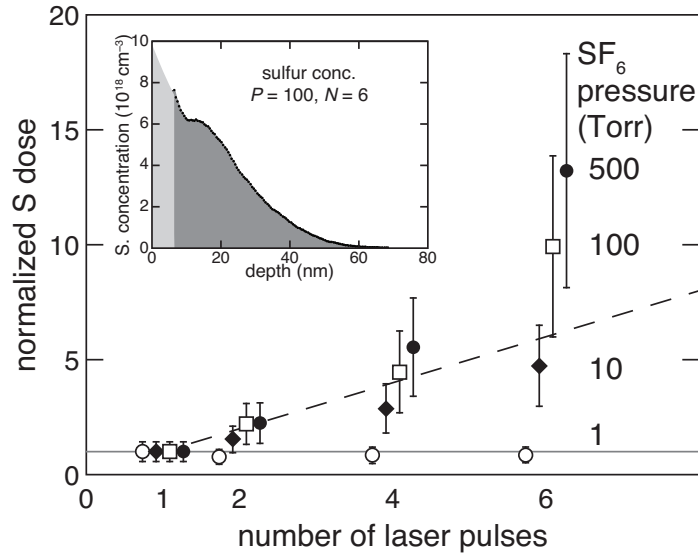


Figure 3.4: Normalized sulfur dose ($D(N, P)/D(N = 1, P)$) versus number of laser pulses at different SF_6 pressures: 1 (\circ), 10 (\blacklozenge), 100 (\square), and 500 Torr (\bullet). The data is displaced horizontally for clarity. Normalized dose at pressure lower than 1 Torr is the same at 1 Torr, so for clarity the low pressure data are not shown. The solid line indicates normalized dose equals to 1. The dashed line indicates a linear trend between S dose and number of laser pulses. The inset shows the possible surface concentration (light gray) that is not accounted by the SIMS measurement (dark gray).

accurate dopant concentration near the surface (within 5 nm), so for analyzing the evolution of dose as a function of laser pulses, it is necessary to estimate the surface concentration. We estimate the surface concentration with different scenarios: constant dopant concentration, a linear dependence, and an exponential dependence (Figure 3.4 inset). We include these estimations of the surface concentration into

the error bars. Figure 3.4 shows different trend for different pressure regimes: at the low pressure regime ($P \leq 1$ Torr), the total S dose is introduced in the first laser pulse. At higher pressures ($P \geq 100$ Torr), the dose increases super-linearly with the number of laser pulses.

3.4 Discussion

We first discuss the microstructure of the material and then discuss the S incorporation mechanism through examining the pressure and pulse number dependence of S incorporation. These results provide guidelines for controlling the dopant concentration and crystallinity using femtosecond laser hyperdoping.

3.4.1 Crystalline phase

The laser fluence used in this chapter is carefully chosen to optimize the material crystallinity and minimize surface texturing. Unlike our previous report, where the fluence used was higher than the ablation threshold and resulting material was amorphous [38], we now observe a crystalline phase (Figure 3.2). Bonse *et al.* report that there is a small fluence range between the melting and ablation threshold where the laser treated material remains crystalline [41]. Using both cross-sectional TEM and Raman spectroscopy, we identified that at a laser fluence of 2.5 kJ/m^2 , the center of the laser spot is crystalline. We demonstrate that we are able to control the resulting material crystallinity by carefully selecting the laser fluence and as a result the material quality is improved.

The microstructure of the hyperdoped layer depends on the resolidification dy-

namics, so from the crystallinity of our sample, we can identify the upper bound of the resolidification velocity. For Si, a crystalline phase cannot form if the solid-liquid interface moves faster than 15 m/s [37]. Since the hyperdoping area yields a crystalline material (Figure 3.2a), the solid-liquid interface velocity is less than 15 m/s during the entire resolidification process. On the other hand, the edge of the laser-treated spot is amorphous. This is because the laser beam has a Gaussian profile, the local fluence varies, and the resolidification velocities are different within the laser spot.

Laser scanning is commonly used for fabricating large-area samples. Although we identified a fluence range where hyperdoped Si is crystalline, Gimple *et al.* show that the amorphous phase is enhanced when scanning the laser pulses [84]. Thus the presence of amorphous Si prevents hyperdoping over a large area while maintaining the crystalline phase using a Gaussian beam [38](See also Chapter 2). For large area fabrication, using a flat-top beam to minimize the amorphous region can be promising. Our finding provides insight for fabricating hyperdoped Si with better crystallinity and hence better material quality.

3.4.2 Source of dopant atoms

We investigate how S is incorporated into Si from the ambient environment. There are two sources of the dopant precursors: molecules adsorbed on the Si surface prior to laser irradiation or gas-phase molecules impinging on the Si surface while Si is molten (Figure 3.1) [94]. The number of gas-phase molecules impinging on the Si surface is linearly proportional to the pressure, while the thickness of the adsorbed molecules depends on the adsorption isotherm and can be a non-linear function of

pressure. Thus, thorough examining how the dopant incorporation depends on pressure, we can determine which form of the dopant precursors is the dominant source. Figure 3.3a shows the dopant incorporation in two pressure regimes; dopant incorporation only exhibits pressure dependence above a critical pressure. Furthermore, at higher pressure, the pressure dependence is less than linear (fit lines with slope $\beta < 1$). Since we do not observe a linearly dependence on pressure, this suggest that, in either pressure regime, the impingement rate of gas-phase molecules is not the major source of dopant atoms. Thus the surface adsorbed SF_6 molecules are the dominant source.

This phenomenon where the incorporated dose depends on pressure only above a critical pressure threshold has been reported in ns-laser doping of phosphorous in Si using PF_5 or PCl_3 as dopant precursors [95,96]. Both papers suggest the adsorbed layer is the dominant source of the dopant, and the adsorbed layer thickness gives rise to the non-linear pressure dependence of dose. At low pressure, the dopant atoms are supplied by a layer of chemisorbed molecules where the adsorbed thickness is independent of pressure, and at higher pressure additional physisorbed molecules increases the thickness of the adsorbed layer. While the exact adsorption isotherm of SF_6 on Si is not known, this further supports that the adsorbed molecules are the dominant source.

In this study, we show that there is also significant amount of F incorporation. Previous studies on hyperdoping Si using SF_6 as dopant precursors did not focus on F incorporation. SF_6 molecules are inert and stable, but can etch Si when the molecules are excited or ionized [97,98]. The product of the etching reaction is Si tetrafluoride

(SiF₄) which is a volatile gas product. SF₆ molecules do not absorb 800-nm radiation but are thermally decomposed at the gas-solid interface after laser irradiation.¹ We hypothesize that after decomposition, some of the F atoms react with Si and some are incorporated into Si. As a result, we observe that both S and F are incorporated, and we obtain F concentration about twice as much as S. The structural and electronic properties of F dopant in Si is not well known, some reports suggest F atoms form small SiF₄ clusters inside crystalline Si [100,101]. While the etching reaction greatly impacts the F concentration, we cannot detect any morphological changes; the etch depth is small and introduces negligible surface roughness.

3.4.3 Pulse number dependence and concentration profiles

We study the total S dose incorporation and find the amount of dopant incorporated is only a small fraction of the molecules in the ambient environment. Comparing the S dose in Figure 3.3a to a density of monolayer surface coverage (10^{15} atoms per cm²), we find that the S dose incorporated into Si (10^{12} cm⁻²) for $N = 1$ is far less than the equivalent of a monolayer coverage of SF₆ molecules in Si. In this section, we first estimate the time scale for SF₆ molecules to build up on a clean Si's surface, and then discuss that only a small fraction of the total SF₆ molecules near the surface of Si is incorporated in the hyperdoping process.

We estimate how fast SF₆ molecules build up on the Si's surface and show that equilibrium adsorption is achieved at all pressures prior to laser irradiation with the

¹It has been reported that SF₆ molecules dissociates under intense laser irradiation at 800 nm, but this phenomenon is only observed at intensities higher than 4×10^{14} W/cm², more than two orders of magnitude higher than the process used in this experiment (2.5×10^{12} W/cm²) [99].

Table 3.1: Impingement rate of SF_6 molecules at different pressures. The impingement rate is: $J_{imp} = N_A P / \sqrt{2\pi MRT}$, where N_A is Avogadro's number, P is the pressure, $M = 146$ is the molecular weight of SF_6 , R is the universal gas constant, and T is temperature. Based on the impingement rate and estimating the surface density of 10^{15} cm^{-2} , we calculate the minimum time it takes to build up monolayer coverage by assuming the sticking coefficient is equal to 1.

Pressure (Torr)	Imp. Rate ($\text{cm}^{-2}\text{s}^{-1}$)	Time to build up a monolayer
10^{-6}	2×10^{14}	5 s
0.5	1×10^{20}	10 μs
1	2×10^{20}	5 μs
10	2×10^{21}	0.5 μs
100	2×10^{22}	50 ns
500	1×10^{23}	10 ns

first pulse. In Table 3.1, we calculate the impingement rate of SF_6 on a surface from the ideal gas law [102]. We find the minimum time that is required to achieve monolayer coverage by assuming the sticking coefficient is unity (all the molecules impinging on the surface stays on the surface). In the case of vacuum, we estimate that the minimum time required for building up a monolayer on the Si surface is only 5 s, much shorter than the time scale required for setting up the experiment. The impingement rate scales linearly with pressure, so at higher pressures the time it takes to achieve equilibrium adsorbed layer is much shorter than 5 s. From this analysis, the amount of SF_6 molecules adsorbed on the surface of Si is at equilibrium before the hyperdoping process, and this suggests that either the amount of SF_6 molecules adsorbed is small or only a small fraction of the dopant is incorporated during the hyperdoping process.

Our investigation into the effect of additional laser pulses on S concentration

shows unexpected observation at both low and high pressure. At pressures below 1 Torr, Figure 3.4 shows that the total S dose is introduced in the first laser pulse, and subsequent laser pulses introduce zero influx of dopant material. The repetition rate of the laser is 100 Hz, so the time separation between laser pulses is 10 ms. Table 3.1 suggests that at 0.5 and 1 Torr, the surface adsorption reaches steady state on the order of 10s of microseconds. So before the subsequent laser pulses arrives at the sample surface, we expect more SF₆ molecules adsorbed at the surface. Thus it is interesting that at 0.5 and 1 Torr the additional laser pulses do not introduce more S dopants. It is possible the actual time to achieve steady state is much longer than estimated in Table 3.1 if the sticking coefficient is much less than one or the desorption rate is high.

At pressures equal to 100 and 500 Torr, the S dose increase more than linearly compared to the number of the laser pulses used (Figure 3.4). For the S dose to increase more than linearly, the dopant flux needs to increase with successive laser pulses. One possible reason is that with more laser pulses, the native oxide on the surface can diffuse into Si or be removed [1, 103]. The flux then increases because S atoms can diffuse into Si more easily without the surface oxide [96]. As a preliminary result, we observe super-linear trend at high pressure as the number of laser pulses increases. Studying effects on surface treatments, such as removing the native oxide prior to hyperdoping, will provide more information.

Lastly, we outline where additional information on the laser melting and resolidification dynamics is needed to elucidate the hyperdoping process. First, in Figure 3.3 we observe that the dopant incorporation depth increases with the number of laser

pulses. The depth increase is a result of either increasing the melt depth or increasing the diffusion length. Information on the melt depth and melt duration will allow us to calculate diffusion length and compare the two length scales. Second, the resolidification velocity is necessary to describe the solute trapping kinetics. With the surface boundary condition we analyzed in Sec. 3.4.2, and if the details on melting and resolidification dynamics is available, we can calculate the dopant concentration profiles including the solute trapping and rejection. Here we hope to provide insights for building a predictive model of doping material with low solubility from a gas-phase dopant precursor [104].

To summarize this section, we observe the S dose is independent of number of laser pulses at pressures at or lower than 1 Torr and is super-linear at 100 and 500 Torr. We also observe the depth of the dopant incorporation increases with additional laser pulses. Information on surface treatments, melt duration and resolidification dynamics are needed to explain the observed dose and concentration profiles.

3.5 Conclusion

In conclusion, we perform fs-laser hyperdoping under different dopant precursor pressures with different number of laser pulses. We have identified that at a fluence of 2.5 kJ/m², we can form single crystalline hyperdoped Si using fs-laser irradiation. We study the dopant concentration profile and dose using SIMS, and we find there are two pressure regimes. At pressures below 1 Torr the dose of S incorporation is independent of pressure and number of laser pulses; at pressures higher than 10 Torr, the S dose increases with both pressure and number of laser pulses. Analyzing the pressure

dependence of dopant incorporation reveals that the surface adsorbed molecules are the dominant source of the dopant material. Analyzing the effect of multiple-pulse irradiation shows that the dopant incorporation depth depends on the number of laser pulses. This chapter provides insight of the dopant incorporation mechanism, fabrication guidelines for hyperdoping Si with high crystalline quality, and information for building a predictive model to engineer desired dopant concentration profiles.

Chapter 4

Intermediate band conduction in fs-laser hyperdoped silicon

We use fs-laser hyperdoping to introduce non-equilibrium concentrations of sulfur into silicon. With increasing dopant concentration, the sub-bandgap absorption increases. We anneal the samples at 975 K for 30 minutes and then perform Hall and resistivity measurements at temperatures between 14 and 300 K. The carrier concentration and resistivity as a function of temperature suggests that the dopant concentration is below the insulator-to-metal transition and the samples have a localized intermediate band. Using a two-band model, we analyze the dopant concentration and the location of the intermediate band.

4.1 Introduction

In recent years, advances in doping techniques have enabled various methods of introducing non-equilibrium concentrations of dopants into host materials. Beyond traditional choices of dopants, hyperdoping silicon with deep level dopants can introduce interesting optical [4, 105], electronic [61], and optoelectronic properties [48, 86]. These unusual properties are a result of the high dopant concentration, which can broaden the dopant energy level into a band, often called the impurity band or the intermediate band. In the context of this work, impurity band and the intermediate band have the same meaning, and we use these two terms interchangeably to be consistent with the literature we reference. In this work, we report the electronic transport properties of silicon supersaturated with deep level dopants and present methods to identify the location of the intermediate band.

We first review literature on the impurity band [106]. Impurity bands from shallow dopants have been reported in many host materials, including Ge, Si, and GaAs [107–110]. When a dopant, for example a phosphorus atom, is introduced into silicon, the dopant electron is bound and localized to the dopant ion. The energy required to excite the electron to the conduction band where the electron is delocalized is the dopant energy level. By measuring the number of carriers as a function of temperature, one can probe the dopant energy level. When the dopant concentration increases, the average separation between the dopant atoms decreases, and the interaction between dopant electrons increases. At a critical concentration, the electron-electron interaction leads to a delocalized dopant energy band instead of a single dopant energy level. In many systems, the critical concentration, n_{crit} , is

approximately $a_b \cdot n_{crit}^{1/3} = 0.2$, where a_b is the effective Bohr radius of the dopant electron [111,112]. Above n_{crit} , a condition referred to as the insulator-to-metal transition, the energy required to promote an electron to a delocalized state vanishes. The temperature dependence of carrier concentration also vanishes, and at temperatures approaching 0 K, the electrical conductivity remains non-zero. The signature for when the insulator-to-metal transition occurs thus is seen in the form of a finite conductivity when $T \rightarrow 0$.

At dopant concentrations just below the insulator-to-metal transition, the samples can exhibit low temperature conductivity. The electron wave functions are localized, but the carrier concentration as a function of temperature is not described by the freeze out of the electrons from a single dopant energy level. Thus, below the insulator-to-metal transition, there is another critical concentration at which the low temperature conductivity exhibits band-like behavior, and electrons conduct through hopping [113]. It requires considering two bands, the conduction band and the impurity band, to describe the observed temperature dependence in the electronic transport data [107,112,114]. Even though most of the literature still uses impurity “band” to refer to systems below the insulator-to-metal transition, it is important to point out that electronic states in the “band” are strictly localized [106].

Studying properties of deep level intermediate bands is a significant challenge because for deep level dopants, the maximum solid solubility is low. Reliable hyperdoping techniques are essential for studying deep level dopants at higher concentrations. Furthermore, since hydrogen-like models do not describe deep level dopants well [115], the effective Bohr radius is not a good measure to estimate the criti-

cal concentration for band formation. Examples of these deep level dopants include heavy chalcogens (S, Se and Te). Sulfur dopants, for instance, have energy levels at 188 or 318 meV below the conduction band edge, depending on their atomic configuration [47]. Many studies use ion-implantation to introduce high concentrations of chalcogen dopants into silicon and report low temperature conductivity, but it is hard to rule out peculiar effects due to ion-implantation damage [116–118]. In 2011, Winkler *et al.* used ion-implantation followed by nanosecond-pulsed laser melting to heal the crystal lattice and identified insulator-to-metal transition for S-hyperdoped silicon at a critical concentration between 1.8 and $4.3 \times 10^{20} \text{ cm}^{-3}$ [61].

In this chapter, we use fs-laser hyperdoping to introduce non-equilibrium concentrations of sulfur into silicon and find that the samples exhibit temperature dependence consistent with systems below the insulator-to-metal transition. We present methods to study the low temperature electronic transport data and identify the location of the intermediate band. We identify a localized “band” formation below the insulator-to-metal transition. These findings are important for evaluating S-hyperdoped silicon for potential applications and provide analysis techniques to study other deep level dopants [119].

4.2 Experimental

Silicon wafers ((100) orientation, float zone grown, p-type, $10 \text{ } \Omega\cdot\text{cm}$) are cleaned to remove organic and metallic contaminants [120]. The wafer is placed in a chamber and irradiated at normal incidence with Ti:sapphire laser pulses with 80-fs pulse duration (center wavelength at 800 nm and 1-kHz repetition rate). The chamber is filled with

sulfur hexafluoride (SF_6) gas at a pressure between 1 and 100 Torr. The laser pulses have an average energy of 1.0 mJ and are focused to a spot size of 600 μm (FWHM of a Gaussian intensity profile), yielding a fluence of 2.5 kJ/m^2 . A set of scanning mirrors scans the laser beam across a $25 \times 25 \text{ mm}^2$ area and translates subsequent pulses by 75 μm such that any given spot in the irradiated region is exposed to 50 laser pulses. After laser irradiation, samples are annealed for 30 minutes in an open-tube furnace with a flow (280 sccm) of forming gas (95% He, 5% H_2) at 975 K.

After sample fabrication, we study the light absorption properties, surface morphologies and dopant concentrations. Using a spectrophotometer, we collect transmission (T) and reflection (R) spectra and calculate absorptance ($A = 1 - R - T$). The spectrophotometer is equipped with an integrating sphere in order to collect transmitted and reflected light at all angles. We perform secondary ion mass spectrometry (SIMS) measurements to verify the sulfur concentrations in these samples.

For measuring electronic properties of these samples, we cut samples into 6-mm squares and deposit 1.2-mm square Ti-Ni-Ag (20–20–200 nm, Ti adjacent to Si) contacts at four corners of the samples. We also deposit Al contacts at the back of the samples for measuring the current-voltage properties of the junction between the laser-doped region and the substrate. The samples studied in this work for transport measurements all have Ohmic contacts and rectifying diode behavior. We use the van der Pauw technique [121,122] for temperature-dependent resistivity and Hall measurements using a constant excitation power between 25 to 100 nW to avoid self-heating effects while minimizing measurement errors. Measurement temperatures between 10 and 300 K are controlled by a closed-cycle helium cryostat. Hall measurement is

performed at a magnetic field $B = 0.6$ T.

Sheet carrier concentration n_s is calculated from the measured Hall voltage V_H using $n_s = r_H \frac{IB}{qV_H}$, where r_H is the Hall scattering factor, I is the excitation current and q is the elementary charge (see also Appendix A). We assume the Hall scattering factor is equal to 1 [61]. If the hyperdoped layer thickness, d , is well defined, the carrier concentration is $n_H = n_s/d$. In this work, we focus our analysis on normalizing $n_s(T)$ to $n_s(T = 300)$ at room temperature. The advantage of studying normalized n_s , instead of n_s itself, is that we do not need to assume a certain thickness of d , and we can still analyze the temperature dependent behavior (Section 4.4). In addition, as long as the Hall scattering factor r_H depends weakly on temperature, we do not need to know how much r_H deviates from 1. After obtaining sheet resistivity ρ_s and sheet carrier concentration n_s , we calculate the Hall mobility μ_H , using $\mu_H = (q \rho_s n_s)^{-1}$.

4.3 Results

Figure 4.1 shows the sulfur concentration and the sub-bandgap absorption of samples hyperdoped at different SF_6 pressures. The SIMS measurements indicate that the S concentration near the surface increases with pressure from 2.0×10^{18} to 1.3×10^{19} cm^{-3} . With increasing SF_6 pressure, the sub-bandgap absorption increases as well. Annealing improves the crystallinity and the material becomes polycrystalline [2]. After annealing at 975 K, we find no difference in the S concentration from the SIMS measurements. After annealing, however, the sub-bandgap light absorption is reduced and no longer a function of the SF_6 pressure. Absorption spectra and SEM images are shown in Figure 4.2. The surfaces of the samples are rough after laser

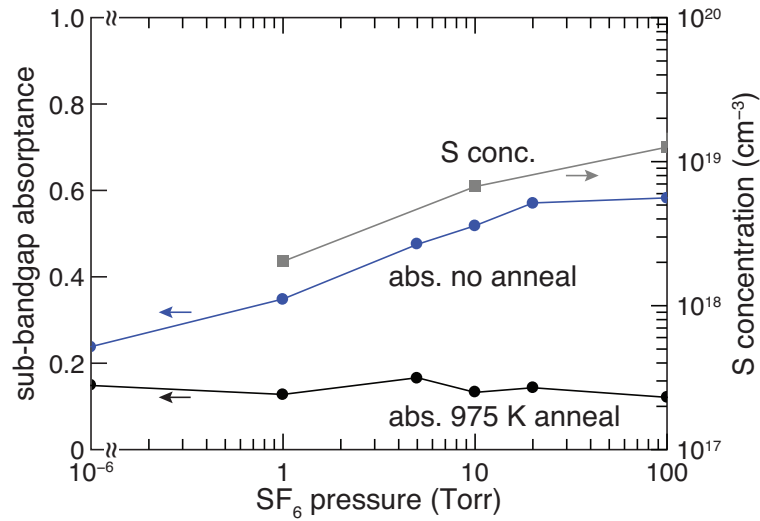


Figure 4.1: Average sub-bandgap absorbance (●) and sulfur concentration (■) of samples hyperdoped at different pressures of SF₆. For average sub-bandgap absorbance, we average the absorbance at wavelengths between 1250 and 2500 nm. We show absorbance both before (blue) and after annealing (black). The S concentration is measured after annealing.

doping, but the surface morphologies are very similar between samples fabricated at different pressures. The residual sub-bandgap light absorption of 0.2 could be due to a measurement error from light scattering out of the detector (see also Appendix B).

To study the electronic properties, we focus only on the samples annealed at 975 K. We find that only the samples annealed at 975 K or higher temperatures exhibit diode formation between the hyperdoped region and the substrate. A rectifying junction between the hyperdoped layer (n-type) and the substrate (p-type) isolates the measurement current to within the hyperdoped layer, and thus allowing us to probe only the properties of the hyperdoped layer. Therefore, we only perform Hall and resistivity measurements on samples annealed at 975 K.

Figure 4.3 shows sheet carrier concentrations, sheet resistivities, and Hall mobilities as functions of inverse temperature. Samples A, B, C, and D refer respectively

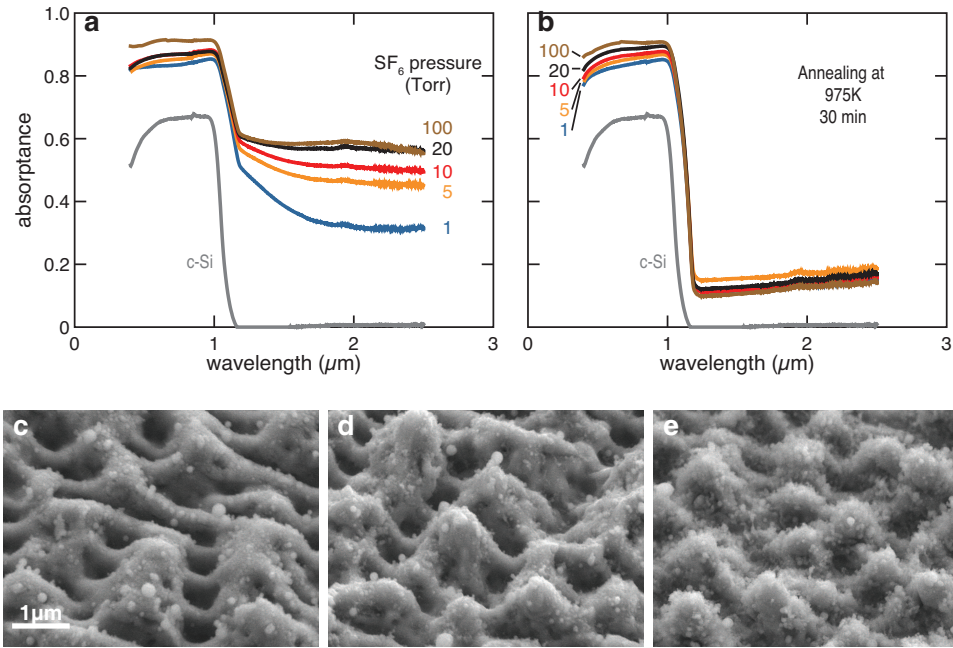


Figure 4.2: Absorbance of S-hyperdoped silicon (a) before and (b) after annealing. (c) – (e) 45° SEM images of samples hyperdoped at 1, 10, and 100 Torr, respectively.

to silicon hyperdoped at SF₆ pressures of 1, 10, 20, and 100 Torr followed by a 30-min annealing at 975 K. Figure 4.3a shows that the carrier densities exhibit little temperature dependence, and the Hall measurement data indicate n-type carriers for all four samples at all temperatures. In contrast, the Si substrate is p-type and the carriers freeze out quickly as the sample cools down. To further investigate the temperature-dependent carrier concentrations, Figure 4.3b shows normalized sheet carrier concentration. For Samples C and D, we observe more carriers at low temperatures than at room temperature. Figure 4.3c shows the sheet resistivity is in the range of 2.1 to 2.6 kΩ/□ at room temperature, and at the lowest temperature (14 K) resistivity increases by a factor of 5 to 7. The Hall mobility shown in Figure 4.3d is proportional to the inverse product of n_s and ρ_s . Since n_s is relatively independent of

temperature, the Hall mobility shows inverse trend of ρ_s . For example, for Sample C, the Hall mobility decreases from $55 \text{ cm}^2\text{V}^{-1}\text{s}^{-1}$ at room temperature to $7 \text{ cm}^2\text{V}^{-1}\text{s}^{-1}$ at low temperature.

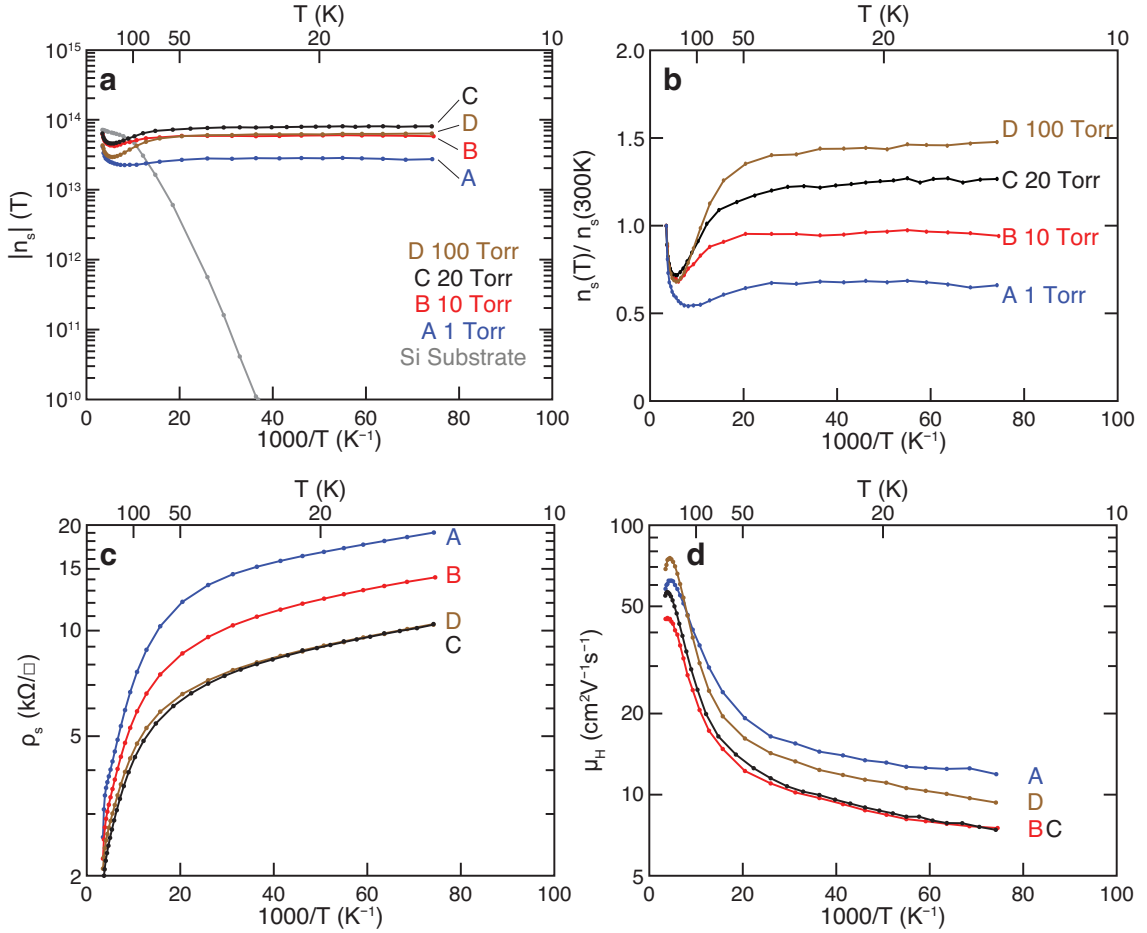


Figure 4.3: Temperature-dependent transport measurements: (a) sheet carrier concentration, (b) normalized carrier concentration with all values normalized to the sample's sheet carrier concentration at room temperature, (c) sheet resistivity, and (d) Hall mobility. Samples A through D are hyperdoped at SF₆ pressures of 1, 10, 20 and 100 Torr, respectively. Sheet carrier concentration data for the silicon substrate (p-type) are shown for comparison.

4.4 Discussion

In this discussion, we present methods to study the hyperdoped silicon samples through analyzing the small temperature dependence of the carrier concentration. Temperature-dependent characteristics are useful for identifying fundamental properties of dopants in the host material. For example, by fitting how carriers freeze out, one can find the dopant energy level. On the other hand, in a semiconductor, if a sample is doped with concentrations higher than the insulator-to-metal transition, the sample exhibits metallic-like conduction (conductivity that is independent of temperature) [109, 110]. We first introduce fundamental equations for describing carrier concentration as a function of temperature. Then we discuss using a two-band model to describe transport properties in hyperdoped silicon.

4.4.1 Carrier concentration at thermal equilibrium

In a non-degenerate regime, the number of carriers in the conduction band, n_c , is described by the Fermi level,¹

$$n_c = N_c \cdot e^{(E_f - E_c)/(kT)}, \quad (4.1)$$

where N_c is the effective density of states in the conduction band, E_f is the Fermi level, E_c is the energy of the conduction band minimum, and k is Boltzmann's constant. At the same time, if there are donors at density N_d and compensating acceptors at density N_a , and if we assume a negligible concentration of intrinsic carriers, the

¹In Section 4.4.3, we show that the analysis for a non-degenerate regime applies to our sample.

number of electrons in the conduction band is described by,

$$n_c = N_d - N_a - \frac{N_d}{1 + \frac{1}{2}e^{(E_d - E_f)/(kT)}}, \quad (4.2)$$

where the last term describes the number of donors that are not ionized, and E_d is the energy level of the donor. We focus the discussion on donors, and the same principle holds for acceptors. Substituting $e^{-E_f/(kT)}$ in Eq. 4.2 with $\frac{N_c}{n_c} e^{-E_c/(kT)}$ from Eq. 4.1, and defining $\Delta E = E_c - E_d$, the full solution for n_c is:

$$n_c = \frac{1}{2} \left(-(N_a + A) + \sqrt{(N_a - A)^2 + 4N_d A} \right), \quad (4.3)$$

where $A = \frac{N_c}{2} e^{-(\Delta E)/(kT)}$. We can thus obtain the number of carriers as a function of T , ΔE , and the donor and acceptor concentrations.

In Eq. 4.2, we assume each donor contribute one donor electron at energy level E_d . For dopant atoms that contribute more than one donor electrons, each at a different energy level, Eq. 4.2 applies only to temperature ranges where the Fermi level is close to the particular energy level E_d [123]. For example, sulfur dopants are double donors; in a dilute concentration, a single substitutional sulfur dopant has two energy levels at 0.3 and 0.6 eV below the conduction band edge [47]. In the low temperature regime, the deeper level is not ionized and does not contribute to conduction, and the situation is equivalent to one with a single donor. At higher temperature, one needs to consider the double donor nature of the sulfur dopants. Since our experiment study transport properties at low temperatures, we consider a single donor electron and apply Eq. 4.2.

For low doping concentrations and a moderate temperature regime such that

$N_a \ll A \ll N_d$, we have approximately [124],

$$n_c = \sqrt{N_d A} = \sqrt{\frac{N_d N_c}{2}} e^{-\Delta E / (2kT)}. \quad (4.4)$$

This equation describes how fast the electrons in the conduction band freeze out as the temperature decreases. The analysis for acceptors is the same. Using Eq. 4.4 to fit the slope of measured data at temperatures between 25 and 82 K for the Si substrate, we obtained the dopant energy level at 48 ± 3 meV. The measured boron dopant energy level matches well with the literature value (45 meV) [125]. Here we only describe the semiconductor physics necessary for finding a donor energy level in a moderate temperature range. Detailed descriptions of semiconductor behavior in different temperature regimes can be found in Ch. 4 of Ref. [124] and Ch. 3 of Ref. [3]. Detailed descriptions of semiconductor behavior in a degenerate regime can be found in Ch. 3 of Ref. [123]

4.4.2 Two-band conduction at high dopant concentration

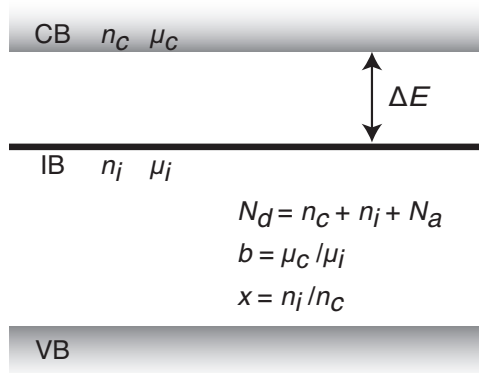


Figure 4.4: Two-band model schematics.

With the presence of an intermediate band (schematic shown in Figure 4.4), if the

electrons are mobile in the intermediate band, then the Hall measurement not only measures n_c , the carriers in the conduction band (CB), but it also probes n_i , the carriers in the intermediate band (IB). Since the carriers in CB and IB have different mobilities, μ_c and μ_i , the measurement is a weighted average of carriers in the two bands (see Appendix A for the derivation) [106]. First, the measured conductivity of the sample is the total conductivity of the two bands:

$$\sigma_H = \sigma_c + \sigma_i = e(n_c \mu_c + n_i \mu_i), \quad (4.5)$$

where we use subscripts c , i , and H to denote properties of the CB, the IB, and the transport measurements (Hall and resistivity), respectively. The weighted average of carriers in the two bands gives the following expression for the measured Hall carriers [107]:

$$\frac{1}{n_H} = \left(\frac{\sigma_c}{\sigma_H}\right)^2 \frac{1}{n_c} + \left(\frac{\sigma_i}{\sigma_H}\right)^2 \frac{1}{n_i}. \quad (4.6)$$

Finally, the measured Hall mobility is:

$$\mu_H = \frac{n_c}{n_H} \mu_c + \frac{n_i}{n_H} \mu_i. \quad (4.7)$$

Fermi statistics still hold, and Equations 4.1 to 4.3 are still valid. Moreover, the number of carriers in the intermediate band is equal to the non-ionized carriers described in Eq. 4.2,²

$$n_i = N_d - N_a - n_c = \frac{N_d}{1 + \frac{1}{2} e^{(E_d - E_f)/(kT)}}. \quad (4.8)$$

Although the Hall measurement now reports a weighted average of the carriers in the two bands, it is still possible to find the dopant energetics through temperature-dependent measurements. We use a two-band model, developed in the 1960s to

²The factor 1/2 in the denominator of Eq. 4.8 describes the density of states for a localized band. For a delocalized band, the factor is equal to 1 [110].

describe the Hall measurement data [110,114,126]. Let b be the ratio of the mobility of carriers in the CB to that in the IB, $b = \mu_c/\mu_i$. And let x be the ratio of the carrier density in the IB to that in the CB, $x = n_i/n_c$. We can rewrite n_H using Equations 4.5 to 4.7,

$$n_H = n_c \frac{(b+x)^2}{b^2+x}. \quad (4.9)$$

Emel'yanenko *et al.* point out that, compared to x , b depends much more weakly on temperature, so b can be approximated as a constant [114]. For example, if we take $N_d = 1.1 \times 10^{18} \text{ cm}^{-3}$, $\Delta E = 70 \text{ meV}$, and $N_a = 0$, we can calculate n_c using Eq. 4.3, n_i using the first part of Eq. 4.8, and obtain x . Figure 4.5 shows calculated Fermi level, n_i , n_c , and n_H as a function of inverse temperature. The relative position of the Fermi level and E_d indicates the distribution of carries in the IB and in the CB (Figure 4.5a). The Fermi level is independent of b and is below E_d

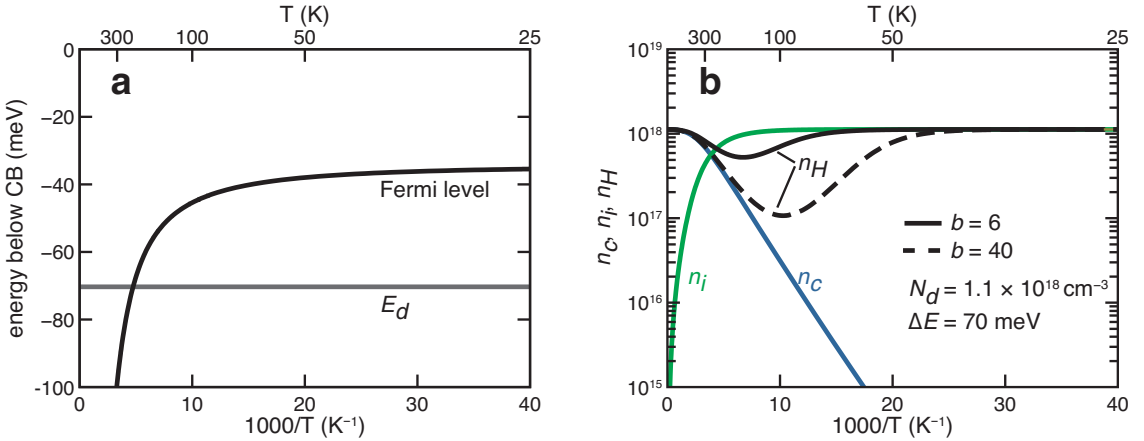


Figure 4.5: Calculated (a) carrier concentrations and (b) Fermi level as a function of inverse temperature with $N_d = 1.1 \times 10^{18} \text{ cm}^{-3}$, $\Delta E = 70 \text{ meV}$. Carrier concentration in the intermediate band n_i (green) and conduction band n_c (blue) depends on N_d and E_d . The measured Hall carrier concentration, n_H , depends on N_d , E_d , and the mobility ratio of the two bands. The black solid line shows n_H for $b = 6$ and the black dashed line shows n_H for $b = 40$.

for temperature above 210 K. At high temperatures, most carriers are ionized into the CB band, so $x \rightarrow 0$ and $n_H \rightarrow n_c$, and the measured carrier are just carriers in the CB. At low temperatures, all the carriers are in the IB, so $x \gg b$ and $n_H \rightarrow n_i$. In the intermediate temperature, n_H exhibits a minimum. For an IB that is isolated from the CB, Figure 4.5b shows the characteristic shape of the n_H curve as a function of inverse temperature: a minimum dip follow by a temperature-independent line at lower temperatures [113].

To gain better intuition of the model, curves of n_H with different values of N_d ,

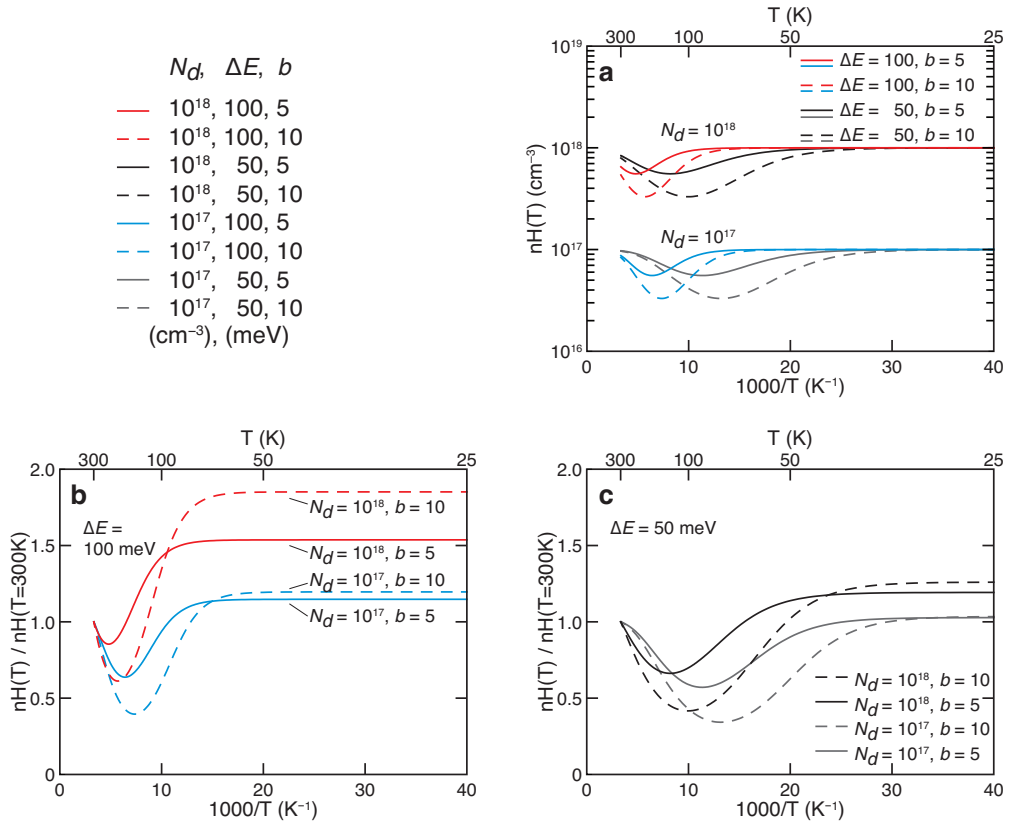


Figure 4.6: (a) Calculated temperature-dependent Hall carrier concentrations with different N_d , ΔE , and b . (c) and (d) Normalized carrier concentration curves. Figure legend is shown in the top left corner.

ΔE , and b are shown in Figure 4.6a. We see that the size and the location of the minimum in n_H depend on all variables. Figures 4.6b and 4.6c show normalized n_H ; Each curve is normalized to its n_H value at 300 K. Unlike shallow dopants [114, 127], only a fraction of deep level dopants are ionized into the CB at room temperature. Therefore, for all of the curves, n_H at low temperatures is higher than n_H at room temperature. The larger the donor concentration, the dopant energy level, or the mobility ratio, the higher n_H is at low temperatures compared to n_H at room temperature.

4.4.3 S-hyperdoped silicon

We performed a least-squares fit of the normalized n_s data shown in Figure 4.3b with three fitting parameters: N_d , ΔE , and b . By normalizing the data, $n_s(T)/n_s(300) = n_H(T)/n_H(300)$, so our analysis does not require knowing the exact sample thickness d . We found a weak dependence of the fitting quality on N_a , so N_a was excluded from the fitting routine ($N_a = 0$). Figure 4.7 shows the fitted curves compared to our measurements, and Table 4.1 shows the value of the fitting parameters. The fitting result suggests that ΔE is large and N_d is small, implying our system is in the non-degenerate regime, so we indeed can apply the approximation we use in Eq. 4.1 [123]. The fit quality is the best for Sample D, which has the highest dopant concentration. As the dopant concentration increases, the number of donors increases and the dopant energy level reduces. The large values of E_d we obtained from the model suggest that the intermediate band is isolated from the conduction band edge.

Comparing N_d to the SIMS concentration for Sample D, we find that N_d only

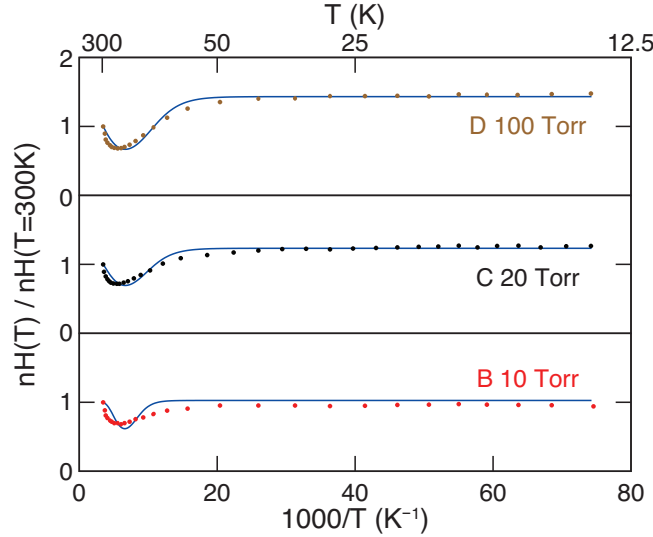


Figure 4.7: Normalized carrier concentrations of sample B (bottom), C (middle), D (top) and fitted curves. Measure data are shown in dots; blue solid lines are fitting results.

accounts for 10% of the sulfur dopants in the sample (Table 4.1). Another study reports similar finding where 90% of the sulfur dopants in hyperdoped Si are not detected by Hall measurements [3]. It is possible that the majority of the sulfur dopants occupy a much deeper energy level, the dopants are not electrically active, or the electrons are not mobile.

Table 4.1: Sulfur concentrations and two-band model fitting results for samples hyperdoped at different SF_6 pressures.

Sample	SF_6 pressure (Torr)	SIMS S concentration (10^{18} cm^{-3})	Two-band model		
			N_d (10^{18} cm^{-3})	ΔE (meV)	b
A	1	2.0 ± 0.3	–	–	–
B	10	6.7 ± 1.0	0.002	150 ± 60	4.4 ± 0.6
C	20	–	0.4 ± 0.2	80 ± 10	4.7 ± 0.5
D	100	13 ± 2	1.1 ± 0.6	70 ± 10	6.4 ± 0.5
D without annealing	100	16 ± 2	–	–	–

We point out two outstanding issues of this analysis. First, for a deep level dopant, the two-band model implies the number of carriers at low temperature is always higher than the number of carriers at room temperature (Figure 4.6b), so we cannot find a good fit for sample A, the sample with lowest dopant concentration. It is likely that in addition to the intermediate band, there are isolated energy levels where the carriers are not mobile and hence not measureable once the electrons occupy the level [106]. Second, the two-band model assumes the band width of the intermediate band is relatively small compared to ΔE [114]. Density functional theory (DFT) calculations suggest that the band-width of the sulfur intermediate band could be large [64, 128]. Ignoring the bandwidth in the IB could influence the quality and the result of the fit.

4.4.4 Intermediate band below the insulator-to-metal transition

Figure 4.3c shows that the resistivity increases as temperature decreases, indicating the absence of metallic-like conduction. Instead, we observe hopping conduction at low temperature. The temperature-dependent resistivity suggests the carrier concentration in our sample is below the insulator-to-metal transition, and the electron wave functions in the intermediate band are localized. Fitting the conductivity data below 25 K to an Arrhenius equation, we obtain an activation energy of 0.53 ± 0.04 meV. The presence of hopping conduction further supports that our system is below the critical concentration for delocalized band formation.

When electronic wave functions in the “band” are localized, compensating ac-

ceptors (N_A) are essential for low-temperature conductivity [112]. When there are compensating centers, electrons occupy the compensating states and leave behind empty states in the IB. The presence of empty states enables carriers to conduct by hopping from occupied states to empty states. There is an activation energy associated with carrier hopping, so the conductivity decreases as temperature decreases.³

While we have clear evidence of hopping conduction, we cannot determine the origin of the compensating acceptors. In this experiment, the substrate is p-type and has acceptor concentration at $1.1 \times 10^{15} \text{ cm}^{-3}$. Furthermore, compensating acceptors, among other types of defects, could be created during the hyperdoping [2] and annealing process [118]. To address this, future experiments with different levels of acceptor concentration in the substrate are essential to elucidate the origin of the compensating acceptors.

4.4.5 Electronic properties decoupled with optical properties

We hypothesize that annealing is necessary for diode formation due to the presence of laser-induced defects. After fs-laser hyperdoping, we observe that without annealing there is no diode isolation between the hyperdoped layer and the substrate underneath. For samples annealed at temperatures below 975 K, majority of the measurement current flows through the substrate and hence the measurement merely reflects the properties of the substrate. It is possible that the presence of amorphous silicon and other defects reduces the shunt resistance significantly, and the current is shorted through the substrate. Our earlier study shows that after fs-laser hyper-

³In the two-band model, the mobility is set to be a constant independent of temperature, so the model does not take into account how the compensating acceptor affects conductivity.

doping, the sulfur dopants are electrically active immediately following the doping process [38]. Thus, instead of activating the dopants, the purpose of annealing is to remove lattice defects.

Annealing also reduces sub-bandgap absorption, and the central question is whether annealing significantly modifies the band structure, specifically the IB nature of the hyperdoped silicon. After annealing, the samples have no strong sub-bandgap absorption, but the concentration of sulfur dopant is sufficient to form an localized IB below the insulator-to-metal transition. The implication of our observation is that the formation of a localized IB is not necessarily coupled with sub-bandgap absorption. As we are interested in the states that contribute to sub-bandgap absorption, future directions include reducing the laser irradiation damage without furnace annealing, or developing methods to isolate the hyperdoped layer from the substrate. Studying the electronic properties before annealing is important to understand how annealing affects the band structure and whether the deactivation of sub-bandgap absorption is due to a reduction of the dopant concentration by dopant diffusion or to the dopant changing its chemical state [44, 65, 129].

4.5 Conclusion

We fabricate S-hyperdoped silicon with dopant concentrations between 2.0×10^{18} and $1.3 \times 10^{19} \text{ cm}^{-3}$ using fs-laser hyperdoping at SF_6 pressures between 1 and 100 Torr. After furnace annealing, the sub-bandgap light absorption is significantly reduced, but the dopant concentration is sufficient to form a localized intermediate band below the insulator-to-metal transition. Our study shows that intermediate band formation is

not directly coupled with sub-bandgap absorption.

Using the two-band model, we can identify the location of the intermediate band and the donor concentration. To our knowledge, this is the first time the two-band model has been applied to a deep level IB. Analyzing the temperature-dependent Hall data, we find that at the highest dopant concentration ($1.3 \times 10^{19} \text{ cm}^{-3}$), the intermediate band is 70 meV below the conduction band edge. The analysis method is useful for studying hyperdoping with deep level dopants.

Chapter 5

Mid-infrared absorptance

Silicon hyperdoped with heavy chalcogen atoms via femtosecond-laser irradiation exhibits strong broadband, sub-bandgap light absorption. Understanding the origin of this absorption could enable applications for hyperdoped-silicon based optoelectronic devices. In this chapter, we measure absorption to wavelengths up to 14 μm using Fourier transform infrared spectroscopy and study sulfur-, selenium- and tellurium-hyperdoped Si before and after annealing. We find that absorption in the samples extends to wavelengths as far as 6 μm . After annealing, the absorption spectrum exhibits features that are consistent with free-carrier absorption. Although the surface morphology influences the shape of the absorption curves, the data permit us to place an upper bound on the position of the chalcogen dopant energy levels.

5.1 Introduction

Pulsed laser processing creates novel materials with ultrahigh dopant concentration and tunable surface textures for enhanced light absorption [130]. Many studies focus on femtosecond laser (fs-laser) doping of silicon with heavy chalcogens (sulfur, selenium, or tellurium) because the material exhibits strong light absorption both above and below the bandgap of silicon, indicating a change in the electronic band structure [2, 4, 7]. The resulting material is called hyperdoped silicon because the dopant concentrations can be as high as 1 at.%, three orders of magnitude above the equilibrium solid solubility limit [39, 42, 43]; and at least 20% of the dopant atoms occupy substitutional sites [8]. Thermal annealing changes the chemical state of the dopant atoms and decreases sub-bandgap light absorption [44, 65]. Although previous studies have shown that the sub-bandgap absorption extends down to at least 0.5 eV, a complete picture of the absorption mechanism remains unclear, as well as the influence of surface morphology and free-carrier absorption. Also, further investigation is necessary to understand the energy states introduced by the supersaturated dopants in silicon.

Chalcogen-doped silicon has been studied extensively for infrared detectors [131, 132]. Photodetectors fabricated from S-hyperdoped Si have sub-bandgap photon responsivity to energies as low as 0.83 eV [48]. Furthermore, if sub-bandgap absorption in hyperdoped Si is due to the presence of an intermediate band, this material system could have applications in high-efficiency photovoltaics [58]. Evidence of intermediate band formation, such as metallic-like conduction, has been observed in other hyperdoped Si systems [61, 64]. Therefore a better understanding of the energetics of

the chalcogen dopants is important for further development of hyperdoped Si-based optoelectronic devices.

In this chapter, we use mid-infrared absorption spectroscopy to study the dopant energy levels created in silicon hyperdoped with S, Se, or Te. Infrared (IR) spectroscopy yields information on transition probabilities between two energy states. Dilute chalcogen concentrations in silicon introduce occupied electronic states located between 100 and 300 meV below the conduction band edge [47, 133], and the energy levels of these states have been identified using IR absorption measurements [134–136]. At a concentration as high as 1 at.%, we expect the dopant energy levels to broaden into a band, and the absorption coefficient of an intermediate band formed by substitutional chalcogen atoms has been calculated using density-functional theory [64, 128]. For Si doped with non-equilibrium concentrations of chalcogens, broad-band sub-bandgap absorption is commonly reported in the range of 0.5 to 1.2 eV (1.0 – 2.5 μm) [2, 4, 7, 105, 137]. In this chapter, we find that strong absorption in chalcogen-hyperdoped silicon extends to energies smaller than 0.4 eV and in some samples to 0.2 eV (3 – 6 μm); the shapes of the absorption curves are sensitive to the surface morphology of the samples. Additionally, upon annealing, sub-bandgap absorptance decreases, and in the case of Se- and Te-hyperdoping, a broad resonance feature emerges. Analysis of the absorption data results in bounds on the location of the chalcogen dopant energy levels in hyperdoped silicon, and we find that in addition to chalcogen dopants, free carriers also contribute to sub-bandgap absorption after annealing.

5.2 Experimental

Silicon wafers ((100) orientation, float zone grown, p-type, $> 3000 \Omega\cdot\text{cm}$) are cleaned to remove organic and metallic contaminants [120]. The wafer is placed in a vacuum chamber and irradiated at normal incidence with Ti:sapphire laser pulses with 80-fs pulse duration (center wavelength at 800 nm and 1-kHz repetition rate). For S doping, the vacuum chamber is filled with sulfur hexafluoride (SF_6) gas at a pressure of 500 Torr. For Se or Te doping the dopant precursor is a thermally evaporated 65-nm Se or Te film directly on the silicon wafer, and the vacuum chamber is filled with nitrogen buffer gas at a pressure of 500 Torr. The laser pulses have an average energy of 1.1 mJ and are focused to a spot size of 500 μm (FWHM of a Gaussian beam) to achieve a fluence of 4 kJ/m^2 . A galvanometric scanning mirror system scans the laser beam across a $25 \times 25 \text{ mm}^2$ area and translates subsequent pulses by 50 μm such that any given spot in the irradiated region is exposed to 80 laser pulses. Using the same parameters, we fabricated a control sample (Si:N_2) in the absence of chalcogen dopants using only nitrogen buffer gas. We fabricated an additional S-hyperdoped sample (Si:S-2) at a higher fluence (8 kJ/m^2 and 50 pulses) to achieve comparable microstructures and sub-bandgap absorptance as the Se- and Te-hyperdoped (Si:Se and Si:Te) samples [138]. After laser irradiation, samples are treated in one of three ways: unannealed, annealed at 730 K, or at 990 K. Annealing is performed for 30 minutes in a nitrogen environment.

We study the optical and electronic properties of these samples. We collect integrated transmission (T) and reflection (R) spectra and calculate absorptance ($A = 1 - R - T$). A UV-VIS-NIR spectrophotometer is used for visible and near-IR

measurements (0.5 – 1.5 eV), and a Fourier transformed-infrared (FTIR) spectrometer is used for collecting mid-IR data (0.09 – 0.62 eV). Both the spectrophotometer and the FTIR spectrometer are equipped with integrating spheres in order to collect transmitted and reflected light at all angles. To study the electronic properties, we deposit 2-mm square Ti-Ni-Ag (20–20–200 nm, Ti adjacent to Si) contacts at four corners of the samples and perform resistivity and Hall measurements using the van der Pauw technique [121].

5.3 Results and discussion

5.3.1 Upper bound on dopant energy levels

The near-IR and mid-IR absorptance of fs-laser hyperdoped samples before thermal treatment is shown in Figure 5.1; reflectance and transmittance data are shown in Figure 5.2. For photons with energies greater than the bandgap of silicon, 1.1 eV, all samples exhibit enhanced photon absorption compared to the crystalline silicon substrate. Between 0.5 and 1.1 eV, all chalcogen-hyperdoped samples exhibit strong but featureless absorption. Below 0.5 eV, extended absorptance for chalcogen-hyperdoped Si decreases in the mid-infrared range, with the onset of a drop in absorptance varying with fabrication parameters.

As a comparison, at energies below the bandgap, the absorptance of a silicon substrate is approximately zero except at energies near the phonon vibrational modes (< 0.18 eV). A sample irradiated with the absence of chalcogen dopant precursors, Si:N₂, exhibit sub-bandgap absorption only due to structural defects (Urbach states)

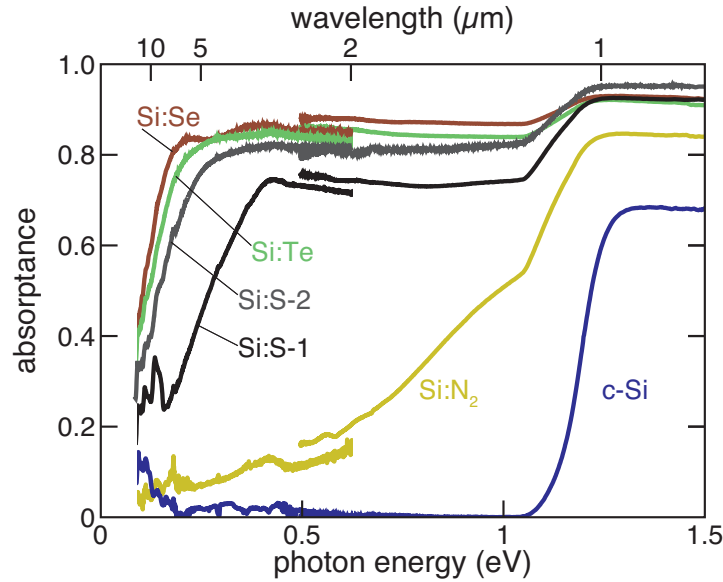


Figure 5.1: Absorptance of chalcogen-hyperdoped silicon. Data for a control sample (Si:N₂) and the silicon substrate (c-Si) are also plotted for comparison. Data from 0.09 to 0.62 eV was collected using an FTIR spectrometer and data from 0.5 to 1.5 eV was collected using a UV-VIS-NIR spectrophotometer. The mismatch between the data from two instruments at 0.5 eV is about 3%.

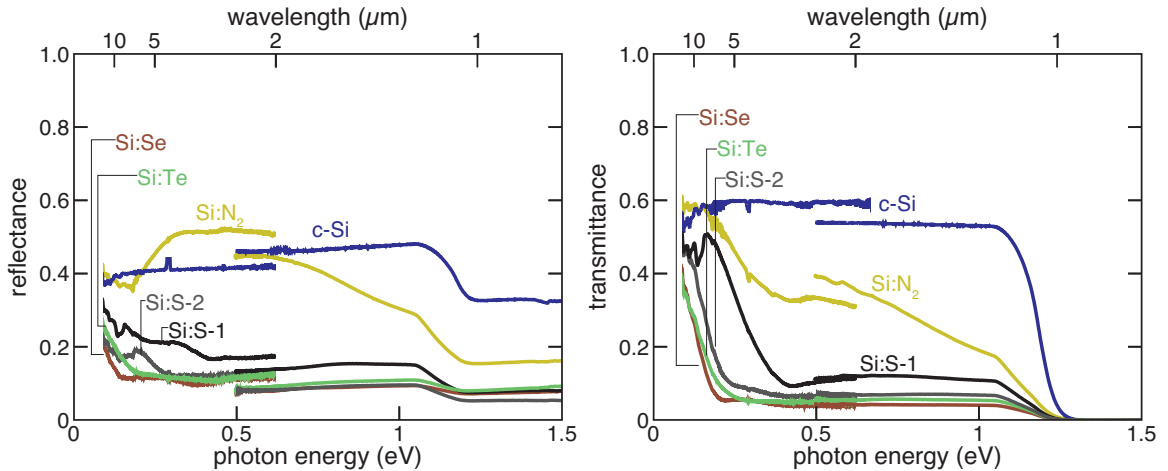


Figure 5.2: Reflectance (left) and transmittance (right) of chalcogen-hyperdoped silicon. Data for a control sample (Si:N₂) and the silicon substrate (c-Si) are also plotted for comparison.

[44, 139, 140]. A recent study shows that absorption related to structural defects is reduced by annealing at a moderate temperature ($T \geq 575$ K), while chemical states or absorption related to the chalcogen dopants are minimally affected [44, 65].

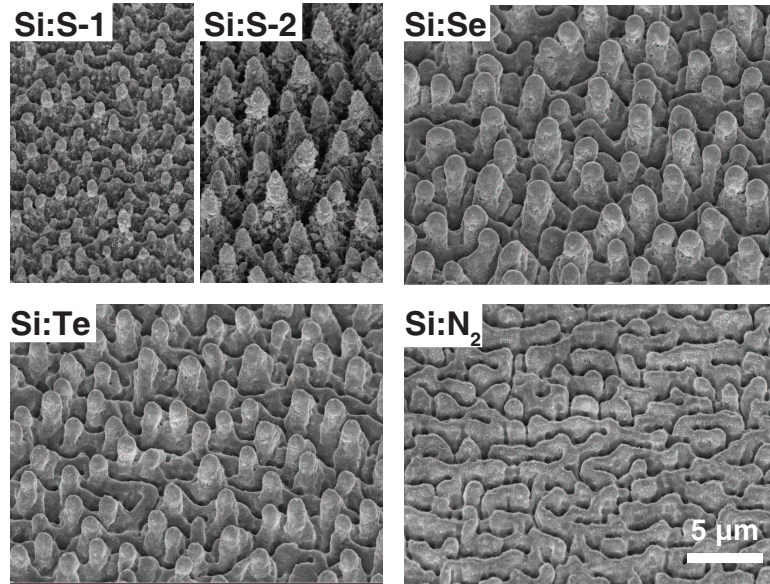


Figure 5.3: Scanning electron micrographs of fs-laser hyperdoped silicon. The images are taken at a 45° angle to the surface. Si:S-1, Si:Se, Si:Te and Si:N₂ are irradiated with the same fs-laser parameter: 4 kJ/m^2 , 80 pulses. Si:S-2 is irradiated with 8 kJ/m^2 , 50 pulses. After annealing, we examined all samples under SEM and observed no change in surface morphology in any of the samples.

Figure 5.3 shows scanning electron microscope (SEM) images of chalcogen-hyperdoped Si after fs-laser irradiation. The formation and structural characteristics of these samples have been discussed in detail in Ref. [138], and in this chapter we provide a brief summary of the difference in surface morphologies among the samples used in this study. First, Si:Se and Si:Te have similar surface morphologies. Under the same fabrication conditions, Si:S-1 has surface features that are smaller than Si:Se and Si:Te. At a higher laser fluence, Si:S-2 achieves similar feature size and compa-

Table 5.1: Average surface feature spacing w and height h .

Sample	w (μm)	h (μm)
Si:S-1	2.3 ± 0.2	3.1 ± 0.5
Si:S-2	3.0 ± 0.3	5.4 ± 0.6
Si:Se	3.8 ± 0.5	4.6 ± 0.6
Si:Te	3.8 ± 0.5	4.5 ± 0.9
Si:N ₂	0.9 ± 0.1	1.5 ± 0.5

able absorptance as Si:Se and Si:Te samples. By analyzing the SEM images, we obtain the average height (h) and spacing (w) of the surface features of these samples (Table 5.1).

Sub-bandgap absorption of chalcogen dopants arises from optical excitation of an electron from a dopant energy level to the conduction band. Thus, a low-energy cutoff of the sub-bandgap absorption could represent the smallest energy required to optically excite an electron from a dopant energy level to the conduction band edge. In the following paragraph, however, we discuss the influence of surface morphology on the shape of the absorption curves of hyperdoped silicon. As a result, Figure 5.1 does not directly provide the location of the dopant energy level, although it does permit an estimation of the maximum energy difference between the level and the conduction band.

Surface morphology can increase the absorption of incident light by reducing reflection and/or increasing the optical path length inside the absorber. Figure 5.4 illustrates how the morphology contributes differently to anti-reflection and light trapping for different wavelengths of light. For wavelengths smaller than about twice the separation between conical spikes ($\lambda < 2w$), reflectance is reduced because incident light reflects multiple times in between the spikes, reducing the total amount of light

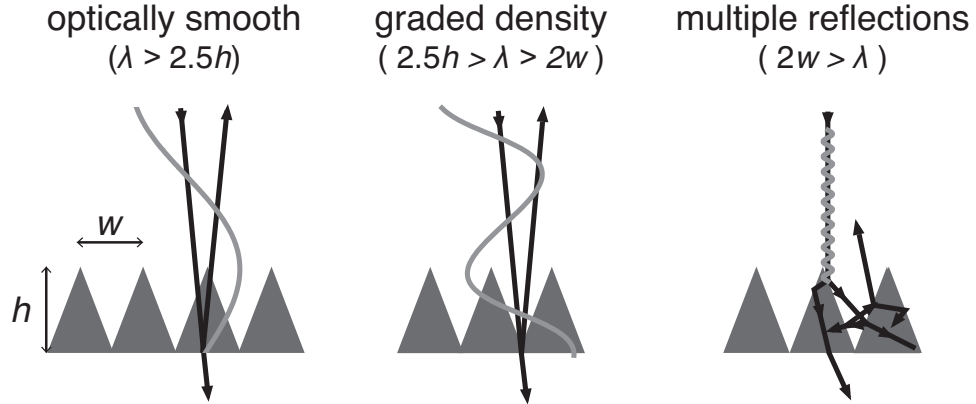


Figure 5.4: Illustration of light propagation through micrometer-scale structures with spacing w and height h . Three wavelength ranges represent different light and matter interactions: optically smooth (left), graded density (middle) and multiple reflections (right). The representative wavelengths are shown for the incoming light (gray); for each wavelength, three arrows indicate incoming, reflected and transmitted light.

reflected. The morphology also results in light trapping, because light enters the material at a non-normal angle, the total internal reflection angle of silicon in air is small, and the propagation path length is extended (Section 1.3.2). For longer wavelengths ($\lambda > 2w$), the length scale of the surface features is smaller than the wavelength of light and the silicon and air form an effective medium. In this regime graded density is the main cause of low reflectance [141]. A graded density material does not change the direction of light propagation, so there is no light trapping. Graded density is only effective when the wavelength is smaller than 2.5 times the height of the surface roughness [142], and at even longer wavelengths ($\lambda > 2.5h$), the surface appears optically smooth. Figure 5.5a illustrates how these surface features influence reflectance (due to anti-reflection) and transmittance (due to light trapping). Si:Se and Si:Te exhibit very similar surface morphologies: $w = 3.8 \mu\text{m}$ and $h = 4.6 \mu\text{m}$ (Table 5.1). Figure 5.5b shows that the reflectance and transmittance curves of these two samples

transition from high to low near wavelengths equal to $2.5h$ and $2w$, respectively. Although the transitions are not sharp, the transition wavelengths qualitatively agree with the analysis above. Similarly for Si:S-1 and Si:S-2, the transmittance and reflectance transition wavelengths qualitatively agree with the above analysis. Because the surface features are aperiodic, numerical simulation is challenging and we currently do not consider the quantitative details regarding changes in the optical path length and reflectivity as a function of wavelength, but this analysis shows that the infrared behavior is at least in part determined by the morphology of the surface.

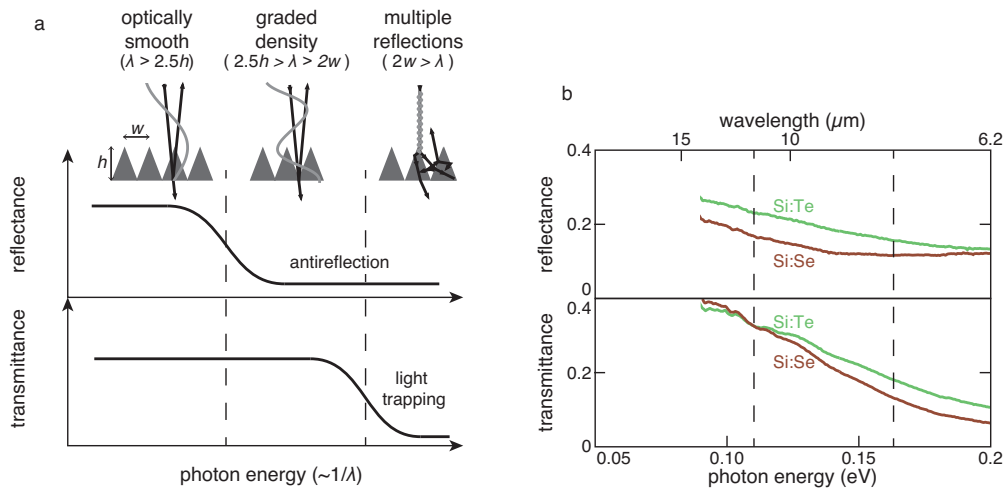


Figure 5.5: (a) Illustration of light propagation through micrometer-scale structures and the corresponding reflectance and transmittance as a function of photon energy (proportional to inverse wavelength). (b) Reflectance and transmittance spectra of Si:Se (brown) and Si:Te (green) between 0.09 and 0.2 eV. The vertical dash lines at 0.11 eV (11.3 μm) and 0.16 eV (7.6 μm) correspond to transition wavelengths at $2.5h$ and $2w$, respectively.

The characteristics of sub-bandgap absorption depend on laser irradiation parameters, and it is illustrative to compare the absorptance curves of the two S-hyperdoped Si samples fabricated under different conditions. Si:S-2 (irradiated with higher laser fluence) has larger surface features (Figure 5.3) and the absorptance

is higher overall than Si:S-1 (Figure 5.1). Furthermore, for Si:S-1 the broad-band absorption extends to 0.42 eV and for Si:S-2 to 0.25 eV. Similar findings have been reported for different laser irradiation parameters in another S-hyperdoping study [14]. Previously we showed that the sulfur concentration in these two samples are comparable [2], and hence the dopant-related absorption coefficients should be similar. Following our analysis of Figure 5.5, the difference in the surface morphology between Si:S-1 and Si:S-2 leads to differences in anti-reflection and light trapping, as evidenced by the variation in infrared behavior.

Thus, it is clear that the location of the absorption edge is influenced by surface roughness, and the absorption turn-offs in the mid-IR range shown in Figure 5.1 cannot be directly correlated to the energetics of the dopant atoms. However, because surface roughness can only serve to increase existing absorption mechanisms, the location of the turn-offs does place an upper bound on the energy gap between dopant energy levels and the conduction band edge, which is around 0.25, 0.20 and 0.21 eV for Si:S, Si:Se and Si:Te, respectively.

5.3.2 Broad resonance features after annealing

Figure 5.6 shows mid-IR absorption spectra of each chalcogen-hyperdoped silicon sample before and after annealing. The above-bandgap absorptance (not shown), is unaffected by annealing [7] while sub-bandgap absorptance decreases with increasing annealing temperature. The reduction of sub-bandgap absorption agrees with earlier results we obtained, showing that the sub-bandgap absorption decreases smoothly with the diffusion length of dopant atoms [44]. For Si:Se, a resonance feature at 0.21

eV emerges after annealing at both 730 and 990 K, and for Si:Te a resonance signal emerges at 0.26 eV after annealing at 990 K. We also observe a broad maximum for Si:S-2 after annealing at 730 K, but after annealing at 990 K the sub-bandgap absorptance deactivates completely.

S-hyperdoped Si samples exhibit a broad oxide absorption band at 0.13 – 0.15 eV (gray line in Figure 5.6: Si:S-2), which can be removed with a dilute hydrofluoric acid (5% HF) etch. In addition, we identify features associated with phonon vibrations and other contaminants labeled in Figure 5.6. We do not observe — either before or after annealing — any absorption lines from dilute chalcogen dopants (ranging from 0.1 to 0.3 eV) [47,133] nor any absorption features related to sulfur compounds [146]. Due to the low signal below 0.09 eV, our measurement is not sensitive to absorption bands of possible precipitated compounds such as SiS₂, SiSe, SiSe₂ or Si₂Te₃ [147–149]. Additional absorptance measurements at low temperature and at far-IR wavelengths could be useful for probing vibrational and electronic transitions with energies below 0.09 eV [150–152].

After annealing, broad resonance signals emerge for chalcogen-hyperdoped silicon, and for the purpose of this discussion we focus on the Si:Se and Si:Te samples annealed at 990 K. The width of these resonances suggests that these local maxima are due to a combination of energy-dependent processes instead of a resonance transition between two energy states. For example, a broad maximum near the absorption edge could emerge by combining these two effects: free-carrier absorption and light trapping. Free-carrier absorption increases with reducing photon energy, but reduced light trapping for energies below 0.16 eV ($\lambda < 2w$) decreases the overall absorption

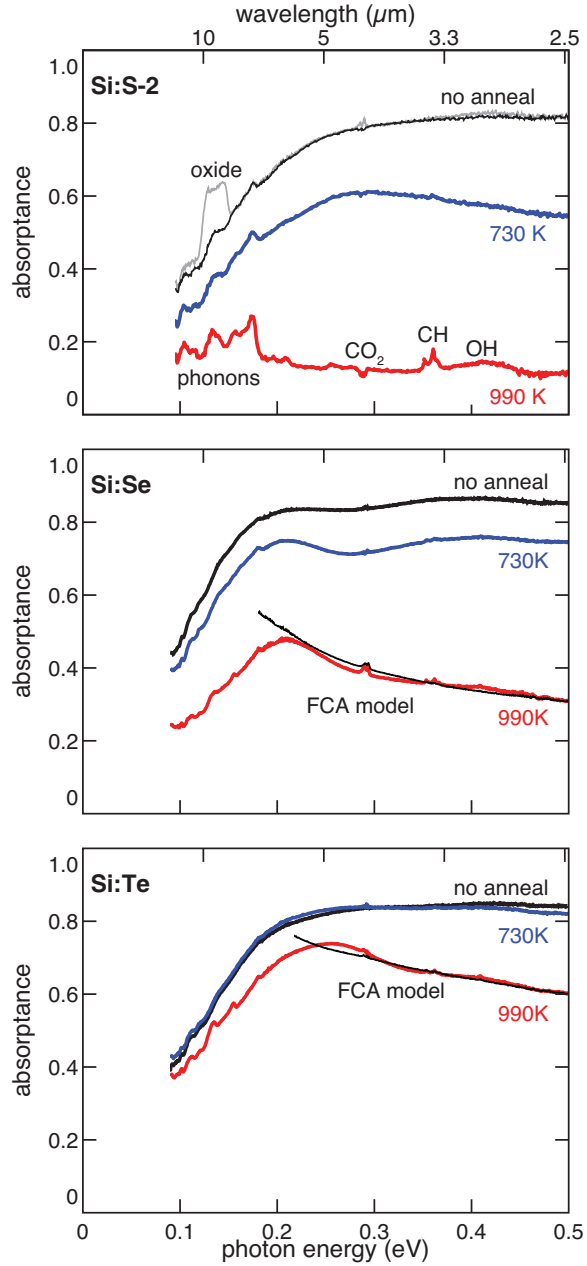


Figure 5.6: Mid-infrared absorbance of Si:S-2, Si:Se, and Si:Te before (black) and after annealing at 730 K (blue) and 990 K (red). Except for the gray line, all Si:S-2 data are taken after a 5% HF etch for 1 min and the surface oxide absorption band from 0.13 to 0.15 eV is removed. Labels correspond to absorption features phonon vibrations and other contaminants: hydroxide (OH; centered at 0.42 eV) [143], hydrocarbon (CH; three peaks near 0.36 eV) [143], silicon phonons (below 0.13 eV and between 0.16 – 0.18 eV) [144], and CO₂ molecules in the spectrometer (0.29 eV) [145]. The curves are fits of the free carrier absorption model between 0.3 and 0.5 eV using Eq. 5.2: $A(\varepsilon) = [1 - R(\varepsilon)](1 - ye^{-x/\varepsilon^2})$.

and thus results in a local maximum.

We fit the absorption curves at energies higher than the resonances as a combination of absorption due to free carriers and dopant atoms. The free-carrier absorption coefficient, α_{FCA} , is proportional to the carrier concentration, n , as well as the square of the wavelength, λ , ($\alpha_{\text{FCA}} \approx 2 \times 10^{-18} \lambda^2 n$, λ in units of μm and n in units of cm^3) [52]. Figure 5.6 shows fits to the data between 0.3 and 0.6 eV with an absorptance estimated from Beer’s law:

$$A = (1 - R)(1 - e^{-(\alpha_{\text{FCA}} + \alpha_{\text{dopant}})dm}). \quad (5.1)$$

A and R are the measured absorptance and reflectance, respectively; d is the thickness of the hyperdoped layer which is enhanced by a factor of m due to light trapping; and α_{dopant} represents dopant-related light absorption that persists after annealing. In the range between 0.3–0.6 eV, we assume α_{dopant} is energy independent [64] and so is m from the light-matter interaction discussion above. We can then rewrite Eq. 5.1 as

$$\frac{A(\varepsilon)}{1 - R(\varepsilon)} = 1 - ye^{-(x/\varepsilon^2)}, \quad (5.2)$$

where ε is the photon energy, y and x are fitting parameters ($x = 3 \times 10^{-18} n_{\text{sheet}} m$, [eV²]). The numerical fit yields $x = 0.04$; $y = 0.49$ for Si:Se, and $x = 0.04$; $y = 0.24$ for Si:Te.

The good fits between the data and model described above support our hypothesis that free carriers contribute to the shape of the absorption curves. We compare this fitting result with electronic measurements. Table 5.2 summarizes the electronic measurements of Si:Se and Si:Te after annealing at 990 K, and the measured majority carriers are electrons. Both Si:Se and Si:Te have similar sheet carrier concentrations

Table 5.2: Hall-effect and resistivity measurements of Se- and Te-hyperdoped Si after annealing.

Sample	Annealing temperature (K)	Sheet resistance (k Ω)	Sheet carrier concentration (10^{12} cm $^{-2}$)	Mobility (cm 2 V $^{-1}$ s $^{-1}$)
Substrate	–	146	0.11	380
Si:Se	990	2.2	–6.2	466
Si:Te	990	1.5	–6.0	692

suggesting the free-carrier absorption is similar for both samples, and we indeed obtain identical fit values of x for the two samples.

While the absorption and the electronic measurements qualitatively agree, the value for x calculated using n_{sheet} in Table 5.2 is much smaller than the fitted value. Even with maximum light trapping ($m = 49$) [153], the measured carrier concentration is still two orders of magnitude too small to explain the absorption with free carriers only. This discrepancy could arise because the measured sheet carrier concentration is an average value of a non-uniform dopant distribution, and the situation is further complicated by the rough surface and non-uniform thickness of the hyperdoped layer [138]. It is also possible, instead of free-carrier absorption, other wavelength-dependent mechanism is contributing to the spectral dependence of absorption in the range of 0.3 to 0.5 eV [154, 155]. Here we emphasize the local maximum observed in the annealed samples is due to a combination of energy-dependent processes.

In summary, in addition to broad-band absorption due to dopant atoms, the low energy optical absorption displays the spectral dependence of free-carrier absorption (increasing with λ^2) for Si:Se and Si:Te annealed at high temperature. The carrier concentration obtained from the electronic measurements, however, is too small to

account for all the free-carrier absorption observed. We believe this discrepancy is due to the complications introduced by the rough surface, but we also cannot exclude other possible wavelength-dependent absorption mechanism [154, 155]. The combination of different wavelength-dependent processes, such as free-carrier absorption, which increases with wavelength, and light trapping, which decreases with wavelength, explains the observed broad resonance.

5.4 Conclusion

We report mid-IR absorptance measurements of chalcogen-hyperdoped silicon, identify the influence of surface morphology on the absorptance curves, and place bounds on the location of the dopant energy levels. The surface morphology resulting from laser irradiation enhances anti-reflection and light trapping, and the low-energy cutoff of the mid-IR absorption is sensitive to the surface morphology. Our data place an upper bound on the energy difference between the dopant energy level and the conduction band of about 0.2 eV. After annealing, the sub-bandgap absorptance decreases and broad resonance features emerge that do not correspond to known defect absorption lines. We attribute the broad resonance features observed in Si:Se and Si:Te to competing wavelength-dependent processes, including free-carrier absorption and wavelength-dependent light trapping. Finally, we emphasize the importance of taking into account the effect of surface roughness when analyzing and comparing optical and electronic measurements.

Chapter 6

Reactivation of sub-bandgap absorption

Silicon doped with non-equilibrium concentrations of chalcogens using a femtosecond laser exhibits near-unity absorption of sub-bandgap photons to wavelengths of at least 2500 nm. Previous studies have shown that sub-bandgap absorptance decreases with thermal annealing up to 1175 K, and that the absorption deactivation correlates with chalcogen diffusivity. In this chapter, we show that sub-bandgap absorptance can be reactivated by annealing at temperatures between 1350 K and 1550 K for 30 minutes followed by fast cooling (> 50 K/s). Our results suggest that the defects responsible for sub-bandgap absorptance are in equilibrium at high-temperatures in hyperdoped Si:chalcogen systems.

6.1 Introduction

Hyperdoping silicon with heavy chalcogens (sulfur, selenium, or tellurium) to orders of magnitude above room-temperature solubility results in strong sub-bandgap absorptance to at least 2500 nm [2, 7]. Hyperdoped silicon has a potential use in infrared detectors [48], light emitting diodes [156], and a wide range of other semiconductor devices [157]. However, the exact mechanism for the enhanced broadband absorptance is not yet well understood.

Previous research demonstrated that thermal annealing of hyperdoped silicon decreases absorption of photons with energy less than the bandgap [2, 44] (Section 5.3.2). The sub-bandgap absorptance decreases with increased annealing time and temperature up to 1175 K. After annealing, the sub-bandgap absorptance is a function of dopant diffusion lengths, regardless of the dopant species (S, Se, or Te) [44]. It was suggested that precipitation of supersaturated dopant species at heterogeneous nucleation sites, such as grain boundaries, may cause the deactivation of the sub-bandgap absorptance [44].

In this chapter, we probe the thermodynamics of sub-bandgap absorptance at higher temperatures and observe a behavior not predicted by the previously proposed diffusion/precipitation model. Thermal annealing at temperatures above 1350 K followed by rapid cooling maintains sub-bandgap absorptance in hyperdoped silicon for both sulfur and selenium dopants. We also show that the fraction of sub-bandgap photons absorbed depends on the cooling rate, suggesting a kinetically limited process. Furthermore, sub-bandgap absorptance is reactivated in samples where it has previously been deactivated by annealing. In addition to offering insight into the na-

ture of the sub-bandgap absorptance in hyperdoped silicon, these results demonstrate that the sub-bandgap absorptance can be thermally engineered and controlled to optimize device characteristics and performance, increasing the practical applications of chalcogen hyperdoped silicon.

6.2 Experimental

To explore the high-concentration, high-temperature regime of the Si:chalcogen system, we hyperdoped a set of c-Si samples with sulfur and selenium using amplified fs-laser pulses (average energy of 1.7 mJ). We used boron-doped silicon (100) wafers ($\rho > 100 \Omega\text{-cm}$). For sulfur hyperdoping, the wafer is placed on a translation stage in a chamber filled with sulfur hexafluoride (SF_6) gas to 500 Torr. For selenium hyperdoping, we thermally evaporate a thin 65-nm selenium film (99.95% purity) onto the wafer before loading the sample into the chamber filled with nitrogen to 500 Torr. We irradiate a $20 \times 40 \text{ mm}^2$ area of the wafers with 80-fs, 800-nm Ti:sapphire laser pulses. The fluence and shots per area for S hyperdoping is 8 kJ/m^2 and 50 S/A, respectively, and for Se hyperdoping, the fluence is 4 kJ/m^2 and the shots per area is 88. After laser irradiation, the surface layer of the silicon wafer is heavily doped with sulfur or selenium with concentrations between 10^{20} to 10^{21} cm^{-3} [7]. The surface is transformed into a rough landscape of micrometer-scaled spikes. The formation and structural characteristics of these spikes are discussed elsewhere [1]. As a control sample, we laser irradiated silicon without dopant precursor in a nitrogen environment.

After fs-laser hyperdoping, samples were cut into $5 \times 5 \text{ mm}^2$ squares for an-

nealing in a vertical tube furnace at a temperature between 1070 and 1600 K. We annealed each sample separately on a clean quartz sample holder and measured the temperature with an R-type thermocouple located at the same height. After 30 minutes, the sample was cooled in one of three ways: dropped into silicone oil for fast quenching (250 K/s); removed from the furnace and air quenched on the quartz sample holder (50 K/s); or cooled in a controlled manner inside the furnace at 0.25 K/s to room temperature. To test reversibility of the thermal treatments, we annealed two Si:S samples at 1070 K for 30 minutes, and then performed a second thermal treatment. The second thermal treatment consisted of either a higher temperature furnace anneal at 1510 K or a second fs-laser irradiation with the same parameters as the first, except in a dopant-free environment.

After annealing, the spectrally dependent transmission (T) and reflection (R) was measured using a UV-VIS-NIR spectrophotometer with an integrating sphere. Absorptance is calculated as $A = 1 - R - T$. A sample that is not annealed exhibits near unity absorptance from 400 to 2500 nm for both Si:S and Si:Se. For characterization, we average sub-bandgap absorptance from 1250 to 2500 nm. We estimate light scattering out of the integrating sphere to cause an overestimation of the absorptance by at most 0.07.

6.3 Results

Figure 6.1 shows the average sub-bandgap absorptance of samples annealed between 1070 and 1600 K. For both Si:S and Si:Se, we observe enhancement of the sub-bandgap absorptance for samples annealed above 1350 K and then rapidly quenched.

Samples annealed at higher temperatures exhibit stronger absorptance. However, as the temperature approaches 1550 K, the absorptance decreases. Scanning electron microscopy of the surface of these Si:Se samples suggests that local surface melting occurs during annealing. Redistribution of dopant atoms on the surface or dopant evaporation could explain the sudden drop in sub-bandgap absorptance.

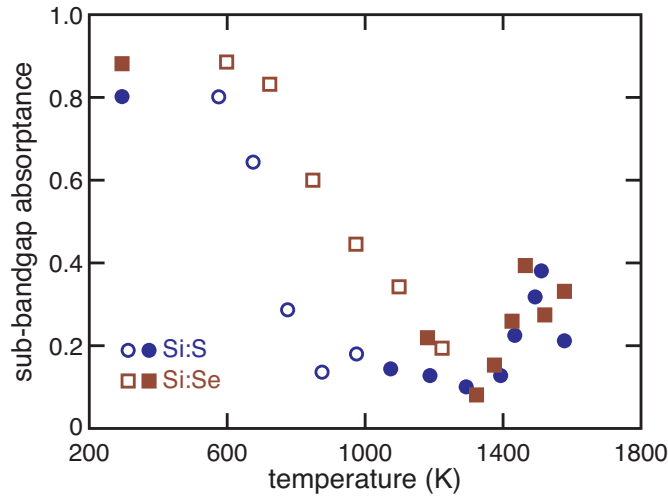


Figure 6.1: Average sub-bandgap absorptance for Si:S (*circles*) and Si:Se (*squares*) hyperdoped silicon after high-temperature anneals followed by oil quenching (250 K/s) for Si:S samples or air quenching (50 K/s) for Si:Se samples. Data points at 295 K are samples before annealing. Measureable increases in sub-bandgap absorptance occur at temperatures above 1350 K. Standard deviations of all data points are less than 0.05. Data points with unfilled symbols are from Refs [44] (Si:S) and [65] (Si:Se).

We verified that enhanced sub-bandgap absorptance depends on the presence of the dopant atoms by performing a high-temperature anneal at 1490 K followed by quenching of two control samples: (1) a bare c-Si wafer that was not hyperdoped and (2) a sample irradiated with fs-laser in a nitrogen environment, containing no dopant but exhibiting micrometer-scaled surface features. The bare c-Si wafer exhibits average sub-bandgap absorptance of 0.02 ± 0.01 after annealing and quench. Sub-

bandgap absorptance of the nitrogen sample after annealing is measured at 0.10 ± 0.02 . Much of this measured sub-bandgap absorptance is likely due to light scattering effects, as noted above.

The amount of sub-bandgap absorptance depends on the cooling rate from high temperature. Figure 6.2 shows the results of cooling at different rates. The sample quenched at 250 K/s exhibits the largest average sub-bandgap absorptance (0.33 ± 0.01), followed by the sample quenched at 50 K/s (0.24 ± 0.02), and finally the sample that underwent controlled cooling at 0.25 K/s (0.14 ± 0.02).

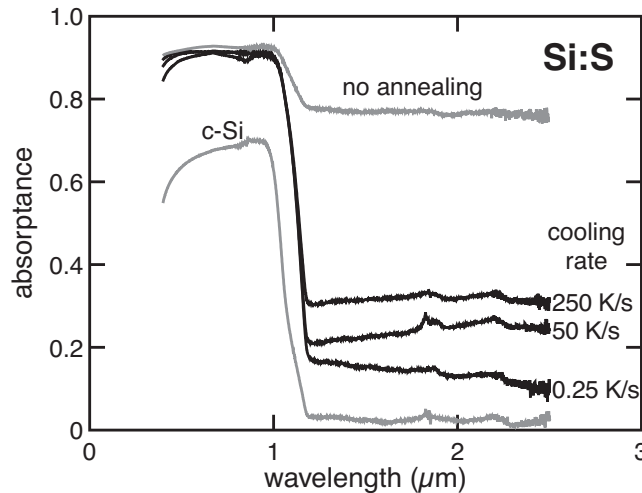


Figure 6.2: Absorptance as a function of cooling rate for Si:S samples. Samples were annealed at 1490 K for 30 minutes. The cooling rates are derived from a one-dimensional convection model for cooling from 1520 K to 1100 K in different media. Absorptance data of a untreated, crystalline silicon wafer and a Si:S sample prior to annealing are included for comparison.

Sub-bandgap absorptance is reactivated in samples where it was previously deactivated by annealing. We performed two-step anneals summarized schematically in Figure 6.3. A Si:S sample was annealed at 1070 K for 30 minutes and quenched in air, resulting in an average sub-bandgap absorptance of 0.12 ± 0.01 . The same sam-

ple was then re-annealed at 1510 K for an additional thirty minutes followed by oil quench. We find that the average sub-bandgap absorptance increases to 0.24 ± 0.01 . A Si:S control sample, annealed only once at 1510 K has an average sub-bandgap absorptance of 0.38 ± 0.02 .

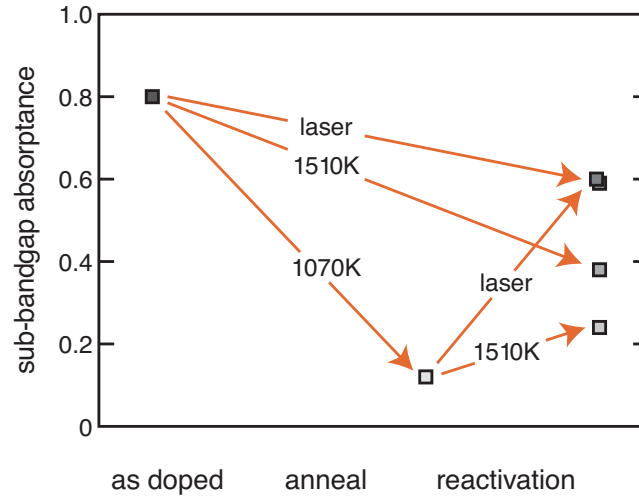


Figure 6.3: Schematic of the two-step annealing process that first deactivates the sub-bandgap absorptance by annealing at 1070 K and then reactivates it via one of two methods: high temperature (1510 K) annealing and quenching or laser irradiation. Control samples are also shown for comparison.

Figure 6.3 shows the sub-bandgap absorptance is also reactivated by a second fs-laser treatment. Sub-bandgap absorptance of a Si:S sample was first deactivated by annealing at 1070 K for 30 minutes and was reactivated to 0.59 ± 0.04 after a second laser irradiation in a nitrogen environment. We compare this to a control sample that was laser-irradiated twice, first for hyperdoping, and the second time with no dopant present and no anneal in between (average sub-bandgap absorptance = 0.60 ± 0.02). This corresponds to an almost complete restoration of the sub-bandgap absorptance. The slight decrease in absorptance for both samples after the second laser-irradiation

is likely due to loss of dopant atoms through laser ablation.

6.4 Discussion

The results presented in this chapter show that sub-bandgap absorptance is reactivated through high-temperature annealing. The amount of sub-bandgap absorptance depends on the rate of post-anneal cooling, suggesting a kinetically limited deactivation process.

In the intermediate temperature regime, from 1070 K to 1350 K, annealing followed by quenching results in deactivation of sub-bandgap absorptance in agreement with previous results of annealing followed by slow cooling (Figure 6.1). If we correlate the sub-bandgap absorptance to the concentration of an optically active defect state, we note the similarities of the results in Figure 6.1 to a time-temperature-transformation diagram describing the precipitation of supersaturated point defects at heterogeneous nucleation sites, as previously reported for Si:Fe [158]. At lower temperatures, the precipitation of supersaturated point defects is energetically favorable but kinetically limited by diffusion. At higher temperatures, the equilibrium solubility of point defects increases with temperature.

The enhanced broadband absorptance of chalcogen-doped silicon is only observed in samples with supersaturated chalcogen concentrations, and the origin of the sub-bandgap absorption is not yet well understood. Chalcogen defect centers have been studied extensively in diffusion experiments; isolated substitutional impurities and dimer pairs are the most common point defects, and other more complex defect centers have been identified [47, 159]. These known defect centers introduce

deep states that allow sub-bandgap photon absorption, however, in samples with chalcogen dopant concentrations up to $7 \times 10^{16} \text{ cm}^{-3}$, no significant broad-band, sub-bandgap absorptance has been reported [131, 134]. In fs-laser chalcogen-hyperdoped silicon studied in this chapter, the initial dopant concentration [7] is at least 1000 times larger than the high-temperature equilibrium solubility achieved via solid-state thermal diffusion from a chalcogen-rich surface source: $3 \times 10^{16} \text{ cm}^{-3}$ for S and $2 \times 10^{17} \text{ cm}^{-3}$ for Se [39, 42, 159]. Our results suggest that a point defect state associated with higher concentrations of chalcogen dopant atoms and with unique optical characteristics is stable at temperatures higher than 1350 K in these samples. Further structural studies to identify this chemical state are underway.

6.5 Conclusion

High-temperature annealing followed by quenching of silicon hyperdoped with sulfur or selenium results in the reactivation of sub-bandgap optical absorptance that is not explained by previous models. Sub-bandgap absorptance is maintained in hyperdoped samples annealed above 1350 K and cooled at rates faster than 50 K/s. A high concentration of point defects stable at high temperatures may be responsible for absorption of sub-bandgap photons. Our results demonstrate an ability to control sub-bandgap absorptance in Si:chalcogen hyperdoped systems using thermal processing.

Chapter 7

Summary and future directions

We investigate a diverse range of scientific concepts in this thesis. Intermediate-band materials have potential for novel optoelectronic applications such as highly-efficient solar cells. Femtosecond laser hyperdoping and texturing is promising for fabricating an intermediate-band material with enhanced light absorption. In this thesis, we use chalcogen-hyperdoped silicon as a model system to study (1) the fs-laser doping techniques and (2) the intermediate band properties. To conclude, we summarize the findings in this thesis and provide future research directions.

7.1 Summaries

In Chapter 3, we study the fundamental hyperdoping mechanism and offer insight toward designing the dopant concentration profiles of intermediate-band silicon. After fs-laser hyperdoping, we probe the dopant concentration profiles using secondary ion mass spectrometry (SIMS). By varying the pressure of the dopant precursor (SF_6), we

identify that the surface adsorbed molecules are the dominant source of the dopant atoms. Furthermore, we show the material microstructure is improved and the sample hyperdoped at a fluence of 2.5 kJ/m^2 is single crystalline. We control the dopant incorporation depth, concentration, and crystallinity by varying the number of laser pulses, pressure of the dopant precursor, and laser fluence, respectively.

In Chapters 4 and 5, we investigate the intermediate band energetics using electronic transport and optical measurements. We find that light absorption of chalcogen-hyperdoped Si extends to wavelengths as far as $6 \mu\text{m}$. Results from the optical measurements are influenced by the morphology of the surface; however, the data permit us to obtain an upper bound of the intermediate band at 0.2 eV below the conduction band edge. After furnace annealing, the hyperdoped layer and the substrate form a p-n junction and the hyperdoped layer is electrically isolated from the substrate. The temperature-dependent Hall and resistivity measurements of the annealed samples show the dopant concentration is sufficient to form an intermediate band at a concentration just below the insulator-to-metal transition. We use a two-band model to analyze the transport data and the model indicates the localized intermediate band is at $70 \pm 10 \text{ meV}$ below the conduction band edge.

After fs-laser hyperdoping, thermal annealing is necessary to improve the material quality for studying the material's electronic properties. The sub-bandgap absorption, however, decreases with thermal annealing. In Chapter 6, we explore annealing at high temperatures and show that the sub-bandgap absorption is reactivated by annealing at temperatures between 1350 K and 1550 K followed by fast cooling ($> 50 \text{ K/s}$). Results shown in Chapter 6 offer solutions to reactivate sub-bandgap light

absorption after it had been deactivated by thermal annealing.

7.2 Future directions

For future studies on fs-laser hyperdoping, there are a number of opportunities. In Chapter 3, we investigate fs-laser hyperdoping with a gas-phase dopant precursor. It is important to point out that the dopant precursor is not limited to gas molecules. For example for Se- and Te-hyperdoped silicon discussed in Chapters 5 and 6, the dopant precursor is a thermally evaporated solid film of the dopant precursor on silicon. In a collaboration work, we have studied hyperdoping with solid-phase dopant precursor extensively [103,138]. Other novel methods such as liquid phase or electrospray could be used to achieve efficient dopant delivery.

In Chapter 3, we suggest that a laser beam with a flat-top intensity profile will simplify the fabrication process and help maintain the crystallinity of the hyperdoped silicon over a large area. Moreover, in addition to spatially engineering the laser beam, we can also change the laser pulse in the time domain. With temporal pulse shaping, a fundamentally new energy deposition profile is achieved by changing the power of the laser pulse as a function of time [160]. An example of pulse shaping is to convert a single pulse into multiple sub-pulses with the first pulse above the melting threshold to melt the material followed by lower fluence sub-pulses to change the resolidification dynamics. By varying the energy deposition as a function of time, we can alter the melt depth, duration, and resolidification dynamics. This offers another parameter space for engineering the desired dopant distribution profile and material crystallinity.

We are interested in the intermediate band property that contributes to the sub-

bandgap light absorption. Currently we cannot obtain reliable electronic transport data without furnace annealing. Thus it is promising to perform pulse engineering either in the time or spatial domain to hyperdope a large area free of laser-induced defects and amorphous silicon. Furthermore, in Chapter 6, we demonstrate reactivating sub-bandgap absorption after low temperature (< 1075 K) thermal annealing. Performing electronic measurements on samples with reactivated sub-bandgap absorption is also promising. Annealing the entire sample at 1510 K for 30 min followed by a rapid quench, however, introduce unwanted thermal stress and substantial dopant diffusion. Thus, future work on reactivation should concentrate on local heating methods such as laser annealing or rapid thermal processing with lamp-based heating.

For future studies on the properties of intermediate-band materials, many questions still remain. Intermediate-band photovoltaic is first proposed more than 15 years ago [58], and so far no device has demonstrated improved efficiencies [60, 161, 162]. Understanding the optical and electronic properties of intermediate-band materials is crucial for designing an intermediate-band device. For example, how wide is the intermediate band? Is it possible to fabricate a delocalized band that is isolated from the conduction or the valence band edge? Moreover, what is the dynamics of the photo-generated carriers? Knowledge of the mobility and the life time of carriers in an intermediate band is important for designing the device geometry. Many more material characterization techniques should be developed and employed to study the nature of an intermediate band.

The outlook for femtosecond-laser hyperdoping and intermediate-band materi-

als is bright. Our work fit in the emerging fields of defect engineering and band-gap engineering. In this thesis, we study the fs-laser hyperdoping technique and intermediate band properties of chalcogen-hyperdoped silicon. Chalcogen-hyperdoped silicon is a good model system for us to begin to understand properties of an intermediate band. Many of the analysis techniques we develop can also be applied to other material systems. We believe that, in the near future, we will be able to tune and design the optical and electronic response of material through hyperdoping.

Appendix A

The Hall effect

We first present a brief introduction of the Hall effect. Then we discuss the case where there are two types of carriers in a semiconductor (electrons and holes, or carriers in the conduction band and carriers in the intermediate band). In this appendix, we derive Eq. 4.6 and 4.7 in Chapter 4.

A.1 Introduction

Figure A.1 shows the schematic of Hall effect measurements. We obtain the carrier concentration n from the measured Hall voltage V_H , the applied current I , and the applied magnetic field B . That is:

$$n d = r_H \frac{IB}{qV_H}, \quad (\text{A.1})$$

where d is the thickness of the semiconductor, and q is the elementary charge. We present the derivation below. We write the equation of motion of a moving charge q

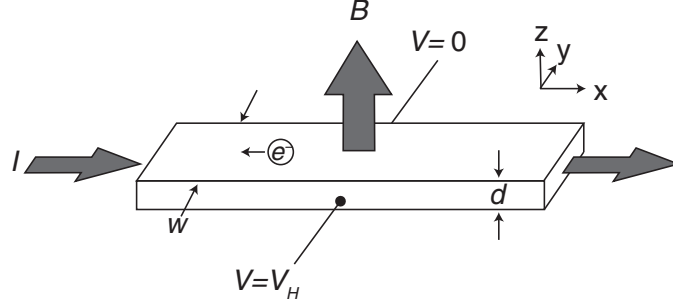


Figure A.1: Schematic of the Hall effect measurement. The semiconductor has width w and thickness d . We apply a magnetic field B in the $+z$ direction, a current I in the $+x$ direction and measure the Hall voltage V_H in the y -direction. Figure adapted from Ref. [122].

with velocity \vec{v} in the presence of an electric field \vec{E} and a magnetic field \vec{B} :

$$m \frac{d\vec{v}}{dt} = q\vec{E} + q\vec{v} \times \vec{B}. \quad (\text{A.2})$$

Using the directions defined in Figure A.1 ($\vec{B} = B\hat{z}$), we rewrite Eq. A.2 in the x - and y -components:

$$m \frac{dv_x}{dt} = qE_x + qv_y B, \quad (\text{A.3})$$

$$m \frac{dv_y}{dt} = qE_y - qv_x B. \quad (\text{A.4})$$

In equilibrium, the electric force in the y -direction due to the Hall voltage cancels out the magnetic force, so no current flows in the y -direction and $v_y = 0$. Eq. A.3 then describes charge carrier movement in the presence of only a electric field. It is necessary to include scattering in charge transport, so we consider an average scattering time, τ , of the charge carriers that leads to an average velocity, \bar{v}_x . Replacing dv_x/dt in Eq. A.3 with \bar{v}_x/τ , the drift velocity is

$$\bar{v}_x = \frac{q\tau}{m} E_x = \mu E_x. \quad (\text{A.5})$$

The factor $q\tau/m$ is also called the drift mobility μ .

Since in equilibrium $\nu_y = 0$, then $d\nu_y/dt$ is also zero. Eq. A.4 then becomes $0 = qE_y - q\nu_x B$. Replacing ν_x using the expression in Eq. A.5, we have

$$E_y = B\mu E_x. \quad (\text{A.6})$$

The Hall coefficient R_H is defined as $R_H = E_y/(J_x B)$. The current density is $\vec{J} = \sigma \vec{E} = qn\mu \vec{E}$, where σ is the conductivity of the material and μ is the mobility of the charge carriers. Apply Eq. A.6 to the Hall coefficient, we have:

$$R_H = \frac{E_y}{J_x B} = \frac{B\mu E_x}{qn\mu E_x B} = \frac{1}{qn}. \quad (\text{A.7})$$

Moreover, from the geometry shown in Figure A.1, $E_y = V_H/w$ and $J_x = I/(wd)$, so R_H is also

$$R_H = \frac{E_y}{J_x B} = \frac{V_H/w}{\frac{I}{wd} B} = \frac{V_H d}{IB}. \quad (\text{A.8})$$

Finally, equating Eq. A.7 and A.8, we show that the carrier concentration is indeed Eq. A.1

$$n d = \frac{IB}{qV_H}.$$

This simple derivation does not include the Hall scattering factor r_H which takes into account that the scattering time τ is a statistical average of scattering time due to many different scattering mechanisms [125].

A.2 Two types of carriers

We consider a more complicate scenario where there are two types of carriers. The goal of this section is to show the origin of Eq. 4.6 in Chapter 4:

$$\frac{1}{n_H} = \left(\frac{\sigma_c}{\sigma_H}\right)^2 \frac{1}{n_c} + \left(\frac{\sigma_i}{\sigma_H}\right)^2 \frac{1}{n_i}, \quad (\text{A.9})$$

where we use subscripts c , i , and H to denote properties of the CB, IB, and the transport measurements (Hall and resistivity), respectively. This derivation is the same as considering these two types of charge carriers: electrons and holes (detailed in Ch. 5 of Ref. [124]). In this section, we derive equations for a general case and label the two types of carriers 1 and 2.

If there are two types of carriers, we cannot set $\nu_y = 0$, because in equilibrium it is J_y that is zero. We now need to take into account of the two types of carriers contributing to the total current, $J_y = q_1 n_1 \nu_{1y} + q_2 n_2 \nu_{2y}$. q_1 and q_2 are the elementary charge and are e or $-e$ depending on the carrier type. First, we consider the Lorentz force for carrier 1:

$$m_1 \frac{d\nu_{1x}}{dt} = q_1 E_x + q_1 \nu_{1y} B, \quad (\text{A.10})$$

$$m_1 \frac{d\nu_{1y}}{dt} = q_1 E_y - q_1 \nu_{1x} B. \quad (\text{A.11})$$

In the second term of Eq. A.10, the drift velocity, ν_{1y} , is on the order of the mobility times the electric field $\mu_1 E_y$ and in the one carrier regime we see $E_y = B\mu E_x$. Thus, $q_1 \nu_{1y} B$ is on the order of $q_1 B^2 \mu_1^2 E_x$. In the case where $B\mu$ is small, we drop this term.¹ Solution for Eq. A.10 then the same as Eq. A.5 in Section A.1

$$\bar{\nu}_{1x} = \mu_1 E_x \quad (\text{A.12})$$

¹ μ is on the order of $100 \text{ cm}^2/(\text{V}\cdot\text{s}) = 10^{-2} \text{ m}^2/(\text{V}\cdot\text{s})$ and B is on the order of 1 T , so $B\mu \approx 10^{-2}$.

To solve Eq. A.11, we consider an average velocity $\bar{\nu}_{1y}$ and the average scattering time τ_1 of the charge carriers. Replacing $d\nu_{1y}/dt$ with $\bar{\nu}_{1y}/\tau_1$ and solve for ν_{1y} :

$$\begin{aligned}\bar{\nu}_{1y} &= \frac{q_1\tau_1}{m_1}E_y - \frac{q_1\tau_1}{m_1}\bar{\nu}_{1x}B \\ &= \mu_1E_y - \mu_1^2BE_x.\end{aligned}\tag{A.13}$$

Similarly, for carrier 2, the solution for ν_{2y} is:

$$\bar{\nu}_{2y} = \mu_2E_y - \mu_2^2BE_x.\tag{A.14}$$

Now we can considering equilibrium condition, which is $J_y = 0$.

$$\begin{aligned}J_y &= q_1n_1\bar{\nu}_{1y} + q_2n_2\bar{\nu}_{2y} \\ &= q_1n_1\mu_1E_y - q_1n_1\mu_1^2BE_x + q_2n_2\mu_2E_y - q_2n_2\mu_2^2BE_x\end{aligned}\tag{A.15}$$

Solving for E_y/E_x , and assuming q_1 and q_2 are the same type of charge carriers (both electrons or both holes) so they have the same sign:²

$$\frac{E_y}{E_x} = \frac{n_1\mu_1^2 + n_2\mu_2^2}{n_1\mu_1 + n_2\mu_2}B.\tag{A.16}$$

We apply Eq. A.16 to the Hall coefficient:

$$R_H = \frac{E_y}{J_x B} = \frac{E_y}{\sigma E_x B} = \frac{1}{q} \frac{n_1\mu_1^2 + n_2\mu_2^2}{(n_1\mu_1 + n_2\mu_2)^2},\tag{A.17}$$

where the total conductivity σ of the sample is $q(n_1\mu_1 + n_2\mu_2)$. Rewriting Eq. A.17 by substituting $R_H = 1/(qn_H)$, $\sigma_1 = q_1n_1\mu_1$ and $\sigma_2 = q_2n_2\mu_2$, we have:

$$\frac{1}{n_H} = \left(\frac{\sigma_1}{\sigma_1 + \sigma_2}\right)^2 \frac{1}{n_1} + \left(\frac{\sigma_2}{\sigma_1 + \sigma_2}\right)^2 \frac{1}{n_2}.\tag{A.18}$$

²If the two types of carriers are of opposite sign, say $q_1 = +e$, $q_2 = -e$, then after taking account of both the sign in q and in μ , the numerator in Eq. A.16 is $n_1\mu_1^2 - n_2\mu_2^2$

This is the same as Eq. A.9 (Eq. 4.6). Lastly, Hall mobility is $\mu_H = R_H\sigma$, so $\mu_H = E_y/E_x/B$. From Eq. A.16 We have:

$$\begin{aligned}\mu_H &= \frac{n_1\mu_1^2 + n_2\mu_2^2}{n_1\mu_1 + n_2\mu_2} \\ &= \frac{\sigma_1}{\sigma_1 + \sigma_2}\mu_1 + \frac{\sigma_2}{\sigma_1 + \sigma_2}\mu_2.\end{aligned}\tag{A.19}$$

This is the expressions for the Hall mobility in Eq. 4.7.

Appendix B

Spectrophotometer corrections

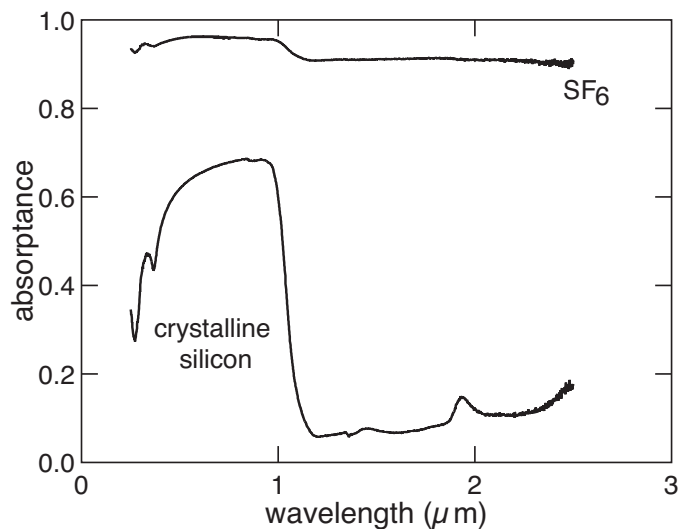


Figure B.1: Typical absorbance reported by the Mazur group [46].

Figure B.1 shows light absorption curves of a black silicon sample and a bare silicon wafer reported in Ref. [46]. Due to silicon's bandgap, silicon should be transparent to light at wavelengths greater than $1.1 \mu\text{m}$. Figure B.1, however, shows non-zero absorption from 1.1 to $2.5 \mu\text{m}$ for a crystalline silicon sample. The absorption curve has a rising tail and two humps. In this work we present how the spectrophotometer

acquires data and discuss methods to correct the measurement error.

B.1 Corrections to reflection measurements

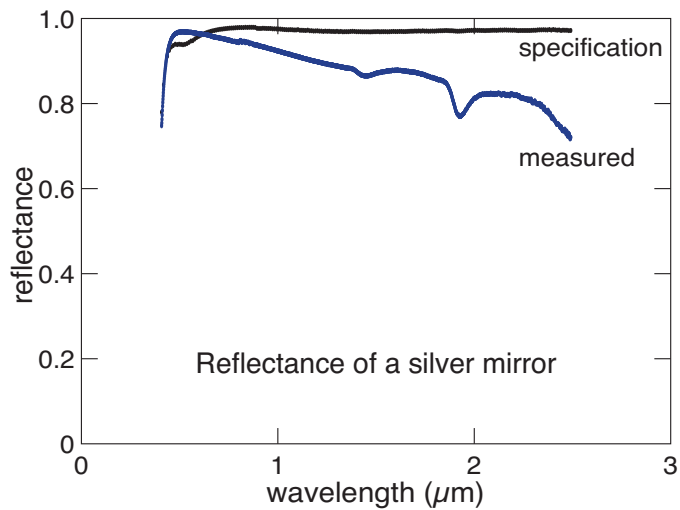


Figure B.2: Reflectance measurement of a silver mirror compared to the specification (Thorlabs Part # PF10-03-P01).

To obtain absorbance of a sample, we use the spectrophotometer to measure reflectance, R , and transmittance, T , and calculate absorbance using $A = 1 - R - T$. The measurement error comes from specular reflection. Figure B.2 shows the reflectance of a silver mirror we measured and a comparison to its specification. Similar to Figure B.1, the measured data also have two humps and a sloped curve. We realize that the integrating sphere in the spectrophotometer (Hitachi U-4001 or Hitachi U-4100) is not designed to measure specular reflection.

To understand the origin of the discrepancy between measurement and specification values, we present a simple model of the spectrophotometer. Figure B.3a is a schematic drawing of the spectrophotometer. The light output from the monochro-

mator passes through a lens and focuses onto a sample (not shown). For transmission measurements, the sample is placed at the front of the integrating sphere and the baseline disk closes the port at the back. For reflection measurements, we remove the baseline disk and place the sample at the back port of the integrating sphere. The photo detector is located at the top or the bottom of the integrating sphere. Before doing a measurement, we run a baseline with a ceramic disk placed at the back. The baseline signal is recorded as 100% reflection (or 100% transmission). Note that the baseline disk is made of Spectralon¹ and the integration sphere is made of BaSO₄, and both have diffuse surfaces.

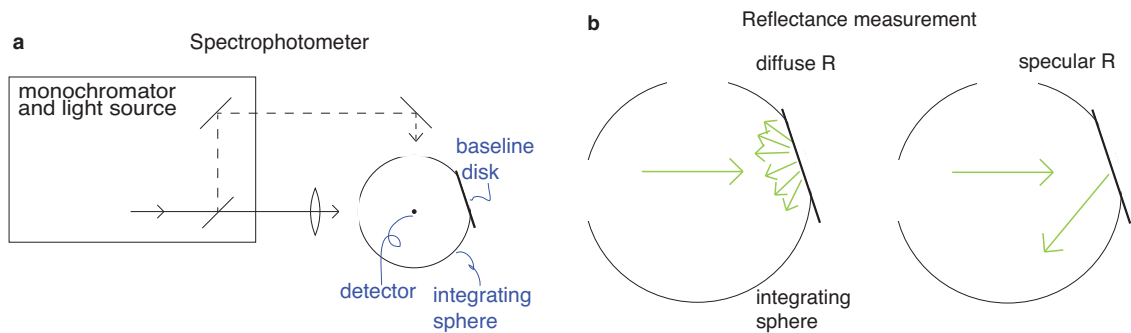


Figure B.3: (a) Schematic of the spectrophotometer setup (Hitachi U-4100 and U-4001). The solid line shows the sample beam path and the dashed line shows the reference beam path. The reference beam calibrates the intensity of the light output at different wavelengths and is not discussed in this work. (b) Illustration of the difference between a diffuse reflecting sample and of a specular reflecting sample.

We use a simple model to describe how the detector collects light. An illustration of the beam path in the integrating sphere is shown in Figure B.3b. Here we ignore the openings of the integrating sphere and the reference beam. We also do not take into account the possibility that some fraction of the light reflected from the integrating

¹1-inch, 99% individual calibrated single diffuse reflectance standards purchased from Labsphere. The baseline disk provided by the manufacturer is an Al₂O₃ disk.

sphere will hit the sample again. These will be higher order corrections. Let us define parameters:

$$C = (\text{area of the detector}) / (\text{area of the integrating sphere})$$

$$I_0 = \text{incoming light intensity}$$

$$R_I = \text{reflectance of the integrating sphere}$$

$$R_D = \text{reflectance of a diffuse reflecting sample}$$

$$R_S = \text{reflectance of a specular sample}$$

B.1.1 Case I: diffuse reflection

When the incoming light hits a diffuse surface, light is reflected in a solid angle of 2π (Figure B.3b). The fraction of reflected light reaching the detector is C , and the rest, $(1 - C)$, reaches the integrating sphere. Let S_i denote the signal the detector collects after the i -th time the light is reflected from a surface.

$$S_1 = I_0 \cdot R_D \cdot C \quad \text{Incoming light with intensity } I_0 \text{ reflects off the sample } (R_D) \text{ and the fraction } C \text{ reaches the detector.}$$

$$S_2 = I_0 \cdot R_D \cdot (1 - C) \cdot R_I \cdot C \quad \text{Intensity of light that did not get to the detector the first time: } I_0 R_D (1 - C). \text{ This amount reflects off the integrating sphere } R_I \text{ and a fraction } C \text{ reaches the detector.}$$

$$S_3 = I_0 \cdot R_D \cdot (1 - C)^2 \cdot R_I^2 \cdot C \quad \text{Similarly, after the third bounce, } S_3 \text{ is the signal the detector receives.}$$

$$\dots$$

$$S_n = I_0 \cdot R_D \cdot (1 - C)^{n-1} \cdot R_I^{n-1} \cdot C$$

The total signal the detector receives from a diffuse surface is:

$$S_{\text{diff,D}} = \sum_{n=1}^{\infty} I_0 \cdot R_D \cdot (1 - C)^{n-1} \cdot R_I^{n-1} \cdot C = \frac{I_0 \cdot C \cdot R_D}{1 - (1 - C) \cdot R_I}. \quad (\text{B.1})$$

B.1.2 Case II: specular reflection

When the incoming light hits a specular surface, the reflected light goes toward one point in the integrating sphere (Figure B.3b). Hence no lights reaches the detector after the first reflection. Then the light is diffusely reflected off the integrating sphere and a fraction C goes to the detector. Let S_i denote the signal the detector collects after the i -th time the light is reflected from a surface.

$$S_1 = I_0 \cdot R_S \cdot 0 = 0$$

The detector sees NOTHING when the light first reflects off a specular sample.

$$S_2 = I_0 \cdot R_S \cdot R_I \cdot C$$

Intensity of light that did not get to the detector the first time: $I_0 R_S$. This amount reflects off the integrating sphere R_I and a fraction C reaches the detector.

$$S_3 = I_0 \cdot R_S \cdot R_I \cdot (1 - C) \cdot R_I \cdot C$$

Intensity of light that did not get to the detector the second time $I_0 R_S R_I (1 - C)$ reflects off the integrating sphere R_I and a fraction C reaches the detector.

...

$$S_n = I_0 \cdot R_S \cdot R_I \cdot (1 - C)^{n-2} \cdot R_I^{n-2} \cdot C$$

For $n \geq 2$; Similarly, we have a geometric series.

The total signal the detector receives from a diffuse surface is:

$$S_{\text{spec,S}} = \sum_{n=2}^{\infty} I_0 \cdot R_S \cdot R_I \cdot (1 - C)^{n-2} \cdot R_I^{n-2} \cdot C = \frac{I_0 \cdot C \cdot R_S \cdot R_I}{1 - (1 - C) \cdot R_I}. \quad (\text{B.2})$$

The spectrophotometer defines reflectance of the baseline disk as 100% reflection. If the baseline disk has reflectance value of R_{disk} , what the measured reflectance is actually $R_{\text{measurement}} = \frac{S_{\text{sample}}}{S_{\text{diff,disk}}}$, where $S_{\text{diff,disk}} = \frac{I_0 \cdot C}{1 - (1 - C) \cdot R_I} \cdot R_{\text{disk}}$ from Eq. B.1.

For a diffuse sample, what we measure is:

$$R_{\text{mea,diff}} = \frac{S_{\text{diff,sample}}}{S_{\text{diff,disk}}} = \frac{\frac{I_0 \cdot C}{1 - (1 - C) \cdot R_I} \cdot R_{\text{diff,sample}}}{\frac{I_0 \cdot C}{1 - (1 - C) \cdot R_I} \cdot R_{\text{disk}}} = \frac{R_{\text{diff,sample}}}{R_{\text{disk}}}. \quad (\text{B.3})$$

For a specular sample what we measure is:

$$R_{\text{mea,spec}} = \frac{S_{\text{spec,sample}}}{S_{\text{diff,disk}}} = \frac{\frac{I_0 \cdot C}{1 - (1 - C) \cdot R_I} \cdot R_{\text{spec,sample}} \cdot R_I}{\frac{I_0 \cdot C}{1 - (1 - C) \cdot R_I} \cdot R_{\text{disk}}} = \frac{R_{\text{spec,sample}} \cdot R_I}{R_{\text{disk}}}. \quad (\text{B.4})$$

B.2 Results

In an ideal world, R_I and R_{disk} will both be equal to 1 (perfect reflectors) over the entire range of wavelengths. In reality, they are not, and Figure B.4 shows the reflectances of the integrating sphere and the baseline disk given by Hitachi.

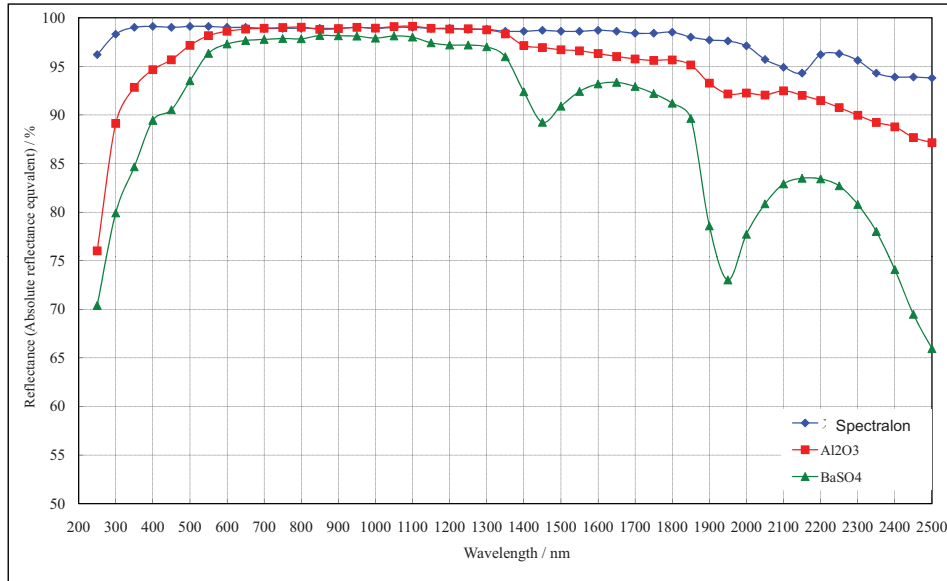


Figure B.4: Reflectance data provided by Hitachi. BaSO_4 (\blacktriangle) is the material used for the interior of the integrating sphere. The Spectralon (\blacklozenge) is the material used for baseline measurement. Al_2O_3 (\blacksquare) is the white baseline disk used for the old spectrophotometer (Hitachi U4001).

From Eq. B.4 and Figure B.4, it is clear that due to the spectral feature of R_I , the

integrating sphere (BaSO_4), our measurement for a bare silicon wafer has two humps. We also realize that we get extra factors not only for specular reflection measurements (R_I/R_{disk}), but also for diffuse reflection measurements ($1/R_{\text{disk}}$). There are many ways to correct the data; we find R_{disk} and R_{disk}/R_I by measuring a sample with a known reflectance (e.g. a silver mirror). We obtain the correction factor (CF) for for a specular surface by dividing the specification value of the silver mirror reflectance by measured reflectance. $\text{CF}_{\text{specular}} = R_{\text{disk}}/R_I = R_{\text{silver,specification}}/R_{\text{silver,measurement}}$. We correct all the specular silicon wafer samples by $R_{\text{siliconwafer}} = R_{\text{measurement}} \cdot \text{CF}_{\text{specular}}$. On the other hand, for the correction factor for diffuse reflectance, $\text{CF}_{\text{diffuse}} = R_{\text{disk}}$, we use the values provided by Hitachi. For diffusely reflecting samples such as black silicon, the corrected value is $R_{\text{blacksilicon}} = R_{\text{measurement}} \cdot \text{CF}_{\text{diffuse}}$.

Figure B.5 shows the measured data and the corrected data of Se-hyperdoped silicon samples and an untreated silicon wafer. The correction factor derived from a simple model works fairly well.

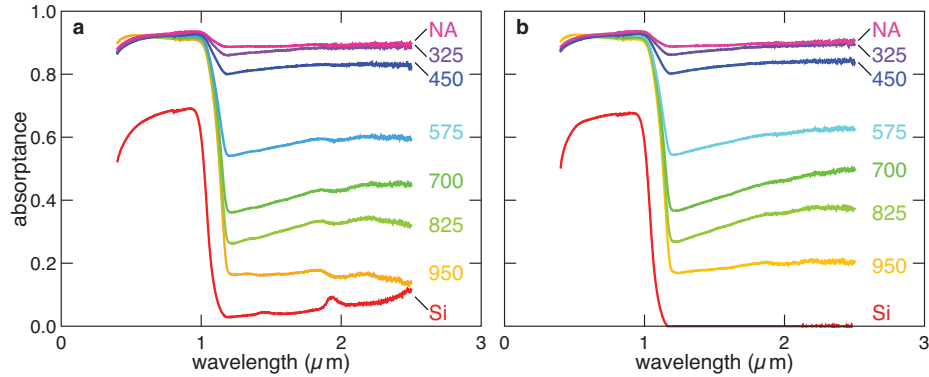


Figure B.5: Absorbance data of Si:Se and Si (a) before and (b) after correction. Data for the Si wafer are corrected using $\text{CF}_{\text{specular}}$ and for Si:Se samples are corrected using $\text{CF}_{\text{diffuse}}$. The number indicates the temperature the samples have been annealed at ($^{\circ}\text{C}$). NA = no anneal.

B.3 Summary and future work

In summary, we find that using the integrating sphere to measure a specular sample causes measurement errors and provide a method to correct the data. Yet several questions still remain. For example, what if the sample is semi-specular and semi-diffuse? In particular, we find the correction factor imperfect when the silicon wafer is only single side polished. Figure B.6 shows absorptance data of a single side polished (SSP) silicon wafer and a double side polished (DSP) silicon wafer before and after correction. For the SSP Si wafer, there is still non-zero absorptance for $\lambda > 1.1 \mu\text{m}$.

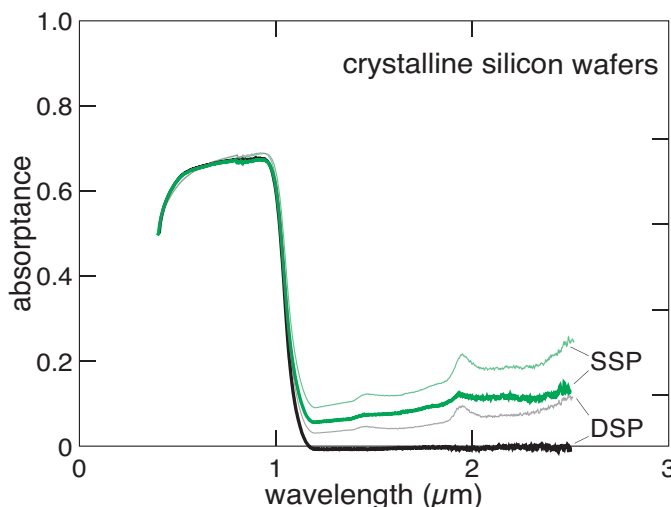


Figure B.6: Absorptance data of Si wafers before (thin lines) and after correction (thick lines). One wafer is double side polished (DSP) and the other wafer is single side polished (SSP).

We think two factors contribute to the remaining non-zero absorptance. First, since the silicon wafer is transparent to long wavelength light, both sides of the surface contribute to reflection. The front polished side reflects light specularly and the back side reflects light diffusely. Secondly, the transmission measurement also requires correction. For the transmission measurement, light passes through the polished side,

through silicon, and when it comes out from the rough side, it *transmits diffusely*. As a result, part of the transmitted light reaches the baseline disk and part of the light reaches the integrating sphere. Both reflection and transmission measurements create conditions different than how the baseline is performed, so the result could be different than expected.

We believe it is important to consider methods to correct the absorptance value of a single side polish wafer because in most of our work, the black silicon is textured. If the textured surface does not absorb light strongly, the reflection scenario is similar to a SSP silicon wafer. Comparing the light absorptance of a 950-K annealed black silicon wafer in Figure B.5b to the light absorptance for a single side polished wafer in Figure B.6, it is hard to know whether there is residual light absorption after annealing. One might be able to gain insight by comparing reflectance of a SSP wafer with the polished side facing the incident light to the reflectance of the same sample with the rough side facing the incident light. One can also consider using the same material for the baseline disk and the integrating sphere to minimize the difference in reflectance between the two materials.

In conclusion, we study how the spectrophotometer collects reflectance data and provide a method to correct reflectance obtained from a specular surface. All absorption data in this thesis (Figures 1.1, 2.10, 4.2, 5.1, 5.2, and 6.2) are corrected using the method presented in this appendix. Challenging remains when the sample is weakly absorbing and is only rough on one side (e.g. Figure 4.2b), and the measurement errors can be upto 20%.

Appendix C

The photovoltaic potential of fs-laser textured amorphous silicon

Femtosecond laser texturing of silicon yields micrometer scale surface roughness that reduces reflection and enhances light absorption. In this work, we study the potential of using this technique to improve efficiencies of amorphous silicon-based solar cells by laser texturing thin amorphous silicon films. We use a Ti:sapphire femtosecond laser system to texture amorphous silicon, and we also study the effect of laser texturing the substrate before depositing amorphous silicon. We report on the material properties including surface morphology, light absorption, crystallinity, as well as solar cell efficiencies before and after laser texturing.

C.1 Introduction

Hydrogenated amorphous silicon (a-Si) solar cells have several advantages over other photovoltaic materials because of strong light absorption and low processing temperature, allowing reduced material usage on low cost substrates [163]. The absorption coefficient of a-Si is higher than crystalline Si due to the lack of long-range order which reduces the momentum conservation requirement, but the disorder also causes a high concentration of defects, limiting the efficiency of charge carrier extraction. The trade-off between charge carrier extraction and optical absorption leads to devices with thin layers of a-Si combined with a light-trapping design. Moreover, defects form when a-Si is exposed to sunlight (the Staebler-Wronski effect) [164], and the stabilized, light-soaked efficiency reduces by at least 10% relative to a cell's initial performance [165, 166]. In this work, we explore treating a-Si with femtosecond laser (fs-laser) pulses to modify the crystallinity as well as the surface morphology for enhanced light absorption, and we study the effect of laser treatment on solar cell performance.

Common light trapping designs for a-Si solar cells utilize randomly textured substrates, plasmonic scattering structures [167–169], or textured transparent top contact [170, 171]. Femtosecond-laser irradiation of silicon results in semi-periodic surface textures that have periodicity on the order of the laser wavelength (800 nm in this study) [1]. Surface textures with sizes slightly smaller than the wavelength of light are ideal for diffracting incident light into shallow angles and enhance the optical path length [172]. Efficient light trapping surfaces that approach the Lambertian limit have been demonstrated by fs-laser processing; moreover, the size of the texture can

be tuned and applied to thin-film material regardless of the crystallinity [10, 79].

Compared to a-Si, nanocrystalline silicon (nc-Si) has larger carrier mobility and higher stability [173]. Solar cells fabricated with nc-Si have higher stabilized efficiency. Nanocrystalline silicon is normally fabricated under carefully controlled deposition condition [174, 175]. On the other hand, it has been demonstrated that treating a-Si with fs-laser pulses anneals and transforms a-Si into nc-Si [173, 176]. Therefore, it is promising to process a-Si solar cells with fs-laser pulses, transforming both the surface morphology and crystallinity for enhanced light absorption and material stability.

C.2 Experimental

We use an *n-i-p* structure for the solar cell design [177], and we increase the absorption with two different methods. (a) We perform laser texturing directly on 2- μm thick hydrogenated a-Si deposited via plasma enhanced chemical vapor deposition (PECVD). (b) We perform laser texturing on the substrate prior to a-Si deposition. The schematics of the two devices and a reference cell are illustrated in Figure C.1. To simplify the fabrication process, we use a degenerately doped silicon (p-type, 0.01 $\Omega\cdot\text{cm}$) not only as the substrate but also as the bottom conductive contact and the back reflector. We discuss later in Section C.4 on how the substrate adds to series resistance and hence reduces the photovoltaic efficiency.

For laser-textured a-Si, the substrate is first solvent cleaned and then dipped in 5% hydrofluoric acid for 60 s to remove surface oxide. The wafer is then transferred to the PECVD chamber, where 30 nm of p-type a-Si is deposited, followed by a 2- μm intrinsic a-Si deposition, both at 200°C. The intrinsic layer is thick since subsequent

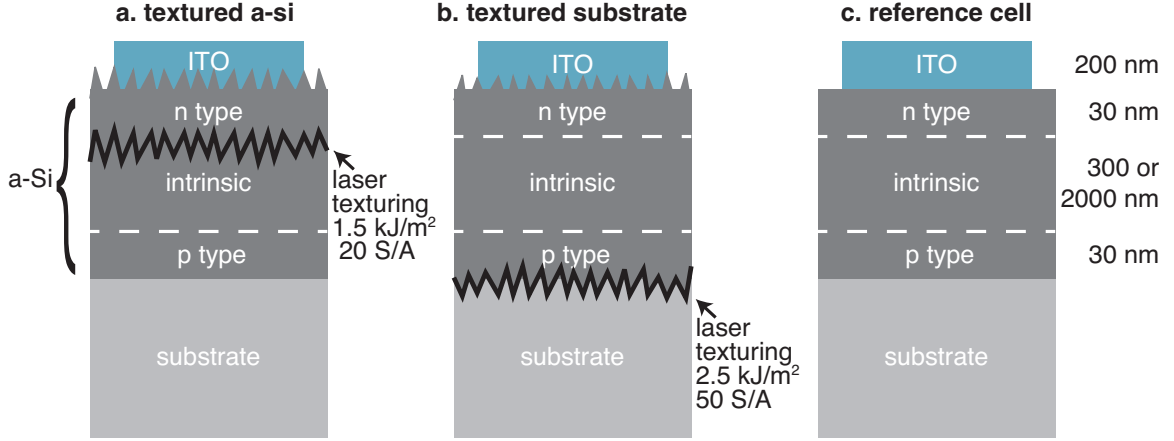


Figure C.1: sample schematics. (a) laser-textured a-Si. The n-type a-Si is deposited after laser treatment on a 2- μm intrinsic layer. (b) laser-textured substrate with a-Si *n-i-p* layers deposited after the laser treatment. (c) reference cell structure. The intrinsic layer is either 300 nm or 2 μm . In all cases, the p-type and n-type a-Si layers are both 30 nm, and the ITO transparent conductive contact is 200 nm.

laser texturing removes material through ablation. We then perform laser texturing on intrinsic layer before depositing the final n-type a-Si layer (30 nm at 200°C). The laser treatment is carried out in a hydrogen ambient environment (pressure = 500 Torr) using a Ti:sapphire amplified laser system (center wavelength 800 nm, pulse duration 80 fs). We use a set of scanning mirrors to process several $1 \times 1 \text{ cm}^2$ squares, and, on average, 20 laser pulses were delivered to every surface of the sample. The average number of laser pulses on a given spot is referred to as *shots per area* (S/A). We optimized the overlapping of the laser pulse and the fluence (energy density $F = 1.5 \text{ kJ/m}^2$) to produce an efficient light trapping surface without penetrating through the 2- μm intrinsic layer.

For the cell with the laser-textured substrate (Figure C.1b), we perform the laser treatment first on the substrate and then deposit a-Si *n-i-p* layers (30/300/30 nm). Compared to direct texturing on a-Si, since there is no restriction on the processing

thickness, we use a fluence of 2.5 kJ/m^2 and 50 shots per area.

We also fabricate reference cells for comparison. Due to the variability of sample performance from batch to batch, such as the exact thickness of the thin film deposited, we always fabricate reference cells on the same substrate as the textured cells and under identical conditions. Two types of reference cells are fabricated; both are *n-i-p* layers of a-Si, but with different intrinsic a-Si thickness: 300 and 2000 nm.

Finally, we sputter indium tin oxide (ITO, 200 nm, sheet resistance $30 \Omega/\square$) on all the samples to form a transparent conductive top contact. The active area (0.38 cm^2) is defined by the circular shadow mask for the ITO deposition. We measure the current-bias ($I-V$) curve of each device under dark and illuminated conditions (AM1.5 spectrum with a solar simulator). Samples are also characterized using scanning electron microscopy, Raman scattering spectroscopy, and absorption measurements using a UV-VIS-NIR spectrophotometer equipped with an integrating sphere.

C.3 Results

Representative images of the surface of the samples are shown in Figure C.2. Laser-textured a-Si samples have irregular surface features that are smaller than the textured substrate samples, which have semi-periodic surface textures. We choose the laser parameters for textured a-Si samples to ensure laser texturing does not penetrate the a-Si layer, which is only $2 \mu\text{m}$. The laser-material interaction is significantly different comparing laser processing of a-Si and of crystalline Si (the substrate). Under the same fabrication conditions (1.5 kJ/m^2 , 20 S/A), no surface texturing occurs on the substrate. We increased both the fluence (2.5 kJ/m^2) and the number of over-

lapping laser pulses (50 S/A). However, the fluence and shots per area cannot be too large, otherwise a-Si deposition is not uniform on the textured substrate.

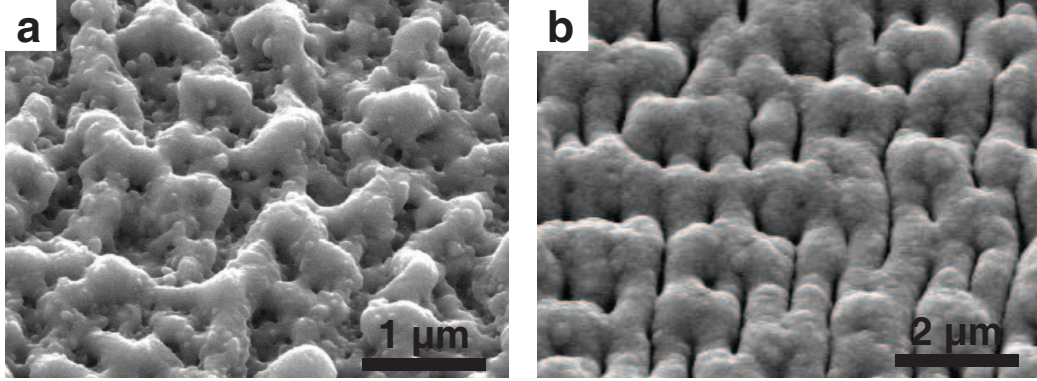


Figure C.2: 45° scanning electron micrographs of the samples before ITO deposition. (a) laser-textured a-Si and (b) laser-textured substrate with a-Si *n-i-p* layers deposited on top.

Figure C.3 shows the illuminated current-bias characteristics of each type of solar cell. Table C.1 summarizes the best solar cell fabricated in each set of experiments. A planar a-Si solar cell should have an intrinsic layer with thickness less than 300 nm to ensure efficient carrier extraction through the amorphous material [168,177]. The reference cell with a 300-nm intrinsic layer (Reference a1) has an efficiency of 1.89%, and the efficiencies of the laser-textured a-Si solar cells are an order of magnitude lower than the reference cells. Reference cell a2 is 2-μm thick, and the efficiency is 0.60%, smaller than Reference a1, due to the reduction in the short circuit current density (J_{SC}) from the inefficient carrier collection over the thick amorphous layer. Reference cell a2 has the same thickness as the a-Si before laser texturing (2 μm) and is 7.5 times more efficient than the textured solar cell, indicating laser processing was not effective. After laser texturing, the open circuit voltage (V_{OC}) drops from 0.82 V to 0.54 V. The drop in V_{OC} could either due to increasing shunting or due to

crystallized Si (the bandgap of crystalline Si is smaller than amorphous Si, resulting in a reduction of V_{OC}). On the other hand, if laser texturing is effective, J_{SC} should increase since more light is absorbed. J_{SC} of the textured a-Si solar cell, however, is much lower than both of the reference cells. This reduction in J_{SC} could be due to increased recombination at the surface or from laser-induced defects.

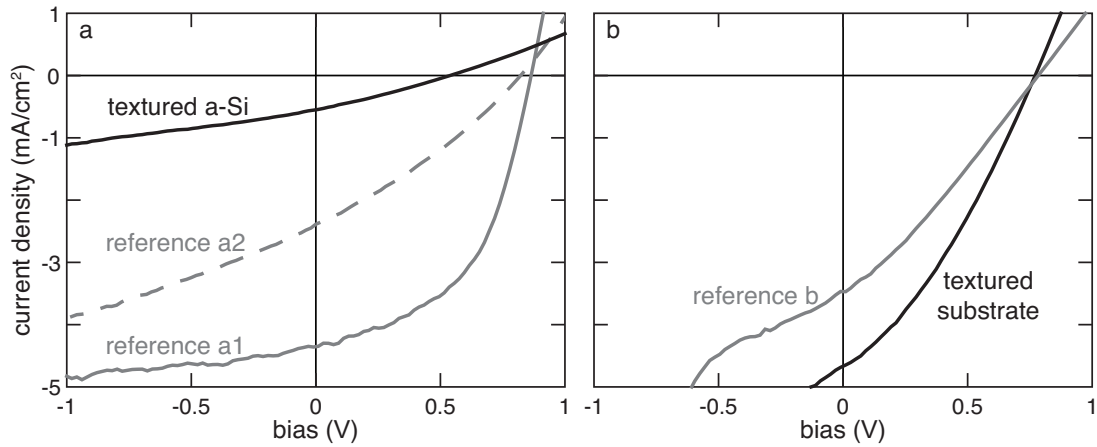


Figure C.3: illuminated $I-V$ curves of solar cells. (a) laser-textured a-Si solar cell (black) plotted together with two reference cells. The intrinsic a-Si thickness is 300 nm for Reference a1 (gray solid line) and is 2000 nm for Reference a2 (gray dash line). (b) solar cell on a laser-textured substrate (black) and reference b (gray) that was fabricated on the same substrate under the same condition

Figure C.3b compares the solar cells fabricated on top of the textured substrate and Reference b. To avoid the variability mentioned above, Reference b is fabricated on the same chip as the solar cells on the textured substrate. The V_{OC} is the same but the J_{SC} is improved by 35%. As a result the efficiency increases by 0.4% absolute. We note that Reference b is not as efficient as Reference a1, which ideally should be the same. Due to practical reasons, the exact same a-Si deposition parameter was not feasible when this set of cells was fabricated, so the deposition conditions were

Table C.1: illuminated I - V data

Sample	Efficiency (%)	J_{SC} (mA/cm ²)	V_{OC} (V)	Fill factor
Textured a-Si (a)	0.08	0.55	0.54	0.28
Reference a1 (300nm)	1.89	4.37	0.86	0.50
Reference a2 (2000nm)	0.60	2.39	0.82	0.31
Textured substrate (b)	1.18	4.68	0.78	0.32
Reference b (300nm)	0.78	3.46	0.78	0.29

slightly different between the two reference cells (a1 and b).

Figure C.4 shows that for the laser-textured a-Si sample, the absorption increases, and the laser processing also crystallizes silicon. To perform optical absorption measurements, we deposit a-Si on a transparent glass and laser-texture the sample with the parameters described in the experimental section. We measure the light transmittance (T) and reflectance (R) and calculate absorptance as $A = 100 - T - R$ (%). The fringes in the absorptance curves in the near infrared range are because of multiple reflections of light at both the front and back surface of the thin film, which interfere constructively or destructively depending on both the thickness of the a-Si film and the wavelength of the incident light.¹ After laser texturing, the above bandgap light absorption increases by 20% absolute and the absorption edge is shifted toward longer wavelength. Furthermore, before laser texturing, the Raman spectrum of the reference sample shows the signature a-Si Raman shift at 480 cm⁻¹ [173]. After laser texturing, a sharp Raman peak at 520 cm⁻¹ indicates that some amorphous silicon is transformed into crystalline silicon.

¹The transmission measurement is performed at normal incidence and reflection measurement is performed at a small angle offset (8°) in order to capture the reflected light. When calculating absorption from transmission and reflection data, the fringes should cancel out if the samples are perfectly aligned. These fringes are very sensitive to the measurement angle and in our setup T and R are performed at slightly different angle, so after computing the absorptance, the fringes do not cancel out perfectly.

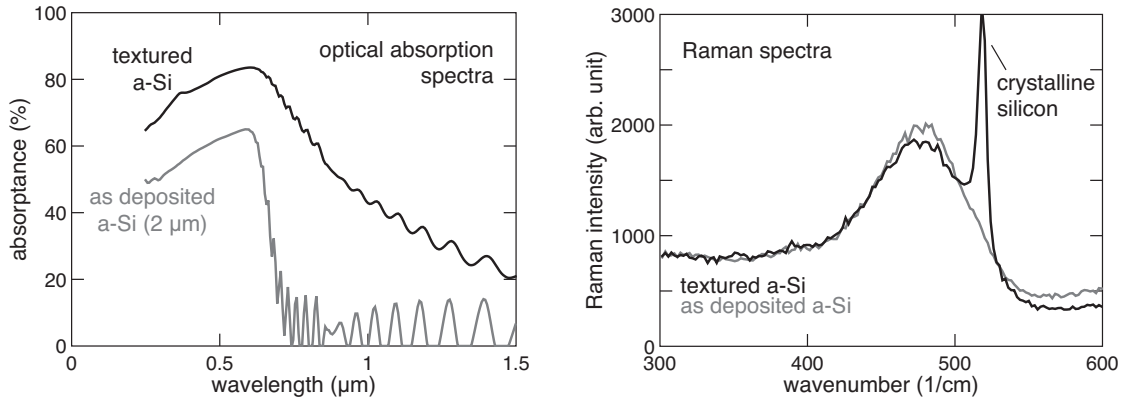


Figure C.4: Optical absorption spectra (left) and Raman spectra (right) of laser-textured a-Si and a reference sample.

It is not easy to quantify the amount of absorption enhancement for the samples on laser-textured substrate since the silicon substrate is not transparent and thus transmittance measurements cannot be performed. In the visible light range, the reflectance of the surface is less than 20%, compared to a reflectance of about 40% for planar a-Si. Since no laser treatment is performed on the deposited a-Si, we do not expect the material crystallinity to change.

C.4 Discussion

The solar cells fabricated from laser-textured a-Si are an order of magnitude less efficient than the reference cells, while a-Si solar cells on top of the laser-textured substrate increase the short circuit current and hence the efficiency. Within the parameters presented in this work, fs-laser texturing and crystallization of a-Si directly for photovoltaic applications does not work as well as enhancing the light absorption by using a fs-laser textured substrate. We discuss possible reasons for low efficiencies

after laser treating a-Si and suggest future directions for enhancing light absorption using laser treated substrates.

This experiment is a proof-of-principle study; therefore, many fabrication parameters are not optimized and the efficiencies of the cells in this study are lower than what is commonly achieved [163]. For example, we chose silicon as a substrate to ensure good a-Si adhesion for CVD deposition, but this substrate is more resistive and less reflective than common back contacts. Furthermore, the sputtered ITO is also more resistive than the desired transparent front contact [177]. This is likely due to the fact that the oxygen content and the substrate temperature are not optimized during ITO sputtering. Both the front and back contacts introduce resistive loss and lower the overall efficiency. Since the substrate and the ITO contact are the same across all of our samples, though, we can still compare the performance of different samples with their reference cells.

We now discuss possible reasons for the efficiency reduction after laser texturing the a-Si. First, we observe formation of pinholes after laser irradiation. We suspect that the hydrogen from the hydrogenated a-Si outgases quickly when the sample is heated by the laser, leaving behind pinholes. Starting with a-Si film that has lower hydrogen concentration could avoid formation of pinholes that degrade the material quality, but our experimental setup does not allow us to change the concentration of hydrogen in the a-Si film. We observe fewer pinholes when using laser fluences higher than 1.5 kJ/m^2 , so there could be better laser parameters that avoid pinhole formation. Secondly, as the surface textures develop, the local fluence of the laser pulses is no longer uniform across the rough surface, and it is possible that this causes

heating and diffusion in the p-type layer underneath. As a result, laser irradiation could affect the interface between the p-type and the intrinsic a-Si. Future work will focus on fine tuning the laser parameters to ensure that laser texturing removes enough excessive a-Si for texturing but does not over-texture and affect the p-type layer underneath.

Since currently we cannot achieve higher efficiencies by using fs-laser treatment to both enhance absorption and to crystallize silicon, we decouple the surface texturing and laser irradiation of a-Si by performing laser texturing on the substrate. In principle, if the thickness of the a-Si solar cell is reduced, the Staebler-Wronski effect will also be reduced [163,167]. We show increased efficiency when the laser irradiation is no longer directly on a-Si. Moreover, fs-laser texturing can be achieved on a wide variety of substrates [178–180], so this experiment shows that we can use the laser texturing technique to enhance light absorption for a-Si solar cells. The thickness of the a-Si solar cells can be further optimized for efficient carrier collection and reduced light-soaked efficiency reduction. Furthermore, investigating the use of fs-laser treatment to texture different substrates and optimizing the surface morphology for light trapping should also improve the efficiency.

We demonstrated that laser texturing the substrate is a feasible method for improving light absorption. The semi-periodic textured surface created by fs-laser processing is effective for anti-reflection and light trapping. In the future, it may also be possible to use these surface textures for template stripping to replicate these surface structures quickly and large scales [181,182].

C.5 Conclusion

In conclusion, we apply fs-laser processing techniques to texture and crystallize a-Si for photovoltaic applications. While the absorption and crystallinity of fs-laser processed a-Si improves, the overall cell efficiency does not increase, due to irradiation-induced damage such as pinhole formation. On the other hand, light absorption can be improved by fabricating a-Si solar cells on laser-textured substrates, which improves both the short circuit current and the efficiency. Future work on tuning the laser processing parameters for texturing a-Si with lower hydrogen content as well as laser texturing ZnO or glass (which are common back contacts and substrates for a-Si solar cells) could yield fruitful results.

Bibliography

- [1] B. R. Tull, J. E. Carey, E. Mazur, J. P. McDonald, and S. M. Yalisove, *MRS Bulletin* **31**, 626 (2006).
- [2] C. H. Crouch, J. E. Carey, M. Shen, E. Mazur, and F. Y. Genin, *Applied Physics A* **79**, 1635 (2004).
- [3] M. Winkler, Ph.D. thesis, Harvard University, 2009.
- [4] C. Wu, C. H. Crouch, L. Zhao, J. E. Carey, R. Younkin, J. A. Levinson, E. Mazur, R. M. Farrell, P. Gothoskar, and A. Karger, *Applied Physics Letters* **78**, 1850 (2001).
- [5] T. G. Kim, J. M. Warrender, and M. J. Aziz, *Applied Physics Letters* **88**, 3 (2006).
- [6] B. P. Bob, A. Kohno, S. Charnvanichborikarn, J. M. Warrender, I. Umezu, M. Tabbal, J. S. Williams, and M. J. Aziz, *Journal of Applied Physics* **107**, 123506 (2010).
- [7] M. A. Sheehy, B. R. Tull, C. M. Friend, and E. Mazur, *Materials Science and Engineering B-Solid State Materials for Advanced Technology* **137**, 289 (2007).
- [8] C. H. Crouch, J. E. Carey, J. M. Warrender, M. J. Aziz, E. Mazur, and F. Y. Genin, *Applied Physics Letters* **84**, 1850 (2004).
- [9] A. Halbwx, T. Sarnet, P. Delaporte, A. Sentis, H. Etienne, F. Torregrosa, V. Vervisch, I. Perichaud, and S. Martinuzzi, *Thin Solid Films* **516**, 6791 (2008).
- [10] V. V. Iyengar, B. K. Nayak, and M. fC. Gupta, *Solar Energy Materials and Solar Cells* **94**, 2251 (2010).
- [11] C. W. White, S. R. Wilson, B. R. Appleton, and F. W. Young, *Journal of Applied Physics* **51**, 738 (1980).
- [12] R. Reitano, P. M. Smith, and M. J. Aziz, *Journal of Applied Physics* **76**, 1518 (1994).

- [13] A. Luque and A. Marti, *Advanced Materials* **22**, 160 (2010).
- [14] Y. Liu, S. Liu, Y. Wang, G. Feng, J. Zhu, and L. Zhao, *Laser Physics* **18**, 1148 (2008).
- [15] V. Zorba, N. Boukos, I. Zergioti, and C. Fotakis, *Applied Optics* **47**, 1846 (2008).
- [16] M. A. Bassam, P. Parvin, B. Sajad, A. Moghimi, and H. Coster, *Applied Surface Science* **254**, 2621 (2008).
- [17] K. Affolter, W. Luthy, and M. Vonallmen, *Applied Physics Letters* **33**, 185 (1978).
- [18] J. M. Fairfiel and G. H. Schwuttk, *Solid-State Electronics* **11**, 1175 (1968).
- [19] P. G. Carey, T. W. Sigmon, R. L. Press, and T. S. Fahlen, *IEEE Electron Device Letters* **6**, 291 (1985).
- [20] P. G. Carey, K. Bezjian, T. W. Sigmon, P. Gildea, and T. J. Magee, *IEEE Electron Device Letters* **7**, 440 (1986).
- [21] M. Tabbal, T. Kim, D. N. Woolf, B. Shin, and M. J. Aziz, *Applied Physics A* **98**, 589 (2010).
- [22] E. Fogarassy, R. Stuck, J. J. Grob, and P. Siffert, *Journal of Applied Physics* **52**, 1076 (1981).
- [23] W. M. Wang, A. S. Lin, and J. D. Phillips, *Applied Physics Letters* **95**, 3 (2009).
- [24] K. M. Yu, W. Walukiewicz, J. Wu, W. Shan, J. W. Beeman, M. A. Scarpulla, O. D. Dubon, and P. Becla, *Physical Review Letters* **91**, 4 (2003).
- [25] K. M. Yu, W. Walukiewicz, J. Wu, W. Shan, M. A. Scarpulla, O. D. Dubon, J. W. Beeman, and P. Becla, *Physica Status Solidi B-Basic Research* **241**, 660 (2004).
- [26] K. M. Yu, W. Walukiewicz, J. W. Ager, D. Bour, R. Farshchi, O. D. Dubon, S. X. Li, I. D. Sharp, and E. E. Haller, *Applied Physics Letters* **88**, 3 (2006).
- [27] S. K. Sundaram and E. Mazur, *Nature Materials* **1**, 217 (2002).
- [28] L. A. Lompre, J. M. Liu, H. Kurz, and N. Bloembergen, *Applied Physics Letters* **43**, 168 (1983).
- [29] A. Cavalleri, K. Sokolowski-Tinten, J. Bialkowski, M. Schreiner, and D. von der Linde, *Journal of Applied Physics* **85**, 3301 (1999).

- [30] J. A. Kittl, P. G. Sanders, M. J. Aziz, D. P. Brunco, and M. O. Thompson, *Acta Materialia* **48**, 4797 (2000).
- [31] P. L. Liu, R. Yen, N. Bloembergen, and R. T. Hodgson, *Applied Physics Letters* **34**, 864 (1979).
- [32] R. Hull, *Properties of Crystalline Silicon* (The Institution of Electrical Engineers, London, 1999).
- [33] V. I. Emel'yanov and D. V. Babak, *Applied Physics A* **74**, 797 (2002).
- [34] M. J. Aziz and C. W. White, *Physical Review Letters* **57**, 2675 (1986).
- [35] D. E. Hoglund, M. O. Thompson, and M. J. Aziz, *Physical Review B* **58**, 189 (1998).
- [36] S. U. Campisano, D. C. Jacobson, J. M. Poate, A. G. Cullis, and N. G. Chew, *Applied Physics Letters* **45**, 1216 (1984).
- [37] M. O. Thompson, J. W. Mayer, A. G. Cullis, H. C. Webber, N. G. Chew, J. M. Poate, and D. C. Jacobson, *Physical Review Letters* **50**, 896 (1983).
- [38] M. T. Winkler, M.-J. Sher, Y.-T. Lin, M. J. Smith, H. Zhang, S. Gradecak, and E. Mazur, *Journal of Applied Physics* **111**, 093511 (2012).
- [39] R. O. Carlson, R. N. Hall, and E. M. Pell, *Journal of Physics and Chemistry of Solids* **8**, 81 (1959).
- [40] D. P. Korfiatis, K. A. T. Thoma, and J. C. Vardaxoglou, *Journal of Physics D-Applied Physics* **40**, 6803 (2007).
- [41] J. Bonse, S. Baudach, J. Kruger, W. Kautek, and M. Lenzner, *Applied Physics A* **74**, 19 (2002).
- [42] H. R. Vydyanath, J. S. Lorenzo, and F. A. Kroger, *Journal of Applied Physics* **49**, 5928 (1978).
- [43] E. Janzen, H. G. Grimmeiss, A. Lodding, and C. Deline, *Journal of Applied Physics* **53**, 7367 (1982).
- [44] B. R. Tull, M. T. Winkler, and E. Mazur, *Applied Physics A* **96**, 327 (2009).
- [45] M. A. Sheehy, L. Winston, J. E. Carey, C. A. Friend, and E. Mazur, *Chemistry of Materials* **17**, 3582 (2005).
- [46] R. Younkin, J. E. Carey, E. Mazur, J. A. Levinson, and C. M. Friend, *Journal of Applied Physics* **93**, 2626 (2003).

- [47] E. Janzen, R. Stedman, G. Grossmann, and H. G. Grimmeiss, *Physical Review B* **29**, 1907 (1984).
- [48] J. E. Carey, C. H. Crouch, M. Y. Shen, and E. Mazur, *Optics Letters* **30**, 1773 (2005).
- [49] G. A. Thomas, M. Capizzi, F. Derosa, R. N. Bhatt, and T. M. Rice, *Physical Review B* **23**, 5472 (1981).
- [50] R. A. Myers, R. Farrell, A. M. Karger, J. E. Carey, and E. Mazur, *Applied Optics* **45**, 8825 (2006).
- [51] Z. H. Huang, J. E. Carey, M. G. Liu, X. Y. Guo, E. Mazur, and J. C. Campbell, *Applied Physics Letters* **89**, 033506 (2006).
- [52] D. K. Schroder, R. N. Thomas, and J. C. Swartz, *IEEE Transactions on Electron Devices* **25**, 254 (1978).
- [53] A. R. Zanatta and I. Chambouleyron, *Physical Review B* **53**, 3833 (1996).
- [54] M. Wolf, *Proceedings of the Institute of Radio Engineers* **48**, 1246 (1960).
- [55] M. J. Keevers and M. A. Green, *Journal of Applied Physics* **75**, 4022 (1994).
- [56] P. T. Landsberg, *Recombination in Semiconductors* (Cambridge University Press, UK, 2003).
- [57] A. Luque, A. Marti, E. Antolin, and C. Tablero, *Physica B-Condensed Matter* **382**, 320 (2006).
- [58] A. Luque and A. Marti, *Physical Review Letters* **78**, 5014 (1997).
- [59] W. Shockley and H. J. Queisser, *Journal of Applied Physics* **32**, 510 (1961).
- [60] A. Luque, A. Marti, and C. Stanley, *Nature Photonics* **6**, 146 (2012).
- [61] M. T. Winkler, D. Recht, M.-J. Sher, A. J. Said, E. Mazur, and M. J. Aziz, *Physical Review Letters* **106**, 178701 (2011).
- [62] E. Antolin, A. Marti, J. Olea, D. Pastor, G. Gonzalez-Diaz, I. Martil, and A. Luque, *Applied Physics Letters* **94**, 042115 (2009).
- [63] J. J. Krich, B. I. Halperin, and A. Aspuru-Guzik, *Journal of Applied Physics* **112**, 013707 (2012).
- [64] E. Ertekin, M. T. Winkler, D. Recht, A. J. Said, M. J. Aziz, T. Buonassisi, and J. C. Grossman, *Physical Review Letters* **108**, 026401 (2012).

- [65] B. K. Newman, J. T. Sullivan, M. T. Winkler, M.-J. Sher, M. A. Marcus, S. Fakra, M. J. Smith, S. Gradecak, E. Mazur, and T. Buonassisi, in *24th European Photovoltaic Solar Energy Conference (EU PVSEC, Hamburg, Germany, 2009)*, pp. 236 – 238.
- [66] Y. Mo, M. Z. Bazant, and E. Kaxiras, *Physical Review B* **70**, 10 (2004).
- [67] J. E. Sipe, J. F. Young, J. S. Preston, and H. M. Vandriel, *Physical Review B* **27**, 1141 (1983).
- [68] J. F. Young, J. S. Preston, H. M. Vandriel, and J. E. Sipe, *Physical Review B* **27**, 1155 (1983).
- [69] J. F. Young, J. E. Sipe, and H. M. Vandriel, *Physical Review B* **30**, 2001 (1984).
- [70] T. Sarnet, J. E. Carey, and E. Mazur, *AIP Conference Proceedings* **1464**, 219 (2012).
- [71] P. Lorazo, L. J. Lewis, and M. Meunier, *Physical Review B* **73**, 22 (2006).
- [72] E. D. Diebold, N. H. Mack, S. K. Doom, and E. Mazur, *Langmuir* **25**, 1790 (2009).
- [73] R. Younkin, Ph.D. thesis, Harvard University, 2001.
- [74] T. H. Her, R. J. Finlay, C. Wu, S. Deliwala, and E. Mazur, *Applied Physics Letters* **73**, 1673 (1998).
- [75] T. H. Her, R. J. Finlay, C. Wu, and E. Mazur, *Applied Physics A* **70**, 383 (2000).
- [76] M. Y. Shen, C. H. Crouch, J. E. Carey, and E. Mazur, *Applied Physics Letters* **85**, 5694 (2004).
- [77] B. R. Tull, Ph.D. thesis, Harvard University, 2007.
- [78] H. M. Branz, V. E. Yost, S. Ward, K. M. Jones, B. To, and P. Stradins, *Applied Physics Letters* **94**, 3 (2009).
- [79] B. G. Lee, Y.-T. Lin, M.-J. Sher, E. Mazur, and H. M. Branz, in *38th IEEE Photovoltaic Specialists Conference (PVSC) (IEEE, Austin, TX, 2012)*, pp. 001606–001608.
- [80] B. K. Nayak, V. V. Iyengar, and M. C. Gupta, *Progress in Photovoltaics: Research and Applications* **19**, 631 (2011).
- [81] J. E. Carey, Ph.D. thesis, Harvard University, 2004.

- [82] M. J. Smith, M.-J. Sher, B. Franta, Y.-T. Lin, E. Mazur, and S. Gradecak, *Journal of Applied Physics* **112**, 083518 (2012).
- [83] M. J. Smith, Ph.D. thesis, Massachusetts Institute of Technology, 2012.
- [84] T. Gimpel, I. Hoger, F. Falk, W. Schade, and S. Kontermann, *Applied Physics Letters* **101**, 111911 (2012).
- [85] E. Bustarret, C. Marcenat, P. Achatz, J. Kacmarcik, F. Levy, A. Huxley, L. Ortega, E. Bourgeois, X. Blase, D. Debarre, and J. Boulmer, *Nature* **444**, 465 (2006).
- [86] S. X. Hu, P. D. Han, S. Wang, X. Mao, X. Y. Li, and L. P. Gao, *Semiconductor Science and Technology* **27**, 102002 (2012).
- [87] E. Landi, P. G. Carey, and T. W. Sigmon, *IEEE Transactions on Computer-Aided Design of Integrated Circuits and Systems* **7**, 205 (1988).
- [88] D. Bauerle, *Laser Processing and Chemistry*, 4th ed. (Springer, Heidelberg, 2011), p. 566.
- [89] D. Cammilleri, F. Fossard, D. Debarre, C. T. Manh, C. Dubois, E. Bustarret, C. Marcenat, P. Achatz, D. Bouchier, and J. Boulmer, *Thin Solid Films* **517**, 75 (2008).
- [90] D. Recht, J. T. Sullivan, R. Reedy, T. Buonassisi, and M. J. Aziz, *Applied Physics Letters* **100**, 112112 (2012).
- [91] J. Bonse and J. Kruger, *Journal of Applied Physics* **108**, 034903 (2010).
- [92] J. Bonse, K. W. Brzezinka, and A. J. Meixner, *Applied Surface Science* **221**, 215 (2004).
- [93] K. Wittmaack, *Vacuum* **34**, 119 (1984).
- [94] A. Slaoui, F. Foulon, R. Stuck, and P. Siffert, *Applied Physics A* **50**, 479 (1990).
- [95] A. Slaoui, F. Foulon, and P. Siffert, *Journal of Applied Physics* **67**, 6197 (1990).
- [96] G. G. Bentini, M. Bianconi, L. Correra, R. Nipoti, D. A. Patti, and A. Gasparotto, *Applied Surface Science* **36**, 394 (1989).
- [97] T. J. Chuang, *Journal of Chemical Physics* **74**, 1453 (1981).
- [98] J. Royer, P. Y. Tessier, B. Grolleau, and G. Turban, *Journal of Vacuum Science & Technology A: Vacuum, Surfaces, and Films* **14**, 234 (1996).

- [99] J. H. Sanderson, R. V. Thomas, W. A. Bryan, W. R. Newell, P. F. Taday, and A. J. Langley, *Journal of Physics B: Atomic, Molecular and Optical Physics* **30**, 4499 (1997).
- [100] D. De Salvador, G. Bisognin, E. Napolitani, M. Mastromatteo, N. Baggio, A. Carnera, F. Boscherini, G. Impellizzeri, S. Mirabella, S. Boninelli, F. Priolo, and F. Cristiano, *Applied Physics Letters* **95**, 101908 (2009).
- [101] F. Panciera, K. Hoummada, M. Mastromatteo, D. De Salvador, E. Napolitani, S. Boninelli, G. Impellizzeri, F. Priolo, A. Carnera, and D. Mangelinck, *Applied Physics Letters* **101**, 103113 (2012).
- [102] G. A. Somorjai, *Introduction to Surface Chemistry and Catalysis* (Wiley, New York, 1993), p. 12.
- [103] M. J. Smith, M.-J. Sher, B. Franta, Y.-T. Lin, E. Mazur, and S. Gradecak, *Applied Physics A* in press (2013).
- [104] N. Mangan, Y.-T. Lin, E. Mazur, and M.P. Brenner, publication in preparation.
- [105] S. H. Pan, D. Recht, S. Charnvanichborikarn, J. S. Williams, and M. J. Aziz, *Applied Physics Letters* **98**, 121913 (2011).
- [106] B. I. Shklovskii and A. L. Efros, *Electronic properties of doped semiconductors*, *Springer Series in Solid-State Sciences* (Springer-Verlag, Berlin, 1984), pp. 25–36, 76–82.
- [107] C. S. Hung and J. R. Gliessman, *Physical Review* **96**, 1226 (1954).
- [108] H. Fritzsche, *Physical Review* **99**, 406 (1955).
- [109] C. Yamanouchi, K. Mizuguchi, and W. Sasaki, *Journal of the Physical Society of Japan* **22**, 859 (1967).
- [110] J. Basinski and R. Olivier, *Canadian Journal of Physics* **45**, 119 (1967).
- [111] N. F. Mott, *Reviews of Modern Physics* **40**, 677 (1968).
- [112] E. M. Conwell, *Physical Review* **103**, 51 (1956).
- [113] N. F. Mott and W. D. Twose, *Advances in Physics* **10**, 107 (1961).
- [114] O. V. Emelyanenko, T. S. Lagunova, D. N. Nasledov, and G. N. Talalakin, *Soviet Physics-Solid State* **7**, 1063 (1965).
- [115] H. G. Grimmeiss and E. Janzen, in *Handbook on semiconductors*, completely ed., edited by T. S. Moss (North-Holland, Amsterdam ;New York, 1994), Vol. 3, Chap. 23, p. 1758.

- [116] T. F. Lee, R. D. Pashley, T. C. McGill, and J. W. Mayer, *Journal of Applied Physics* **46**, 381 (1975).
- [117] V. V. Abramov, N. B. Brandt, V. A. Kulbachinskii, A. B. Timofeev, A. G. Ulyashin, N. V. Shlopak, and I. G. Gorolchuk, *Soviet Physics Semiconductors-USSR* **25**, 310 (1991).
- [118] V. A. Kulbachinskii, V. G. Kytin, V. V. Abramov, A. B. Timofeev, A. G. Ulyashin, and N. V. Shlopak, *Soviet Physics Semiconductors-USSR* **26**, 1009 (1992).
- [119] J. Olea, G. Gonzalez-Diaz, D. Pastor, I. Martil, A. Marti, E. Antolin, and A. Luque, *Journal of Applied Physics* **109**, 063718 (2011).
- [120] W. Kern, *Handbook of semiconductor wafer cleaning technology: science, technology and applications* (Noyes Publications, New Jersey, 1993).
- [121] L. J. van der Pauw, *Philips Technical Review* **20**, 220 (1958).
- [122] W. Robert Thurber, NIST Hall Effect Measurements, <http://www.nist.gov/pml/div683/hall.cfm>.
- [123] J. Blakemore, *Semiconductor Statistics* (Pergamon Press, New York, 1962), pp. 121–130, 153–159.
- [124] R. A. Smith, *Semiconductors* (Cambridge University Press, Cambridge, UK, 1978).
- [125] S. M. Sze, *Physics of Semiconductor Devices* (Wiley-Interscience, New York, 1981), pp. 21, 34.
- [126] H. Neumann, *Crystal Research and Technology* **23**, 1377 (1988).
- [127] L. Essaleh, S. M. Wasim, and J. Galibert, *Journal of Applied Physics* **90**, 3993 (2001).
- [128] K. Sanchez, I. Aguilera, P. Palacios, and P. Wahnou, *Physical Review B* **82**, 165201 (2010).
- [129] B. K. Newman, E. Ertekin, J. T. Sullivan, M. T. Winkler, M. A. Marcus, S. C. Fakra, M.-J. Sher, E. Mazur, J. C. Grossman, and T. Buonassis, Submitted for publication to *Physical Review B* (2013).
- [130] M.-J. Sher, M. T. Winkler, and E. Mazur, *MRS Bulletin* **36**, 439 (2011).
- [131] N. Sclar, *Journal of Applied Physics* **52**, 5207 (1981).

- [132] Y. A. Astrov, L. M. Portsel, A. N. Lodygin, V. B. Shuman, and N. V. Abrosimov, *Infrared Physics and Technology* **52**, 25 (2009).
- [133] H. G. Grimmeiss, E. Janzen, H. Ennen, O. Schirmer, J. Schneider, R. Worner, C. Holm, E. Sirtl, and P. Wagner, *Physical Review B* **24**, 4571 (1981).
- [134] N. S. Zhdanovich and Y. I. Kozlov, *Soviet Physics Semiconductors-USSR* **10**, 1102 (1976).
- [135] J. C. Swartz, D. H. Lemmon, and R. N. Thomas, *Solid State Communications* **36**, 331 (1980).
- [136] G. Grossmann, K. Bergman, and M. Kleverman, *Physica B & C* **146**, 30 (1987).
- [137] I. Umezu, A. Kohno, J. M. Warrender, Y. Takatori, Y. Hirao, S. Nakagawa, A. Sugimura, S. Charnvanichborikarn, J. S. Williams, and M. J. Aziz, *AIP Conference Proceedings* **1399**, 51 (2011).
- [138] M. J. Smith, M. T. Winkler, M.-J. Sher, Y.-T. Lin, E. Mazur, and S. Gradecak, *Applied Physics A* **105**, 795 (2011).
- [139] A. Poruba, A. Fejfar, Z. Remes, J. Springer, M. Vanecek, J. Kocka, J. Meier, P. Torres, and A. Shah, *Journal of Applied Physics* **88**, 148 (2000).
- [140] W. B. Jackson, N. M. Johnson, and D. K. Biegelsen, *Applied Physics Letters* **43**, 195 (1983).
- [141] Y. F. Huang, S. Chattopadhyay, Y. J. Jen, C. Y. Peng, T. A. Liu, Y. K. Hsu, C. L. Pan, H. C. Lo, C. H. Hsu, Y. H. Chang, C. S. Lee, K. H. Chen, and L. C. Chen, *Nature Nanotechnology* **2**, 770 (2007).
- [142] P. B. Clapham and M. C. Hutley, *Nature* **244**, 281 (1973).
- [143] P. R. L. Sarma, T. R. R. Mohan, S. Venkatachalam, V. P. Sundarsingh, and J. Singh, *Journal of Materials Science* **27**, 4762 (1992).
- [144] J. I. Pankove, *Optical processes in semiconductors* (Dover, New York, 1975).
- [145] J. Susskind and J. E. Searl, *Journal of Quantitative Spectroscopy & Radiative Transfer* **18**, 581 (1977).
- [146] S. Aldallal, M. Hammam, S. M. Alalawi, S. Aljishi, and A. Breitschwerdt, *Philosophical Magazine B-Physics of Condensed Matter Statistical Mechanics Electronic Optical and Magnetic Properties* **63**, 839 (1991).
- [147] B. Begemann, J. Dorschner, T. Henning, and H. Mutschke, *Astrophysical Journal* **464**, L195 (1996).

- [148] S. Aldallal, S. Aliishi, M. Hammam, S. M. Alalawi, M. Stutzmann, S. Jin, T. Muschik, and R. Schwarz, *Journal of Applied Physics* **70**, 4926 (1991).
- [149] K. E. Petersen, U. Birkholz, and D. Adler, *Physical Review B* **8**, 1453 (1973).
- [150] J. E. Griffiths, M. Malyj, G. P. Espinosa, and J. P. Remeika, *Physical Review B* **30**, 6978 (1984).
- [151] L. Andrews, P. Hassanzadeh, D. V. Lanzisera, and G. D. Brabson, *Journal of Physical Chemistry* **100**, 16667 (1996).
- [152] A. Gaymann, H. P. Geserich, and H. vonLohneysen, *Physical Review B* **52**, 16486 (1995).
- [153] E. Yablonovitch, *Journal of the Optical Society of America* **72**, 899 (1982).
- [154] J. T. Sullivan, Ph.D. thesis, Massachusetts Institute of Technology, 2013.
- [155] I. Umezu, J. M. Warrender, S. Charnvanichborikarn, A. Kohno, J. S. Williams, M. Tabbal, D. G. Papazoglou, X. C. Zhang, and M. J. Aziz, *Journal of Applied Physics* in press (2013).
- [156] J. M. Bao, M. Tabbal, T. Kim, S. Charnvanichborikarn, J. S. Williams, M. J. Aziz, and F. Capasso, *Optics Express* **15**, 6727 (2007).
- [157] A. Serpenguezel, A. Kurt, I. Inanc, J. E. Cary, and E. Mazur, *Journal of Nanophotonics* **2**, 9 (2008).
- [158] W. B. Henley and D. A. Ramappa, *Journal of Applied Physics* **82**, 589 (1997).
- [159] A. A. Taskin and E. G. Tishkovskii, *Semiconductors* **36**, 605 (2002).
- [160] K. Sugioka, M. Meunier, and A. Pique, *Laser Precision Microfabrication* (Springer-Verlag Berlin Heidelberg, Berlin, Heidelberg, 2010).
- [161] N. Lopez, L. A. Reichertz, K. M. Yu, K. Campman, and W. Walukiewicz, *Physical Review Letters* **106**, 028701 (2011).
- [162] T. Tanaka, K. M. Yu, A. X. Levander, O. D. Dubon, L. A. Reichertz, N. Lopez, M. Nishio, and W. Walukiewicz, *Japanese Journal of Applied Physics* **50**, 082304 (2011).
- [163] B. Rech and H. Wagner, *Applied Physics A* **69**, 155 (1999).
- [164] H. Fritzsche, *Annual Review of Materials Research* **31**, 47 (2001).
- [165] J. Meier, J. Spitznagel, U. Kroll, C. Bucher, S. Fay, T. Moriarty, and A. Shah, *Thin Solid Films* **451**, 518 (2004).

- [166] T. Matsui, H. Sai, K. Saito, and M. Kondo, *Japanese Journal of Applied Physics* **51**, 10NB04 (2012).
- [167] V. E. Ferry, M. A. Verschuuren, H. B. T. Li, E. Verhagen, R. J. Walters, R. E. I. Schropp, H. A. Atwater, and A. Polman, *Optics Express* **18**, A237 (2010).
- [168] D. Derkacs, S. H. Lim, P. Matheu, W. Mar, and E. T. Yu, *Applied Physics Letters* **89**, 093103 (2006).
- [169] C. I. Ho, D. J. Yeh, V. C. Su, C. H. Yang, P. C. Yang, M. Y. Pu, C. H. Kuan, I. C. Cheng, and S. C. Lee, *Journal of Applied Physics* **112**, 023113 (2012).
- [170] C. M. Hsu, C. Battaglia, C. Pahud, Z. C. Ruan, F. J. Haug, S. H. Fan, C. Ballif, and Y. Cui, *Advanced Energy Materials* **2**, 628 (2012).
- [171] C. Eisele, C. E. Nebel, and M. Stutzmann, *Journal of Applied Physics* **89**, 7722 (2001).
- [172] S. E. Han and G. Chen, *Nano Letters* **10**, 4692 (2010).
- [173] A. V. Emelyanov, A. G. Kazanskii, P. K. Kashkarov, O. I. Konkov, E. I. Terukov, P. A. Forsh, M. V. Khenkin, A. V. Kukin, M. Beresna, and P. Kazansky, *Semiconductors* **46**, 749 (2012).
- [174] Y. Mai, S. Klein, R. Carius, J. Wolff, A. Lambertz, F. Finger, and X. Geng, *Journal of Applied Physics* **97**, 114913 (2005).
- [175] J. M. Pearce, N. Podraza, R. W. Collins, M. M. Al-Jassim, K. M. Jones, J. Deng, and C. R. Wronski, *Journal of Applied Physics* **101**, 114301 (2007).
- [176] J.-M. Shieh, Z.-H. Chen, B.-T. Dai, Y.-C. Wang, A. Zaitsev, and C.-L. Pan, *Applied Physics Letters* **85**, 1232 (2004).
- [177] T. M. Razykov, C. S. Ferekides, D. Morel, E. Stefanakos, H. S. Ullal, and H. M. Upadhyaya, *Solar Energy* **85**, 1580 (2011).
- [178] M. Y. Shen, *Modern Physics Letters B* **24**, 257 (2010).
- [179] D. Dufft, A. Rosenfeld, S. K. Das, R. Grunwald, and J. Bonse, *Journal of Applied Physics* **105**, 034908 (2009).
- [180] S. K. Das, D. Dufft, A. Rosenfeld, J. Bonse, M. Bock, and R. Grunwald, *Journal of Applied Physics* **105**, 084912 (2009).
- [181] W. Zhou and T. W. Odom, *Nature Nanotechnology* **6**, 423 (2011).
- [182] P. Nagpal, N. C. Lindquist, S.-H. Oh, and D. J. Norris, *Science* **325**, 594 (2009).